UNIVERSITY OF CALIFORNIA SAN DIEGO

Numerical Investigation of Squid-Inspired Pulsed-Jet Propulsion

A dissertation submitted in partial satisfaction of the
requirements for the degree
Doctor of Philosophy

in

Structural Engineering

by

Xiaobo Bi

Committee in charge:

Professor Qiang Zhu, Chair
Professor Jiun-Shyan Chen
Professor Veronica Eliasson
Professor Geno Pawlak
Professor Michael T. Tolley

2021

The dissertation of Xiaobo Bi is approved, and it is acceptable in quality and form for publication on microfilm and electronically.

University of California San Diego

2021

DEDICATION

To my youth.

TABLE OF CONTENTS

LIST OF FIGURES

LIST OF TABLES

ACKNOWLEDGEMENTS

First of all, I would like to express my special thanks of gratitude to my advisor, Professor Qiang Zhu, for his selfless support and guidance during my Ph.D. life.

I deeply thank him for leading me into this profession and help me discover the beauty of rigorous scientific research. Without his support, I might have left academia years back. Besides guiding me to write papers, Prof. Zhu cultivated my scientific ethics and set a high standard for my future academic career. I learned from him that the fundamental goal of research is understanding underlying physics under superficial phenomena rather than just accumulating papers.

I would like to thank Prof. Jiun-Shyan Chen, Prof. Michael T. Tolley, Prof. Geno Pawlak, and Prof. Veronica Eliasson for serving on my defense committee. I have learned a lot from their lectures, papers and feedback during my PhD progress. I benefit a lot from the outstanding academic environment of UCSD.

Last but not the least, I would like to convey my gratitude to my family for their countless love and support of my career choice. This dissertation is dedicated to them. I will never forget where I get started.

Chapter 2, in part, is a reprint of the material as it appears in the following papers.

- Xiaobo Bi and Qiang Zhu, "Fluid-structure Interaction of a Squid-inspired Swimmer", *Physics of Fluids*, vol. 31, pp. 101901, 2019.

- Xiaobo Bi and Qiang Zhu, "Dynamics of a Squid-Inspired Swimmer in Free Swimming", *Bioinspiration & Biomimetics*, vol. 15, no. 1, pp. 016005, December 2019.

Chapter 3, in part, is a reprint of the material as it appears in the following papers.

- Xiaobo Bi and Qiang Zhu, "Pulsed-Jet Propulsion via Shape Deformation of an Axisymmetric Swimmer", *Physics of Fluids*, 32: 081902,2020.

- Xiaobo Bi, Qiang Zhu, "Efficiency of Pulsed-Jet Propulsion via Thrust-Drag Decoupling",*Physics of Fluids*, 33: 071902,2021.

- Xiaobo Bi, Qiang Zhu, "Effect of Nozzle Geometry on the Performance of Pulsed-Jet Propulsion", under review.

Chapter 4, in part, is a reprint of the material as it appears in the following paper.

- Xiaobo Bi and Qiang Zhu, "Numerical Investigation of Cephalopod-Inspired Locomotion with Intermittent Bursts", *Bioinspiration & Biomimetics*, vol. 13, pp. 056005,2018.

The dissertation author is the primary investigator and author of these papers.

VITA

2014	Bachelor of Engineering, Huazhong University of Science and Technology, China
2016	Master of Engineering, Huazhong University of Science and Technology, China
2021	Doctor of Philosophy, University of California San Diego

PUBLICATIONS

Xiaobo Bi and Qiang Zhu, "Fluid-structure Interaction of a Squid-Inspired Swimmer", *Physics of Fluids*, vol. 31, pp. 101901, 2019.(featured article)

Xiaobo Bi and Qiang Zhu, "Numerical Investigation of Cephalopod-Inspired Locomotion with Intermittent Bursts", *Bioinspiration & Biomimetics*, vol. 13, pp. 056005,2018. (featured article)

Xiaobo Bi and Qiang Zhu, "Pulsed-Jet Propulsion via Shape Deformation of an Axisymmetric Swimmer", *Physics of Fluids*, 32: 081902,2020.

Xiaobo Bi, Qiang Zhu, "Efficiency of Pulsed-Jet Propulsion via Thrust-Drag Decoupling",*Physics of Fluids*, 33: 071902,2021. (editor's pick)

Xiaobo Bi and Qiang Zhu, "Dynamics of a Squid-Inspired Swimmer in Free Swimming", *Bioinspiration & Biomimetics*, vol. 15, no. 1, pp. 016005, December 2019.

Qiang Zhu and Xiaobo Bi, "Effects of Stiffness Distribution and Spanwise Deformation on the Dynamics of a Ray-Supported Caudal Fin", *Bioinspiration & Biomimetics*, vol. 12, pp. 026011, 2017.

Caleb Christianson, Yi Cui, Xiaobo Bi, Qiang Zhu, Geno Pawlak, and Michael T. Tolley, "Cephalopod-Inspired Robot Capable of Cyclic Jet Propulsion Through Shape Change", *Bioinspiration & Biomimetics*, 16:016014,2021.

Qiang Zhu and Xiaobo Bi, "Dynamics and Internal Stress in Erythrocytes within Oscillatory Shear Flows: Effects of Cell Abnormality", under review.

Xiaobo Bi, Qiang Zhu, "Effect of Nozzle Geometry on the Performance of Pulsed-Jet Propulsion", under review.

TEACHING EXPERIENCE

TA, *Fluid Mechanics*(SE115), Winter 2018,2019,2020 (undergraduate course)

TA, *Mechanics III: Vibrations*(SE101C), Fall 2017,2018,2019,2020 (undergraduate course)

TA, *Cable Structure*(SE215), Spring 2019,2020,2021 (graduate course)

TA, *Solid Mechanics*(SE110B), Spring 2021 (undergraduate course)

PEER REVIEWS

Bioinspiration & Biomimetics, 2 manuscripts

Journal of Fluids and Structures, 4 manuscripts

PRESENTATIONS

Talk, 11th Southern California Flow Physics Symposium, UC San Diego, April 22,2017

Talk, 73rd Annual Meeting of the APS Division of Fluid Dynamics, Chicago, November 22–24, 2020

ABSTRACT OF THE DISSERTATION

Numerical Investigation of Squid-Inspired Pulsed-Jet Propulsion

by

Xiaobo Bi

Doctor of Philosophy in Structural Engineering

University of California San Diego, 2021

Professor Qiang Zhu, Chair

Inspired by the locomotion method of cephalopods such as squids, we propose a novel concept of underwater propeller that utilizes pulsed jet for thrust generation. A squid-inspired robot is expected to possess multiple advantages such as mechanical simplicity, high swimming speed, and low environmental footprint. To understand the physical mechanisms of squid-like jet propulsion, computational simulations are conducted to explore the underlying fluid dynamics and fluid-structure interaction problems.

A two-dimensional fluid-structure numerical model is firstly developed by using the Immersed Boundary Method (IBM), which avoids the complexity of body-fitted grid regeneration,

and is thus suitable for problems involving large body deformations. Through systematic simulations we demonstrate that the 2D squid-inspired swimmer is capable of long-distance swimming through cyclic deflation-inflation shape change. Through parametric studies, it is found that the body oscillation frequency is the most important parameter determining the hydrodynamics of the swimmer.

The 2D IBM-based model is then extended to an axi-symmetric numerical rendition. Based on control volume analysis, a thrust-drag decoupling strategy and a thrust decomposition method are proposed. In the thrust decomposition method the jet-related thrust is calculated as the summation of three components, the jet flux force, the exit normal stress and the flow momentum force inside the chamber. This method allows us to understand the underlying physics of force generation, e.g. the effects of jet speed profile, jet acceleration, background flow and nozzle geometry. Moreover, it enables the separation of thrust and drag forces on the body (a classical problem in free-swimming bodies) so that it leads to a novel method to calculate the propulsive efficiency.

Finally, a potential-flow-based rendition of a 3D squid-inspired propulsion system is developed to explore the swimming process and the dynamic characteristics. The results show that in the bursting phase its peak speed depends on the size of the body, the deformation time, the amount of volume change during the deformation, and the size of the nozzle. The optimal speed is found to coincide with the critical formation number, indicating that the formation of vortex rings in the wake plays a pivotal role in the dynamics of the system.

Chapter 1

Introduction

1.1 Background

1.1.1 Fish-inspired locomotion

With remarkable efficiency, controllability, and maneuverability, the locomotion capacity of aquatic animals has inspired the development of numerous biomimetic underwater vehicles and robots. The existing experiments, simulations, and prototypes are concentrated on the imitation of fish swimming [5–9]. All underwater propulsion methods rely on the process of momentum transfer from the body to the surrounding flow field. In fish and aquatic mammals this is achieved through undulatory motions of the body and flapping motions of the appendages (fins or flippers). These oscillatory motions lead to the formation of a reverse Kármán vortex street in the wake, where two staggered arrays of counter-rotating vortices induce a jet stream between them, providing the impulse for thrust generation.

Fish swimming is highly sophisticated. In steady swimming alone there are about 20 locomotion modes with different combinations of body undulation and unsteady flapping of fins, providing plentiful prototypes for artificial swimmers [5]. For example, the fins of bony fish

contain a soft collagenous membrane supported by embedded rays. Each ray consists of tendons actuated by a group of muscles so that it can be controlled individually, allowing the fin to perform complicated motions (*e.g.* the cupping motion, 'W'-shape motion and 'S'-shape motion) [6–8], each associated with a particular swimming mode (cruising, bursting, braking, *etc.*).

To date, most of the man-made underwater robots are based on imitation of fin-activated fish swimming. These robots therefore can be categorized into rigid robots since their bodies remain undeformable during the locomotion, while the artificial fins perform complex flapping motion to create driving force. The robots using rigid materials are perfect for repetitive operations due to their rapid and precise dynamic response. Nevertheless, there are two major drawbacks for the traditional rigid-bodied underwater robots. On the one hand, the rigid-bodied fish-like robots are not able to operate in confined and unstructured spaces. Soft-bodied bio-inspired robots becomes a solution to these issues. However soft structures have a delay in propagation of motion that limits the rate of actuation.

On the other hand, fish-like (fin-activated) robots can not achieve the multi-degree-of-freedom controllability using flapping foils (the mechanical replica of fish fins), which are usually rigid or with uniform stiffness. As a consequence, today's artificial swimmers perform far below the standard of their natural counterparts in terms of speed, efficiency, *etc*. In fact, with the state-of-the-art technology it poses tremendous challenge to artificial control and actuation systems to create motions similar to fish fins for better locomotion capacity [10–12].

1.1.2 Squid-inspired locomotion

Compared with the fish swimming, cephalopods (*i.e.* squids, octopuses and cuttlefish) locomotion have been mostly neglected. These animals are also capable of highly effective swimming, especially when escaping from predators. Indeed, cephalopods have developed a much simpler, yet equally effective method of escaping locomotion based on jet propulsion [13]. For

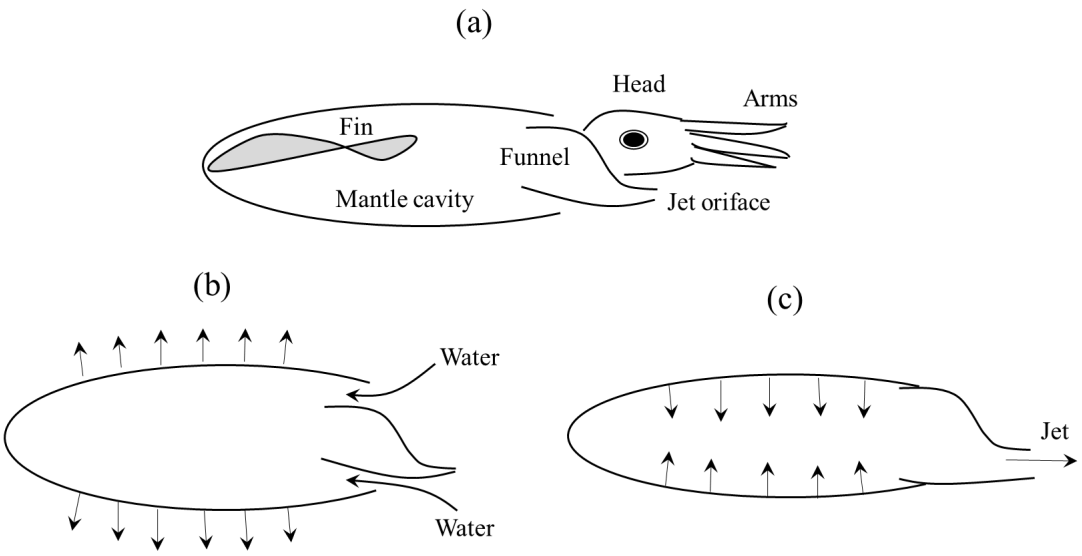

Figure 1.1: (a) A sketch of the structure in a squid. (b) A inflation phase, during which the mantle expands to refill the cavity. (c) A deflation phase, during which the mantle shrinks, pushing water out of the body to form a jet. This figure was modified from Fig. 1 in [1].

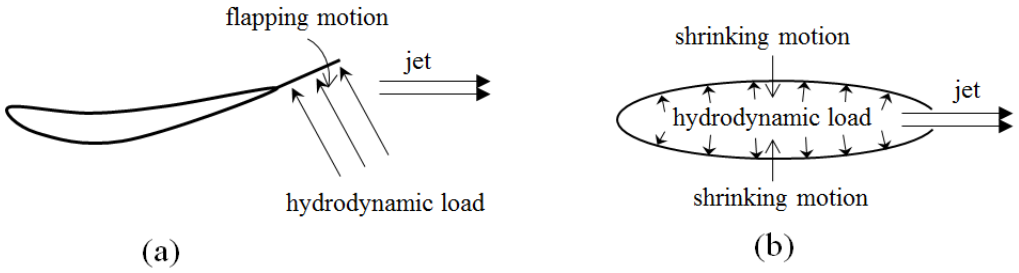

Figure 1.2: (a) In fin activated swimming the hydrodynamic load is concentrated on the fin. (b) In cephalopod-like swimming the the hydrodynamic load is distributed over the whole body. This mechanism allows soft-body creatures to achieve high speed swimming.

example, in such a swimming mode a squid (as shown in Fig. 1.1) first inflates its compression chamber (the mantle cavity) by sucking water through a wide inlet called mantle aperture. During that process (refer to inflation phase) its lateral dimension is increased by 30%. It then contracts its mantle and expels the water through a narrow funnel that can be pointed at a range of directions (refer to deflation phase). This propulsion method, usually referred to as the jetting mode, is often used in escape maneuvers.

Although squids are equipped with fins which are able to generate thrust and maneuvering forces through undulating and flapping motions, due to the lack of embedded supports (skeletal bones, rays, or fluid-filled cavities that enable hydrostatic support) these fins cannot sustain large hydrodynamic load so that they are only able to function in relatively low speeds. In the jetting mode, however, the hydrodynamic load is distributed over the whole body, rather than concentrating on a small portion of it (*e.g.* caudal fins) (see Fig. 1.2). Moreover, the hydrodynamic load is supported by the tension inside the body, rather than the bending stiffness of the body (as in fin-activated swimming). This strategy thus enables these soft-bodied creatures to reach extremely high bursting speeds of 10-25 body lengths per second [14, 15].

On the other hand, in this swimming method since the body deformation has to be reciprocal the jet formation is intermittent. Subsequently, the forward speed is unsteady with acceleration during the deflation phase and deceleration during the inflation phase. The unsteadiness of the forward speed may actually be beneficial in terms of locomotion efficiency. Recent studies about the hydrodynamics of the burst swimming of cephalopods illustrate that in addition to the repulsive force created by the jet, this locomotion mode also depends on shape and volume variations of the body [16–18]. Specifically, when the lateral dimension of a cephalopod-like swimmer decreases, its added mass in the swimming direction will decrease with time, leading to an added-mass-related force of $-\frac{d}{dt}\left(m_a V\right) = -\dot{m}_a V - m_a \dot{V}$ (V is the instantaneous speed of the swimmer), in which the term $F_a = -\dot{m}_a V$ provides additional thrust to the system since $\dot{m}_a < 0$. This results from the

recovery of the added-mass kinematic energy by the body, as demonstrated by the simulations in previous studies [17,19]. This effect, together with the shrinking mass of the body itself when water is expelled, contributes to the impressive bursting speed that can be achieved in this locomotion mode.

1.1.3 State of the art

There exist only a handful of investigations in the unique locomotion technique of cephalopods. The investigation started with observations and measurements of live animals in field or laboratory environments [14, 15, 20]. In laboratory experiments, the kinematics of the body (especially the fins) and the near-body flow fields in both the flapping and the jetting modes have been recorded [21–23]. These studies indicate that squids employ both jet propulsion and fin activation in locomotion. DPIV measurements also recorded various vorticity patterns in both fin activated and jet propelled motions [21, 22]. Similar jet propulsion mechanisms have also been discovered in other aquatic creatures [24].

Based on experimental observations of live animals, mechanical and robotic systems have been designed and manufactured to imitate the jet-propelled mechanism of squids and other cephalopods. A mechanical device containing a pressure chamber similar to the one in a squid was developed and tested by Weymouth *et al.* [25]. Despite its simplicity, this design is capable of reaching instantaneous speed comparable with its natural counterparts. Without a mechanism to refill the pressure chamber, this prototype system is only able to perform one bursting-coasting cycle. A more sophisticated design resolves this issue by using a motor-tendon system [26]. More recently, a soft-bodied robot capable of pulsed-jet swimming through cyclic shape deformations (inflation-deflation) has been developed by Christianson *et al.* [27].

The locomotion mechanism via jet formation and body deformation has also been studied numerically. Existing models fall into two categories, low-fidelity models [26] and high-fidelity

models [16–19]. The low-fidelity models are based on idealized fluid dynamics theory, in which the details of the flow field and vortex dynamics are not considered. The high-fidelity models, on the other hand, do not consider the flow inside the pressure chamber so that the jet flow is either neglected or artificially prescribed.

1.2 Motivations

Compared with fish-like propulsion that has been studied in most existing work, the novel squid-inspired jet propulsion will possess the following advantages:

1. Mechanical simplicity: Unlike the multi-degree-of-freedom controlling mechanism (*e.g.* the control and actuation of individual fin rays) required for high-efficiency fishlike swimming, a cephalopod-like swimmer relies on the inflation/deflation of its own body for locomotion. This can be achieved by a low-degree-of-freedom control/actuation system. It is particularly suitable for smart materials such as shape memory alloys so that no servo motors will be needed. With minimum number of moving parts, this system will be highly robust and reliable.

2. High speed and maneuverability: As demonstrated in observations of live animals [14, 15] and experimentally measured from a simple mechanical replica [25], squid-like swimmers may reach instantaneous speeds unreachable by today's fish-like robots (and this is achieved by a much simpler mechanical design). Moreover, if we use controllable nozzles similar to the funnel tube of a squid, the swimming direction can be easily controlled through thrust vectoring. By directly changing the direction of the thrust, this is expected to be a highly effective measure for maneuvering.

3. Versatility: With the soft body, it enables the operations in unstructured space.

4. Low noise: With few moving parts and no servo motors, the noise generation of a squid-like robot is expected to be much lower than a traditional one with propeller.

5. Compatibility with sample testing: The inflation-deflation locomotion pattern of a squid-like robot may be particularly useful when intermittent motion and sample testing is necessary. For example, in each inflation-deflation cycle the water sample it sucks in may be tested by instruments inside its body.

It is thus interesting and necessary to study in detail the dynamics of the squid-like jet propulsion. The aims of this thesis are using numerical modeling and theoretical analysis to understand the underlying physical mechanism of this propulsion mode and investigate the effect of physical parameters (*e.g.* frequency and amplitude of the body motion) on its hydrodynamic performance. This work will be a pioneering investigation in a novel locomotion mode that can be used in underwater vehicles. It will also greatly improve our knowledge about the biomechanics and locomotion performance of soft-bodied aquatic animals.

1.3 Dissertation outline

The rest of this thesis is organized as follows,

1. In Chapter 2, a fully coupled fluid-structure study of a two dimensional squid-inspired swimmer is described. An activation and control system of cyclic inflation-deflation body deformation, which can be directly applied in engineering, is also proposed.

2. In Chapter 3, an axis-symmetric squid-inspired swimmer is numerically analyzed in low Reynolds number regime using immersed-boundary method.

3. In Chapter 4, we extend our investigation to high Reynolds number regime to explore the dynamics of a three dimensional potential-flow-based numerical model.

4. In Chapter 5, conclusions and future directions will be presented.

Chapter 2

Fully Coupled Fluid-Structure Investigation of a Squid-Inspired Swimmer

In this Chapter, we create a two-dimensional fully-viscous fluid-structure interaction model of a squid-inspired propulsion system. Unlike the existing work in squid swimming, our purpose is not to investigate the biomechanics of actual squids. Instead, we aim to explore the possibility of a bio-inspired mechanical system that inherits some key design characteristics of squids, *e.g.* a pressure chamber that can be inflated and deflated through body deformation, and a orifice(or nozzle) through which jetting is allowed. Through numerical simulations we investigate the interactions among the structure, the activation system, and fluids inside and outside of the body. We are particularly interested in examining effects of body-shed vortices as well as robustness of the activation strategy.

Stemming from the immersed-boundary framework [28–30], this model takes full account of the effect of fluid viscosity (therefore the vorticity shedding from the body as well as the exit), the structural response of the body, and the underlying fluid-structure interaction mechanisms. This model is then applied to investigate the hydrodynamic performance of the system over

repeated deflation-inflation cycles, including the force generation, travelling speed and energetics. Nevertheless, in the current study we will be concentrated in relatively low Reynolds numbers so that turbulence effects, which may be important in the high-speed swimming mode of real squids, are not considered.

2.1 Model geometry

As shown in Fig. 2.1, we consider a two-dimensional rendition of the squid-inspired propulsion system consisting of a pressure chamber enclosed within an outer shell idealized as an inextensible beam with zero thickness. A swimming cycle is decomposed into two phases, deflation and inflation. During the deflation phase the eccentricity of the body shape (hereby represented as part of an ellipse with an open end; a detailed description of this geometry is included in Appendix A) changes from e_0 to e_1 ($e_1 > e_0$) so that the fluid inside the pressure chamber is expelled, creating a jet flow behind. In the inflation phase fluid is sucked back into the chamber and the eccentricity of the body shape decreases back to e_0. The equilibrium state of the beam coincides with the shape e_1. Current design is characterized by a single opening through which the fluid enters (during the inflation phase) and exits the chamber (during the deflation phase), *i.e.* this opening works as both the inlet and the exit (albeit a departure from the real squid).

2.2 Actuation system

The activation system of a squid consists of two groups of muscles (radial and circular) and a mantel wall [20]. The contraction of the radial muscles causes hyper-inflation of the mantel cavity, which is needed at the beginning of an escape maneuver. The deflation for jetting is activated by the contraction of the circular muscles. For continuous swimming, the refilling is enabled mostly by the elastic recoiling of the mantel wall. Inspired by this design, we have tested various measures

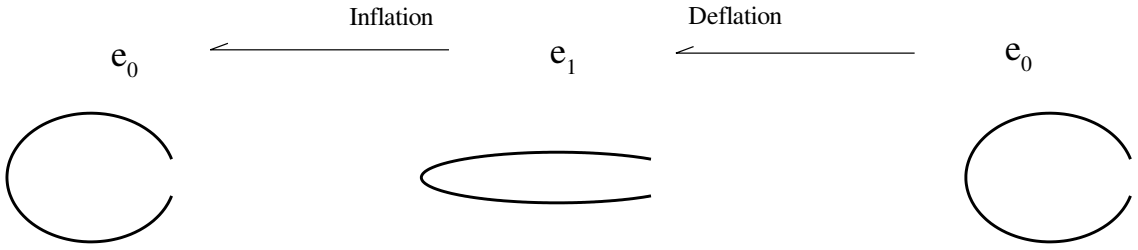

Figure 2.1: A complete deflation-inflation cycle during squid-inspired swimming.

to power the periodic deflation and inflation deformations of our model system, including, *e.g.* a system containing both longitudinal springs (similar to the radial muscles) and lateral springs (similar to the circular muscles), as well as a system in which the refilling/inflation process is powered using the bending energy stored in the beam (functioning as the mantel wall). Among all these options, a system containing springs with variable unstretched lengths outperform others in terms of controllability (the ability to achieve targeted body deformation) and repeatability (the ability to achieve periodic body deformations in long term simulations). In this particular design, the bending stiffness of the beam is chosen to be small. Its primary function is to prevent buckling of the body.

As shown in Fig. 2.2a, in our depiction the contraction/expansion of the body is driven by a model actuation system consisting of a sequence of linear springs, K_1 to K_8, from which lateral contraction/expansion forces are generated. Each of these springs has two unstretched lengths, $L_i^{(d)}$ and $L_i^{(i)}$ ($i = 1, \cdots, 8$), corresponding to the deflated and the inflated states of the body, respectively. These unstretched lengths are chosen to fit in the aforementioned reference body shapes e_0 and e_1. For example, during the deflation phase these springs are in natural states at the deflated reference shape with eccentricity e_1. On the other hand, during the inflation phase they are in their natural state at the inflated reference shape with eccentricity e_0. Uniformly distributed

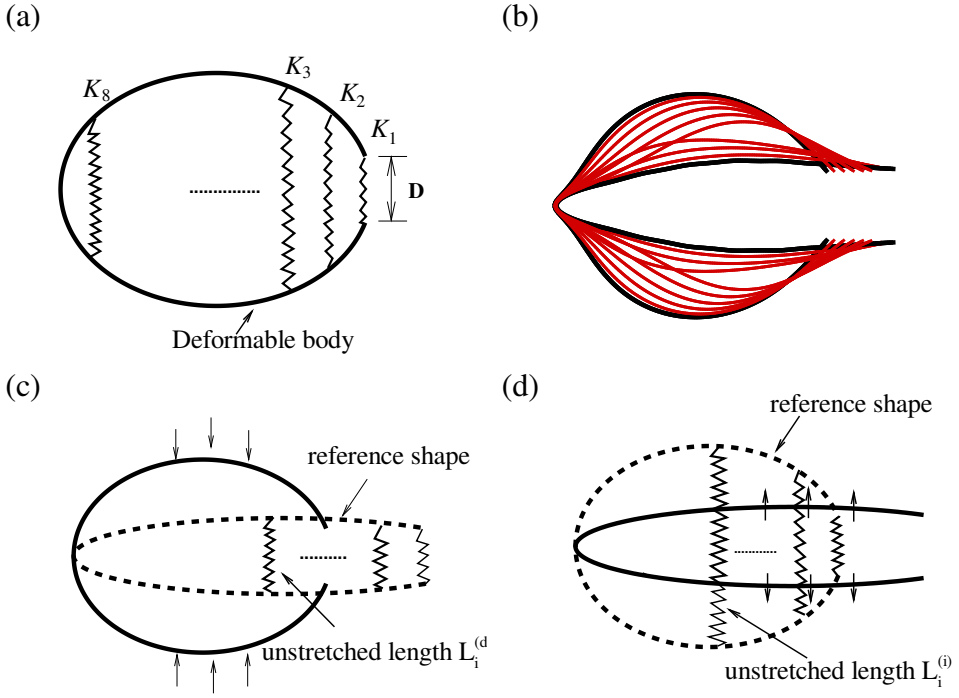

Figure 2.2: (a) Schematic depiction of the model, (b) deformation of the body (the fully deflated/inflated configurations are shown in black solid lines). Unstretched lengths for deflation phase (c) and inflation phase (d), the arrow indicates the direction of spring force.

in the longitudinal direction, these springs do not interact directly with the surrounding fluid. For simplicity, the stiffnesses of the springs are chosen to be identical, *i.e.* $K_i = K$, $i = 2, \cdots, 8$ except for the one at the exit, K_1, which is equal to $10K$ so that the change in the size of the exit (D) is negligibly small. This activation system, albeit developed mostly for modeling purpose, may be engineered either through mechanical design (*e.g.* a system that switches between two sets of springs) or by using materials with special properties (*e.g.* bi-state shape memory alloys).

A typical inflation-deflation cycle is activated in the following manner. Starting from the deflated state, the unstretched lengths of the springs are set as $L_i^{(i)}$ so that they expand to inflate the pressure chamber. After the total remaining strain energy in the springs is less than 2% of its maximum value ($E_m = \sum_{i=2}^{8} \frac{1}{2} K (L_i^{(i)} - L_i^{(d)})^2$), the unstretched lengths of the springs are switched to $L_i^{(d)}$, causing them to contract and triggering the deflation phase. Similar to the inflation phase, the deflation phase ends after the remaining strain energy in the springs is below 2% of E_m, when the unstretched lengths of the springs are switched back to $L_i^{(i)}$.

It is necessary to point out that the reference shapes (*i.e.* the ellipses with eccentricities e_0 and e_1) are only used as a convenient way to determine the unstretched lengths of the springs. It is not necessary for the actual deflated and inflated body shapes to match these reference ones perfectly. Due to the small but finite bending stiffness of the beam and the fluid dynamic forcing on the body, there does exist certain difference between the actual body shapes and the reference ones, *per se*. What is important is that the actual shapes (especially the area difference between the inflated and the deflated shapes, which is directly related to jetting) are consistent at different values of K. Also, during time evolution they remain almost unchanged from period to period after the steady state is reached (see Fig. 2.6).

2.3 Mathematical formulations

2.3.1 Governing Equations

An immersed-boundary method is employed to solve the fluid-structure interactions involved in the aforementioned swimming process. In this approach, the motion of fluid particles is described within a Eulerian coordinate $\boldsymbol{x} \equiv (x, y)$, while the dynamics of the structure is depicted with a Lagrangian coordinate s, which denotes the arclength along the beam from one end. The structural variables include the instantaneous position $\boldsymbol{X}(s,t)$ and the corresponding velocity $\boldsymbol{V}(s,t)$, the hydrodynamic force density $\boldsymbol{F}(s,t)$, the tension $\sigma(s,t)$, the bending force density $\boldsymbol{F}_b$, the stretching force density $\boldsymbol{F}_s$, and the spring force density $\boldsymbol{F}_r$. Hereby $\boldsymbol{F}_b$ and $\boldsymbol{F}_s$ stem from the elasticity of the body itself, $\boldsymbol{F}_r$ represents the effect of the activation system. Detailed descriptions of these terms are provided later. The fluidic variables are the velocity $\boldsymbol{u}(\boldsymbol{x},t) \equiv (u, v)$, the pressure $p(\boldsymbol{x},t)$, and the body force density exerted by the immersed boundary $\boldsymbol{f}(\boldsymbol{x},t)$. Other parameters are the excessive line density of the body m_l, the bending rigidity c_b, the damping coefficients for the structure (*i.e.* the beam) λ and for the spring λ_k, the total contour length of the beam L, the fluid density ρ, the size of the exit D, the dynamic viscosity of the fluid μ, as well as the inflow velocity u_0. The governing equations for the fluid dynamics are

$$\rho\left(\frac{\partial \boldsymbol{u}}{\partial t} + \boldsymbol{u}\cdot\nabla\boldsymbol{u}\right) = -\nabla p + \mu\nabla^2\boldsymbol{u} + \boldsymbol{f}(\boldsymbol{x},t), \tag{2.1}$$

and

$$\nabla\cdot\boldsymbol{u} = 0. \tag{2.2}$$

For the structural dynamics, we have

$$m_l\frac{\partial^2\boldsymbol{X}(s,t)}{\partial t^2} + \lambda\frac{\partial\boldsymbol{X}(s,t)}{\partial t} = \boldsymbol{F}_s + \boldsymbol{F}_b - \boldsymbol{F}(s,t) + \boldsymbol{F}_r, \tag{2.3}$$

where

$$\boldsymbol{F}_s = \frac{\partial}{\partial s}[\sigma(s,t)\boldsymbol{\tau}(s,t)], \boldsymbol{\tau}(s,t) = \frac{\partial \boldsymbol{X}}{\partial s} / \left| \frac{\partial \boldsymbol{X}}{\partial s} \right|, \tag{2.4}$$

$$E_b(\boldsymbol{X},t) = \frac{1}{2}\int_{\Gamma_{ib}} c_b \left| \frac{\partial^2 \boldsymbol{X}}{\partial s^2} - \frac{\partial^2 \boldsymbol{X}^0}{\partial s^2} \right|^2 ds, \tag{2.5}$$

$$\boldsymbol{F}_b = -\frac{\wp E_b(\boldsymbol{X},t)}{\wp s} = -c_b \left(\frac{\partial^4 \boldsymbol{X}}{\partial s^4} - \frac{\partial^4 \boldsymbol{X}^0}{\partial s^4} \right), \tag{2.6}$$

and

$$\boldsymbol{F}_r(s) = \sum_{j=1}^{8} \boldsymbol{F}_{r,j}\delta(s - s_j), \quad \boldsymbol{F}_{r,j} = K\Delta \boldsymbol{x}_j - \lambda_k \partial \boldsymbol{x}_j / \partial t. \tag{2.7}$$

$\boldsymbol{\tau}(s,t)$ represents the unit tangent vector to the immersed boundary. E_b stands for the bending energy. $\boldsymbol{X}^0$ denotes equilibrium configuration of the body. $\wp$ denotes the perturbation operator [31]. $\Delta \boldsymbol{x}_j$ is the elongation of the jth spring, whose relative velocity at the ends is expressed by $\partial \boldsymbol{x}_j / \partial t$. We use the Dirac delta function δ to distribute the spring force (point force at s_j) to the structural body.

2.3.2 Fluid-structure coupling

The structural dynamics and the fluid dynamics are coupled through the following rendition using the two-dimensional Dirac delta function

$$\boldsymbol{U}(s,t) = \int_{\Omega_f} \boldsymbol{u}(\boldsymbol{x},t)\delta(\boldsymbol{x} - \boldsymbol{X}(s,t))d\boldsymbol{x}, \tag{2.8}$$

$$\partial \boldsymbol{X}(s,t)/\partial t = \boldsymbol{V}(s,t), \tag{2.9}$$

$$\boldsymbol{F}(s,t) = \alpha \int_0^t \left[\boldsymbol{U}(s,\tau) - \boldsymbol{V}\right] d\tau + \beta \left[\boldsymbol{U}(s,t) - \boldsymbol{V}\right], \tag{2.10}$$

and

$$\boldsymbol{f}(\boldsymbol{x},t)=\int_{\Gamma_{ib}}\boldsymbol{F}(s,t)\delta(\boldsymbol{X}(s,t)-\boldsymbol{x})ds, \tag{2.11}$$

where Γ_{ib} and Ω_f denote the structural and fluidic domain, respectively. $\boldsymbol{U}(s,t)$ denotes the local fluid velocity at the immersed boundary point s, which is calculated by interpolation flow velocity using delta the function. In order to enforce the structural boundary conditions, the matching between $\boldsymbol{U}$ and $\boldsymbol{V}$ is achieved through the feedback algorithm in Eqn. (2.10), which simultaneously offers us the feedback force $\boldsymbol{F}$. This strategy is similar to the PI feedback control scheme [32]. Physically, this feedback equation implies that the adjacent fluid particle and structural point are connected through a linear spring with stiffness α and damping coefficient β, which are sufficiently large negative numbers. More details on this feedback law and its numerical stability can be found in an earlier publication [33]. The interacting force $\boldsymbol{F}$ then could be distributed to the fluid domain using the delta function to update the fluid field.

2.3.3 Implementation of structural inextensibility

Since the beam is assumed to be inextensible, the tension force $\sigma(s,t)$ can be determined by solving the following equation, in which the inextensibility constraint $\tilde{\boldsymbol{\tau}}\cdot\tilde{\boldsymbol{\tau}}=1$ (where $\tilde{\boldsymbol{\tau}}=\frac{\partial \boldsymbol{X}}{\partial s}$) is imposed [34].

$$\frac{\partial^2}{\partial s^2}(\sigma\tilde{\boldsymbol{\tau}})\cdot\tilde{\boldsymbol{\tau}}=\frac{m_l}{2}\frac{\partial^2}{\partial t^2}(\tilde{\boldsymbol{\tau}}\cdot\tilde{\boldsymbol{\tau}})-m_l\frac{\partial\tilde{\boldsymbol{\tau}}}{\partial t}\cdot\frac{\partial\tilde{\boldsymbol{\tau}}}{\partial t}+\frac{\lambda}{2}\frac{\partial}{\partial t}(\tilde{\boldsymbol{\tau}}\cdot\tilde{\boldsymbol{\tau}})-\frac{\partial}{\partial s}(\boldsymbol{F}_b+\boldsymbol{F}_r-\boldsymbol{F})\cdot\tilde{\boldsymbol{\tau}}. \tag{2.12}$$

With $\sigma(s,t)$ determined, we are able to update the structural position through Eqn. (2.3) together with the following boundary conditions at the two ends

$$\frac{\partial^2\boldsymbol{X}(s,t)}{\partial s^2}=\frac{\partial^2\boldsymbol{X}^0}{\partial s^2},\frac{\partial^3\boldsymbol{X}(s,t)}{\partial s^3}=\frac{\partial^3\boldsymbol{X}^0}{\partial s^3},\sigma=0\quad\text{at } s=0 \text{ or } L \tag{2.13}$$

2.4 Numerical approach

2.4.1 Fluid solver

Following the previous studies [34–37], the Navier-Stokes equations are solved with the fractional step method on a staggered Cartesian grid. As shown in Fig. 2.3, the fluidic velocity and momentum forcing are defined on the staggered grid while the pressure is defined at the element center. In this algorithm each term in the equation (except the structural forcing term) is treated implicitly using the Crank-Nicolson scheme so that the accuracy is second order in time. The spatial derivatives are calculated using the central difference approach based on the staggered grid. Let $\mathcal{H}, \mathcal{G}, \mathcal{D}, \mathcal{L}$ be the convective, gradient, divergence and Laplacian operators, the discretized form of the Navier-Stokes equation at the $(n+1)$th time step can be written as

$$A(\boldsymbol{u}^{n+1}) + \mathcal{G}(\delta p) = \boldsymbol{r}, \mathcal{D}(\boldsymbol{u}^{n+1}) = 0, \tag{2.14}$$

where

$$A = \frac{1}{\Delta t}[\rho I + \Delta t(\rho\mathcal{N} - \frac{\mu\mathcal{L}}{2})], \tag{2.15}$$

$$\boldsymbol{r} = \frac{\rho}{\Delta t}\boldsymbol{u}^n - \mathcal{G}(p^{n-1/2}) + \frac{\mu}{2}\mathcal{L}(\boldsymbol{u}^n) + \boldsymbol{f}^n, \tag{2.16}$$

$$p^{n+1/2} = p^{n-1/2} + \delta p, \tag{2.17}$$

where I is the identity matrix, Δt denotes the time step and $\mathcal{N}$ is a linear operator for the convective term defined as

$$\mathcal{N}(\boldsymbol{u}^{n+1}) = \frac{1}{2}(\mathcal{H}(\boldsymbol{u}^{n+1}) + \mathcal{H}(\boldsymbol{u}^n)). \tag{2.18}$$

The nonlinear convective term is linearized by using a linearization scheme so that the linear convective operator only contains velocity at time step n [35].

LU decomposition and approximate factorization (approximating $\mathcal{G}(\delta p)$ with $\Delta t A\mathcal{G}(\delta p)/\rho$)

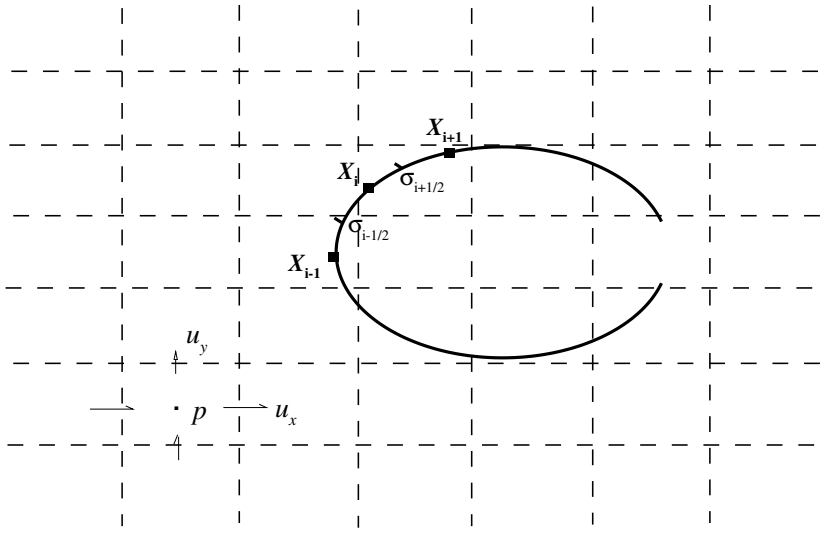

Figure 2.3: Schematic diagram of the staggered Eulerian grid and the Lagrangian coordinate system.

are employed to decouple the velocity and pressure, then Eqn. (2.14) can be rewritten in matrix form,

$$\begin{bmatrix} A & 0 \\ \mathcal{D} & \frac{-\Delta t \mathcal{D}\mathcal{G}}{\rho} \end{bmatrix} \begin{bmatrix} \boldsymbol{u}^* \\ \delta p \end{bmatrix} = \begin{bmatrix} \boldsymbol{r} \\ 0 \end{bmatrix} \tag{2.19}$$

and

$$\begin{bmatrix} I & \frac{\Delta t \mathcal{G}}{\rho} \\ 0 & I \end{bmatrix} \begin{bmatrix} \boldsymbol{u}^{n+1} \\ \delta p \end{bmatrix} = \begin{bmatrix} \boldsymbol{u}^* \\ \delta p \end{bmatrix}, \tag{2.20}$$

where $\boldsymbol{u}^*$ is an intermediate value of $\boldsymbol{u}^{n+1}$. The velocity and pressure at time level $n+1$ are then calculated via the following steps,

$$A(\boldsymbol{u}^*) = \boldsymbol{r}, \tag{2.21}$$

$$\Delta t \mathcal{D}\mathcal{G}(\delta p) = \rho \mathcal{D}(\boldsymbol{u}^*), \tag{2.22}$$

$$\boldsymbol{u}^{n+1} = \boldsymbol{u}^* - \frac{\Delta t \mathcal{G}(\delta p)}{\rho}, \tag{2.23}$$

and

$$p^{n+\frac{1}{2}} = p^{n-\frac{1}{2}} + \delta p. \tag{2.24}$$

2.4.2 Structural dynamics solver

Regarding the numerical algorithm for the structure, uniform staggered grids are also used on the body along s so that the tension σ is defined in the index $i + 1/2$ and other structural variables are defined in i ($1 \leq i \leq N$). The first, second and third-order $s-$derivatives of $\boldsymbol{X}_i$ are approximated by the central difference algorithm as

$$\mathcal{D}_s \boldsymbol{X}_i = (\boldsymbol{X}_{i+1/2} - \boldsymbol{X}_{i-1/2})/\Delta s, \tag{2.25}$$

and

$$\mathcal{D}_{ss}\boldsymbol{X}_i = (\boldsymbol{X}_{i+1} - 2\boldsymbol{X}_i + \boldsymbol{X}_{i-1})/\Delta s^2, \tag{2.26}$$

where Δs is the body grid size. The discretizated form of Eqn. (2.3) is now written as

$$\boldsymbol{X}^* = 2\boldsymbol{X}^n - \boldsymbol{X}^{n-1}, \tag{2.27}$$

and

$$\begin{aligned} & m_l \frac{\boldsymbol{X}_i^{n+1} - \boldsymbol{X}_i^*}{\Delta t^2} + \lambda \frac{\boldsymbol{X}_i^{n+1} - \boldsymbol{X}_i^n}{\Delta t} \\ = \quad & [\mathcal{D}_s(\sigma^* \mathcal{D}_s \boldsymbol{X}^{n+1})]_i - c_b[\mathcal{D}_{ss}(\boldsymbol{X}^{n+1} - \boldsymbol{X}^0)_{i+1} - 2\mathcal{D}_{ss}(\boldsymbol{X}^{n+1} - \boldsymbol{X}^0)_i \\ & + \mathcal{D}_{ss}(\boldsymbol{X}^{n+1} - \boldsymbol{X}^0)_{i-1}]/\Delta s^2 - \boldsymbol{F}_i^n + (\boldsymbol{F}_r^*)_i, \quad i = 2 \cdots N-1. \end{aligned} \tag{2.28}$$

At the free ends $i = 1$ and N, the boundary conditions (Eqn. (2.13)) are applied so that the right hand side of Eqn. (2.28) at these two ends becomes, respectively,

$$RHS = 2(\sigma^* \mathcal{D}_s \boldsymbol{X}^{n+1})_{1+1/2}/\Delta s - 2c_b \mathcal{D}_{ss}(\boldsymbol{X}^{n+1} - \boldsymbol{X}^0)_2/\Delta s^2 - \boldsymbol{F}_1^n + (\boldsymbol{F}_r^*)_1, \tag{2.29}$$

and

$$RHS = -2(\sigma^* \mathcal{D}_s \boldsymbol{X}^{n+1})_{N-1/2}/\Delta s + 2c_b \mathcal{D}_{ss}(\boldsymbol{X}^{n+1} - \boldsymbol{X}^0)_{N-1}/\Delta s^2 - \boldsymbol{F}_N^n + (\boldsymbol{F}_r^*)_N, \tag{2.30}$$

where the superscript '$*$' denotes the intermediate time step. The spring force term $\boldsymbol{F}_r^*$ is explicitly calculated through the intermediate position $\boldsymbol{X}^*$, whereas the tension force $\sigma_{i+1/2}^*$ is implicitly

computed by solving Eqn. (2.12), whose discretized form is

$$\mathcal{D}_{ss}(\sigma^*_{i+1/2}\tilde{\boldsymbol{\tau}}^*_{i+1/2})\cdot\tilde{\boldsymbol{\tau}}^*_{i+1/2} = m_l[1-2(\tilde{\boldsymbol{\tau}}\cdot\tilde{\boldsymbol{\tau}})^n_{i+1/2}+(\tilde{\boldsymbol{\tau}}\cdot\tilde{\boldsymbol{\tau}})^{n-1}_{i+1/2}]/2\Delta t^2 +$$
$$\lambda[1-(\tilde{\boldsymbol{\tau}}\cdot\tilde{\boldsymbol{\tau}})^n_{i+1/2}]/2\Delta t - m_l(\mathcal{D}_s\boldsymbol{V}\cdot\mathcal{D}_s\boldsymbol{V})^n_{i+1/2} - [\mathcal{D}_s(\boldsymbol{F}^*_b+\boldsymbol{F}^*_r-\boldsymbol{F}^n)]\cdot\tilde{\boldsymbol{\tau}}^*_{i+1/2},$$

where $\tilde{\boldsymbol{\tau}}^*_{i+1/2} = \mathcal{D}_s\boldsymbol{X}^*_{i+1/2} = \frac{\boldsymbol{X}^*_{i+1}-\boldsymbol{X}^*_i}{\Delta s}$, $i = 1,\cdots,N-1$.

The fluid-structure interaction Eqns. (2.8) to (2.11) are discretized as

$$\boldsymbol{U}^n_i = \sum_{\boldsymbol{x}} \boldsymbol{u}^n_i(\boldsymbol{x})\delta_h(\boldsymbol{x}-\boldsymbol{X}^n_i)\Delta x\Delta y, \tag{2.31}$$

$$\boldsymbol{V}^n_i = (\boldsymbol{X}^n_i - \boldsymbol{X}^{n-1}_i)/\Delta t, \tag{2.32}$$

$$\boldsymbol{F}^n_i = \alpha\sum_{j=1}^{n}(\boldsymbol{U}^j_i-\boldsymbol{V}^j_i)\Delta t + \beta(\boldsymbol{U}^n_i-\boldsymbol{V}^n_i), \tag{2.33}$$

and

$$\boldsymbol{f}^n = \sum_s \boldsymbol{F}^n_i(s)\delta_h(\boldsymbol{x}-\boldsymbol{X}^n_i(s))\Delta s, \tag{2.34}$$

where $\Delta x, \Delta y$ are the sizes of the uniform grids around the body. In the following simulations, we use mesh size $\Delta x = \Delta y = h$ in both x and y directions near the immersed boundary. The Dirac delta function δ is approximated by a smoothed delta function δ_h so that

$$\delta_h(\boldsymbol{x}) = h^{-2}\phi\left(\frac{x}{h}\right)\phi\left(\frac{y}{h}\right), \tag{2.35}$$

where

$$\phi(r) = \begin{cases} \frac{1}{8}(3-2|r|+\sqrt{1+4|r|-4r^2}) & 0\le|r|<1 \\ \frac{1}{8}(5-2|r|+\sqrt{-7+12|r|-4r^2}) & 1\le|r|<2 \\ 0 & 2\le|r| \end{cases} \tag{2.36}$$

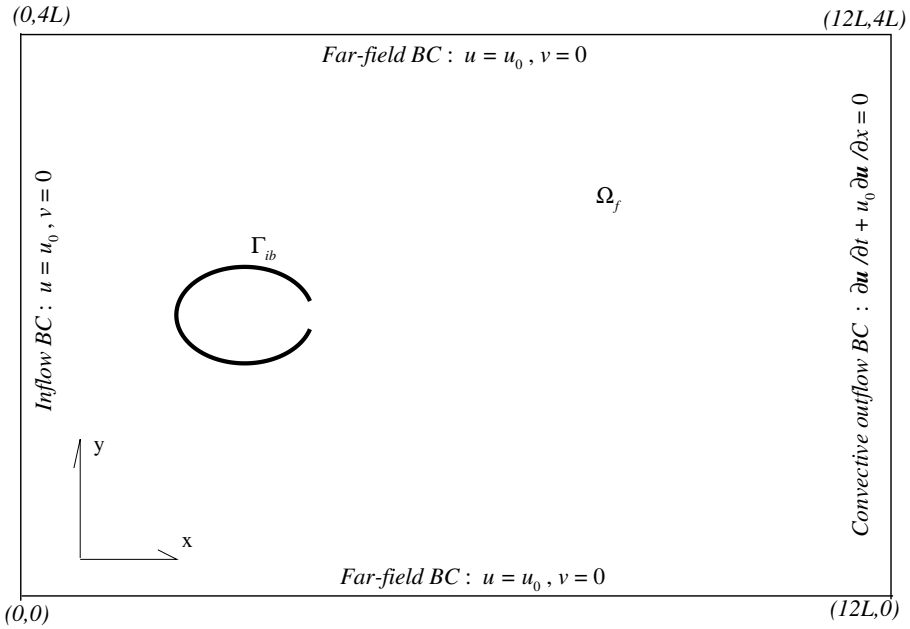

Figure 2.4: The computational domain and boundary conditions (not to scale).

The validation of this method was elaborated in previous studies through comparisons with benchmark results (theoretical studies, numerical results, and experimental measurements). Specifically, the accuracy of the fluid solver has been demonstrated in simulations of flow around a stationary cylinder, cylinder with prescribed oscillations [36],an accelerating plate, and an oscillatory wing [37]. The structural solver has been validated by simulating the dynamics of a hanging filament [37]. Finally, the validity and accuracy if the fluid-structure coupling algorithm have been corroborated through simulations of an elastic ring [38], an elastically mounted cylinder [36], a flexible flag, two side-by-side filaments, and galloping motions of rectangular objects [39].

2.5 Tethered swimming mode

To illustrate the propelling performance of the system shown in Fig. 2.2, we conduct numerical simulations by using the immersed-boundary algorithm depicted in the previous section. Specifically, in this section we concentrate upon a tethered motion case in which the body is fixed at its front end. This is achieved by mooring the front point of the body with a stiff spring.

We use thrust coefficient C_T (here we define the generated thrust as the net axial force acting on the body), hydrodynamic efficiency η_h and mechanical efficiency η_m to measure the propelling performance of the system. C_T is obtained by

$$C_T = \frac{F_T}{\rho u_0^2 L} \tag{2.37}$$

and

$$F_T = -\int_{\Gamma_{ib}} F_x(s,t)ds. \tag{2.38}$$

In the tethered case with a constant incoming flow speed, we define a hydrodynamic efficiency as

$$\eta_h = \frac{\overline{F}_T u_0 T}{P}, \tag{2.39}$$

where $\overline{F}_T$ is the average thrust in a deformation period T, P represents the overall power expenditure per cycle, which is expressed by

$$P = \int_T \int_{\Gamma_{ib}} \boldsymbol{F} \cdot \boldsymbol{U} ds dt. \tag{2.40}$$

The potential energy stored in the springs is calculated by

$$PE = \sum_{j=2}^{8} \frac{1}{2} K \left| \Delta \boldsymbol{x}_j \right|^2. \tag{2.41}$$

So the mechanical efficiency η_m is

$$\eta_m = \frac{\overline{F}_T u_0 T}{2 \times \Delta PE}, \tag{2.42}$$

where ΔPE is the overall spring potential energy released in deflation(or inflation), which is equivalent to the maximum value of PE.

Using the fluid density ρ, the incoming flow speed u_0, the contour length L of the body, and characteristic time $T_0 = L/u_0$ as the reference variables, all results will be presented in normalized form. The Reynolds number is defined as

$$R_e = \frac{\rho u_0 L}{\mu}, \tag{2.43}$$

which will be chosen to be 400 for all simulations of tethered mode. At lower Reynolds number the thrust-generation performance of our system tends to be low. If the Reynolds number is high, on the other hand, the effect of symmetry-breaking instability is more pronounced (see §2.5.3).

As depicted in Fig. 2.2, driven by the internal springs (with stiffness K and damping coefficient λ_k), the reference shape of the body varies periodically at frequency $f \equiv 1/T$ between the swollen state with eccentricity $e_0 = 0$ and the slender state with eccentricity $e_1 = 0.99$ in a uniform flow u_0. The body stiffness c_b is determined through numerical tests so that it is sufficiently large to prevent buckling and ensure smooth body deformations, yet small enough so that the discrepancy between the body deformations at difference values of spring stiffness K is not significant (as mentioned earlier, this discrepancy is associated with the finite value of potential energy stored in the beam so that the strain energy in the springs will not be completely released). Besides, when the beam is sufficiently soft it does not induce large initial vibrations at the beginning of each simulation. Thus determined, the combinations of K and the corresponding bending stiffness c_b used in our simulations are included in Table. 2.1.

As shown in Fig. 2.4, the computational domain is chosen to be a rectangular box with

Table 2.1: Combinations of K and c_b (in non-dimensional form).

$K/\rho u_0^2$	0.5-1.5	2.0-4.5	6-12	15-40
$c_b/\rho u_0^2 L^3$	0.01	0.02	0.03	0.05

Table 2.2: List of parameters used in the simulations.

m_l	λ	λ_k/K	α	β	N	Δt	Δx,Δy
$10^{-4}\rho L$	$0.01\rho u_0$	$0.05T_0$	$-10^5\rho u_0^2/L$	$-100\rho u_0$	300	$3.0\times10^{-5}T_0$	$0.004L$

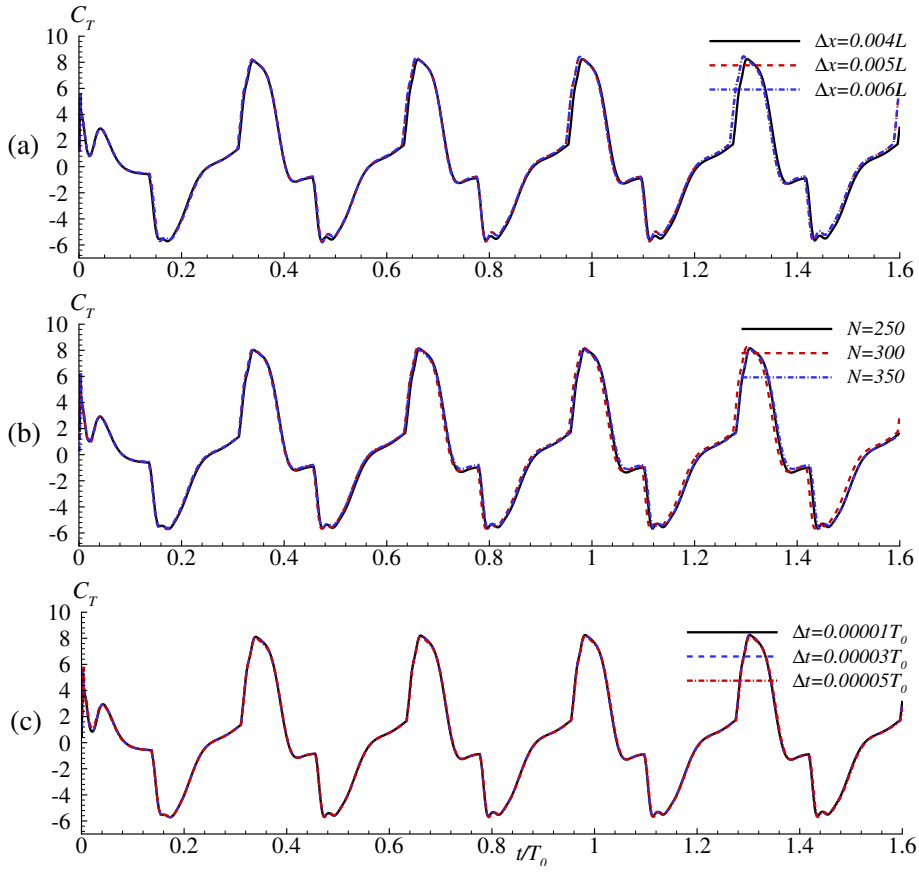

Figure 2.5: (a) Sensitivity of C_T with respect to fluid grid size Δx ($N = 300$ and $\Delta t = 3 \times 10^{-5}T_0$). (b) The effect of the number of Lagrangian element on C_T ($\Delta x = 0.004L$ and $\Delta t = 3 \times 10^{-5}T_0$). (c) Sensitivity of C_T with respect to the time step ($N = 300$ and $\Delta x = 0.004L$). $K = 15\rho u_0^2$, $D = 0.1L$.

$0 \leq y \leq 4L, 0 \leq x \leq 12L$. Dirichlet boundary condition is applied in inflow and far-field boundaries, whereas convective boundary condition is used in outflow. The initial mass center of the body is located at $(2L, 2L)$. Sensitivity tests have been conducted to ensure that the results are not sensitive to the spatial and temporal steps (see Fig. 2.5). Based on these tests, in the following simulations the number of Lagrangian elements and the time step are chosen to be 300 and $3 \times 10^{-5} T_0$, respectively. Uniform fluid grids with $\Delta x = \Delta y = 0.004L$ are used in the vicinity of the body and grids are stretched outside towards the boundary [36]. Other parameters used in this study are listed in Table 2.2.

2.5.1 Steady-state responses

To check if the activation algorithm we apply meets the requirements for consistency (*i.e.* not sensitive to K) and periodicity (*i.e.* minimum variations from period to period), in Fig. 2.6a and b we plot the inflated and deflated shapes of the body at two different values of K. For comparison the referent shapes (with eccentricities e_1 and e_0, respectively) are also plotted. It is seen that although there do exist certain differences between the reference shapes and the actual body shapes due to the finite bending stiffness of the beam and the fluid dynamic force, the differences between the body shapes obtained at different values of K are relatively small. For further illustration in Fig. 2.6c we plot the time histories of the area change $\Delta\forall$, defined as the difference between the internal area at the inflated state and that at the deflated state. After the first period the value of $\Delta\forall$ remains steady. Moreover, the difference between $\Delta\forall$ obtained with the two different values of K is negligibly small. Indeed, in all the cases we study once the steady state is established the variation of $\Delta\forall$ at steady state is less than 3%.

Figure 2.7 demonstrates the steady state response of a typical case (usually it takes just one period for the steady state to be reached). In Fig. 2.7a, we plot time histories of the internal area of the body ($\forall$) and the potential energy stored in the springs (PE) of the typical case. As designed,

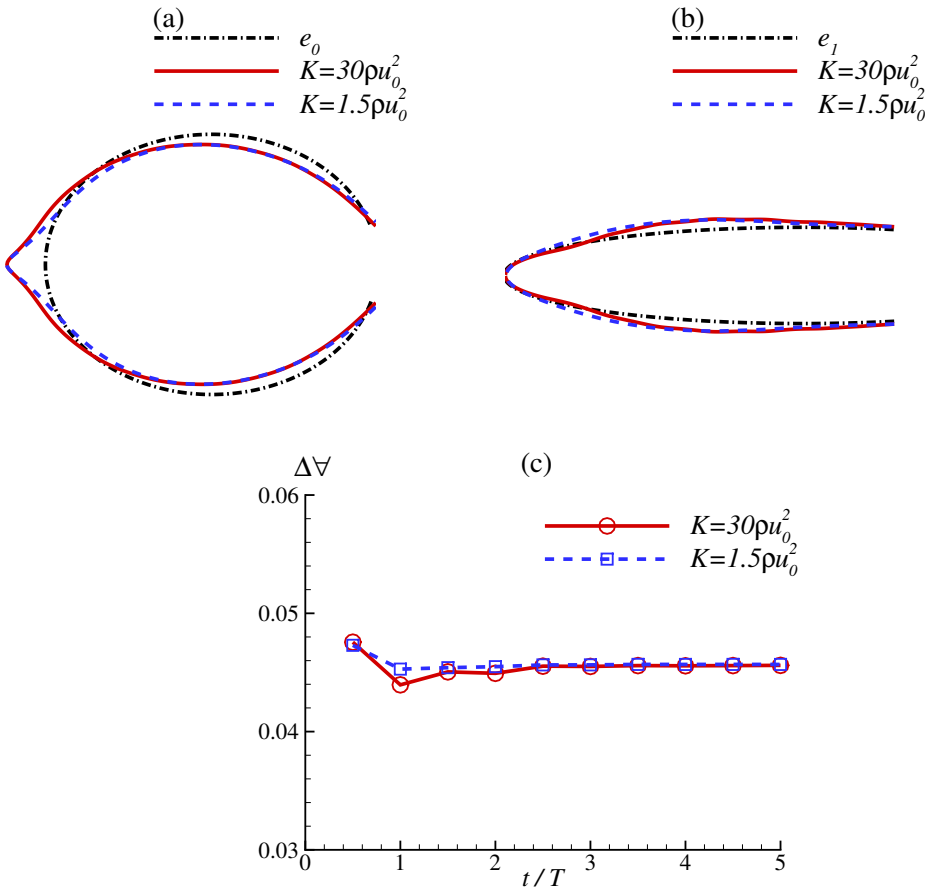

Figure 2.6: (a) Inflated shapes of the reference state (e_0) and the actual states with different values of K. (b) Deflated shapes of the reference state (e_1) and the actual states with different values of K. All of these shapes are obtained in the fourth period. (c) Time histories of the internal area change $\Delta\forall$ (*i.e.* the internal area of the inflated shape minus that of the deflated shape). In each period two data points are obtained, one from the deflation phase and the other from the inflation phase. $D = 0.1L$.

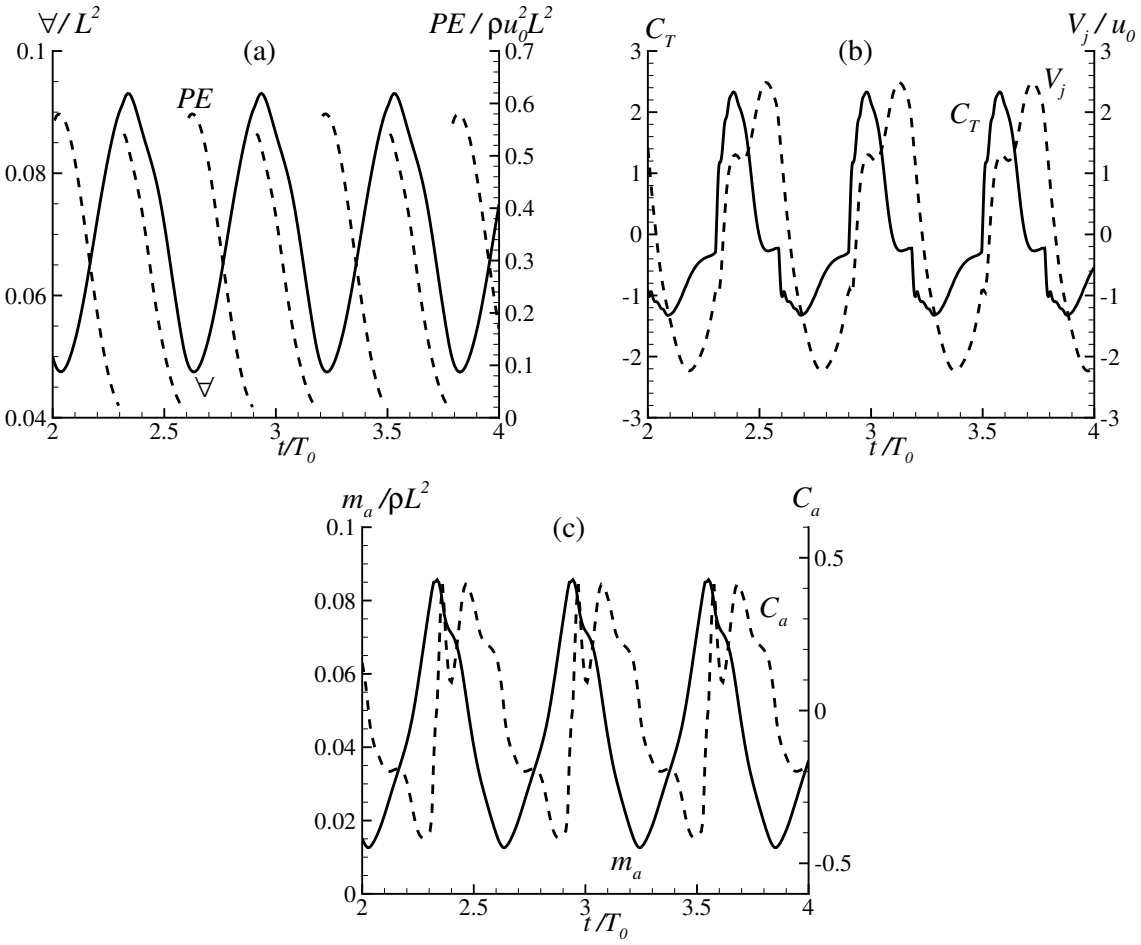

Figure 2.7: Time histories of (a) internal area $\forall$ and strain energy PE, (b) thrust C_T and jet speed V_j, and (c) added mass m_a and added-mass-related thrust coefficient C_a. $K = 3.0\rho u_0^2$, $D = 0.1L$.

the instantaneous potential energy in the springs jumps to a peak right after $\forall$ reaches its maximum or minimum point (corresponding to the switching of the unstretched lengthes of the springs). It is then released gradually to drive the body deformation in the following phase.

Figure 2.7b displays the time histories of average jet speed and the thrust force coefficient C_T the system generates. Hereby the average jet speed is calculated as $V_j = -\frac{1}{D}\frac{d\forall}{dt}$. It is seen that thrust generation is achieved in the deflation phase, where $V_j > 0$. During the inflation phase ($V_j < 0$) negative values of C_T is observed. Its magnitude is relatively low so that the time averaged thrust in this particular case is still positive. There exists, however, a clear phase difference between V_j and C_T, which is attributed to the time varying drag force the body sustains and fact that jet momentum is not the only thrust source, the variation of the internal fluid momentum and the over pressure at the orifice exit (which are more or less related to jet acceleration) make fairly large contribution to thrust generation during the unsteady jetting (see §3.4).

Time variations of the added mass m_a and its contribution to thrust generation $C_a = F_a/\rho u_0^2 L$ where $F_a = -\dot{m}_a u_0$, are plotted in Fig. 2.7c. The instantaneous configuration of the body is simplified as an ellipse with semi-minor axis b so that the added mass can be expressed as $m_a = \rho\pi b^2$. Since the swimmer speed u_0 is constant in this case, although the magnitude of C_a is in the same order as that of C_T, its time averaged value is negligibly small so that it has almost no contribution to the average thrust. This result, however, is closely associated with the tethered swimming assumption. In free swimming scenario the forward speed is high during the deflation phase ($\dot{m}_a < 0$) and low during the inflation phase ($\dot{m}_a > 0$), so that a positive value of time averaged C_a is reached. This effect will be included in our studies of free swimming cases.

The evolution of the near-body flow field is shown in Fig. 2.8. It is seen that aside from the vortices inside the pressure chamber, two pairs of counter-rotating vortices are generated within one inflation-deflation period and prorogate downstream into the wake, one pair from the outer surface of the body and the other from the exit. These vortices are shed in a staggered way -

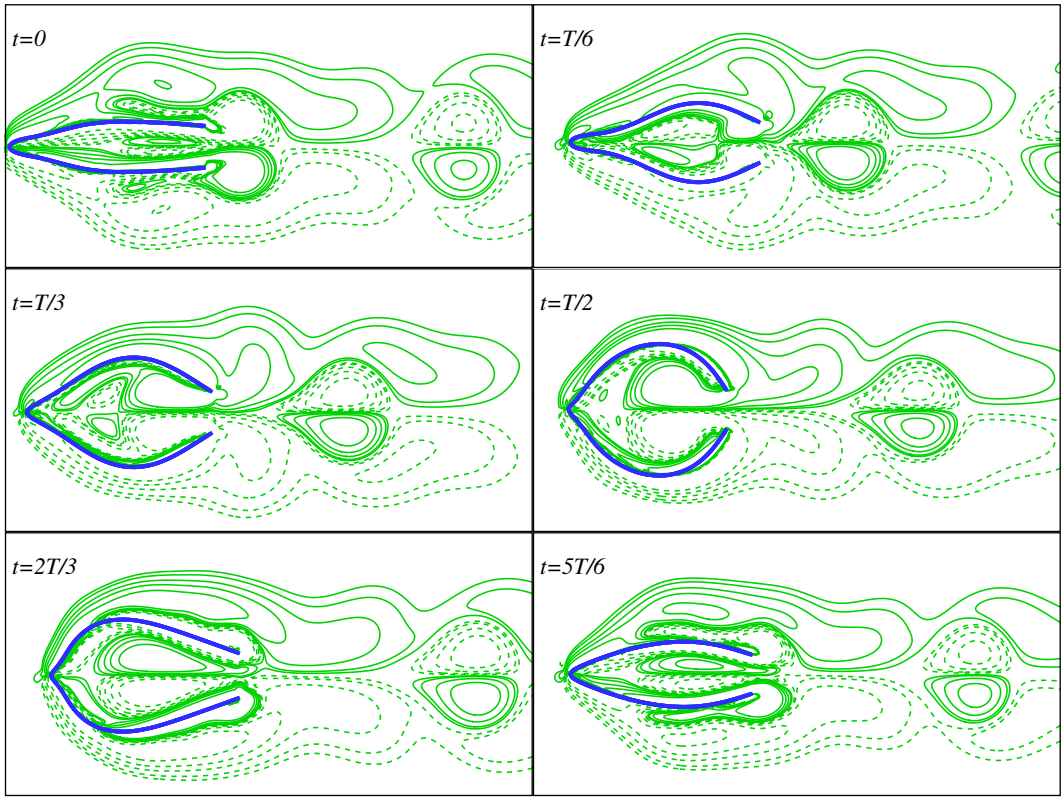

Figure 2.8: Evolution of the near-body flow field (visualized through the vorticity contour) within an inflation-deflation period T. The positive values of vorticity (solid lines) correspond to clockwise vortices. The negative vorticity (dashed lines) represent counter-clockwise vortices. $K = 3.0\rho u_0^2$, $D = 0.1L$.

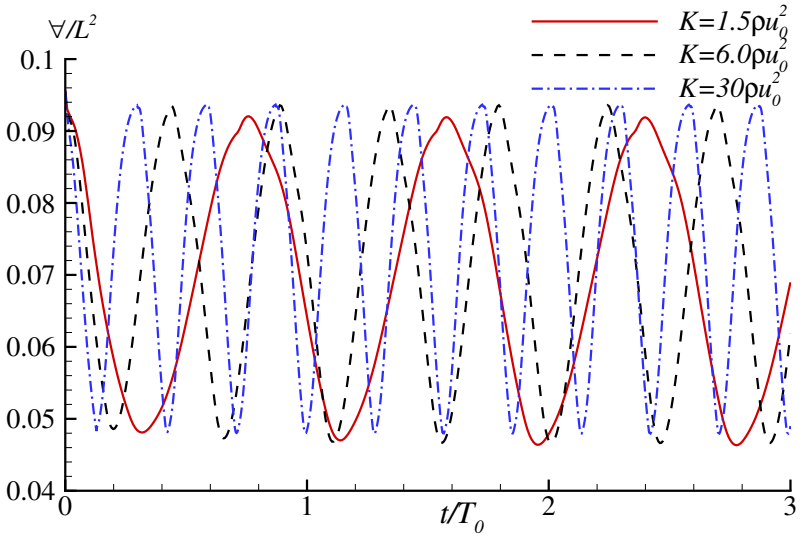

Figure 2.9: Variations of the internal area during the locomotion at different frequencies when $D = 0.1L$.

the body-originated vortices are developed during the inflation phase (from $t = 0$ to $T/2$ in the figure; note that for clarity in this figure we redefine the time corresponding to the starting of the inflation phase as $t = 0$), whereas the exit vortices (which are closely related to the jet flow) are created during the deflation phase (starting at $t = T/2$). These vortices form a complicated, yet well-organized and symmetric (with respect to the $x-$ axis) wake behind the body, before it is disturbed and eventually destroyed by a symmetry-breaking instability (see §2.5.3).

The flow field produced by our system bears certain resemblance to the experiments and simulations of a tube which generates a jet *via* an internal piston [1, 40, 41]. In both cases the vortices generated by the jet and those by the body itself coexist in the wake. However, in our case the body-shed vortices and the exit-shed vortices are generated in a staggered manner through the body deformation. This effect was not considered in the those studies since the body they considered (a tube with a piston inside) was rigid.

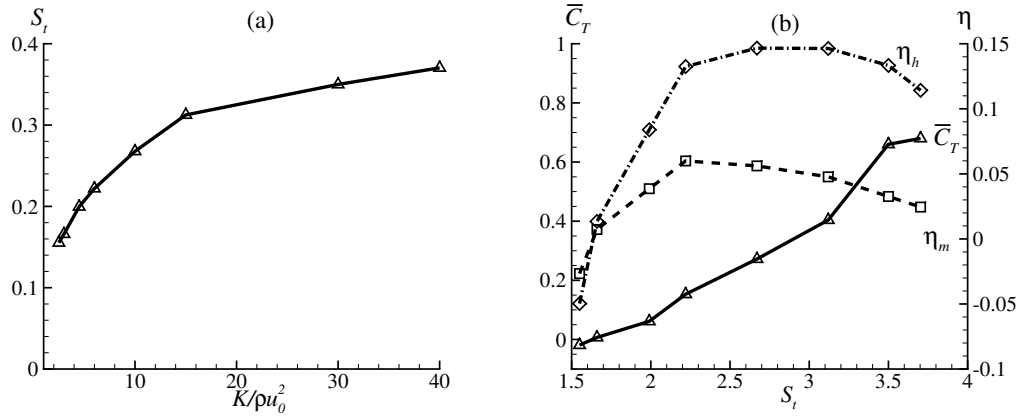

Figure 2.10: (a) Variation of S_t as functions of K, (b) mean thrust coefficient $\overline{C}_T$, hydrodynamic efficiency η_h and mechanical efficiency η_m as functions of S_t. $D = 0.1L$.

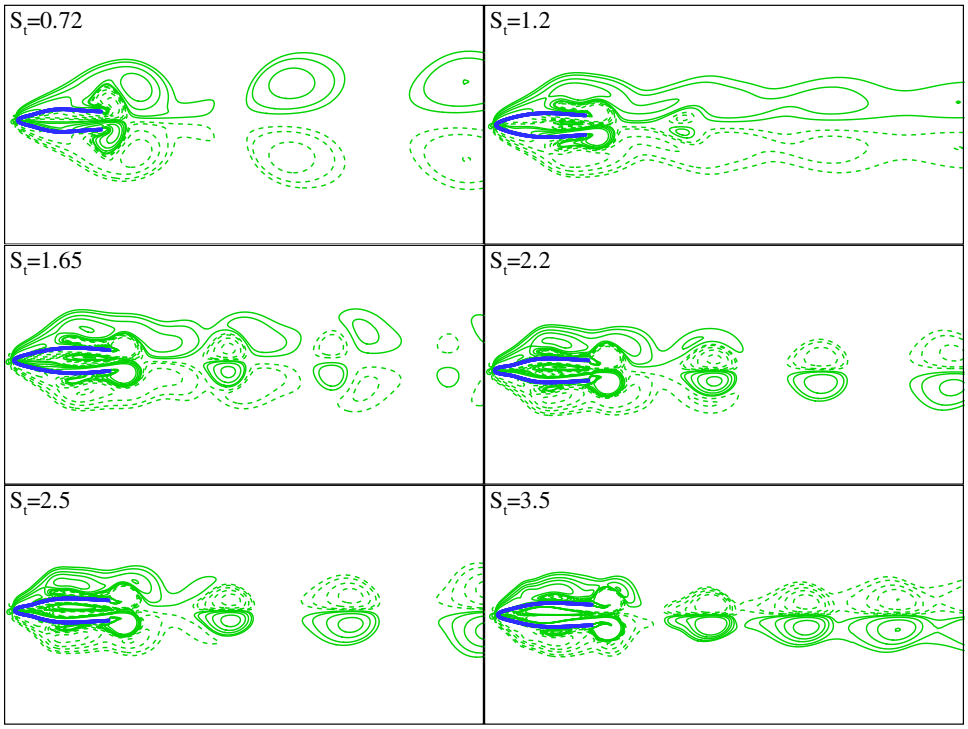

Figure 2.11: Wake patterns visualized through vorticity contour at various S_t. These snapshots are drawn when the body is at its fully deflated state. $D = 0.1L$.

2.5.2 Parametric studies

The dynamics of the system are expected to be dependent upon physical parameters such as the frequency of the body oscillation and size of the exit/inlet D. With other parameters fixed, the oscillation frequency f (or, alternatively, the Strouhal number $S_t \equiv fL/u_0$) is determined by the stiffness of the internal springs K. Figure 2.9 plots the time histories of the internal area Λ at different values of spring constant K. It shows stronger springs create higher frequency motions. This tendency is shown more clearly in Fig. 2.10a, which also demonstrates that the growth rate of the $S_t - K$ curve decreases with K. Subsequently, beyond a certain point (*e.g.* $K = 40$) it is difficult to further increase S_t through K. For that reason, our simulations are confined within certain range of S_t. As demonstrated in Fig. 2.10b, where variations of the mean thrust coefficient $\overline{C}_T$, the hydrodynamic efficiency η_h, and the mechanical efficiency η_m on different values of S_t are plotted, the body sustains drag at low S_t (*e.g.* $\overline{C}_T = -0.062$ at $S_t = 1.5$) and produces thrust at relatively high values of S_t. It shows that higher values of S_t tend to produce larger thrust $\overline{C}_T$ while the propulsive efficiencies (both mechanical and hydrodynamic) are found to reach peaks at a certain S_t (in this case, the highest points of η_h and η_m occur at $S_t = 2.5$ and 2.2, respectively).

To understand the dependence of the propulsive performance of this system upon the oscillation frequency and its correlation with the near-body flow field, we draw the snapshots of the vorticity field around the body at different values of S_t. As shown in Fig. 2.11, there exist three distinctive wake patterns. The first pattern, occurring at low frequency ($S_t = 0.72$ and 1.2 in the figure), is dominated by the vortices that are shed from the outside of the solid boundary (mostly in the inflation phase). These vortices are organized into vortex pairs. During each oscillatory cycle one pair of vortices is generated. The rotational directions of these vortices are consistent with those in a drag-type wake. Vortex pairs that are generated from the exit in deflation phase, by comparison, are much weaker than the body-shed ones. Right after shedding they are dissipated away rapidly.

At higher values of S_t the second wake pattern appears, where these two types of vortices (exit-generated vortices and body-generated ones) are comparable in strength (see Fig. 2.11 at $S_t = 1.65$). Consequently, these coexisting vortices interact with each another and propagate downstream together. The third wake pattern occurs when the deformation frequency is further increased (see, *e.g.* $S_t = 2.5$). Under this condition, the wake structure is dominated by the exit vortices so that the vorticity distribution displays the opposite scenario against the first pattern (*i.e.* a thrust wake). Upon closer inspection, it is found that the maximum hydrodynamic efficiency η_h is reached at $S_t = 2.5$, which roughly coincides with the transition to the exit-vortex-dominated wake pattern.

Figure 2.12 displays the pressure distribution in the near-body flow field at three distinctive wake patterns ($S_t = 0.72, 1.65$ and 3.5) and the corresponding time histories of thrust the swimmer produces. Two snapshots of pressure contours are plotted for each case, obtained during the deflation($t = T/4$) and the inflation ($3T/4$) phases. A high speed jet flow is generated at the exit during the deflation phase, leading to a high pressure area in the rear side of the swimmer. The front side of the body, on the contrary, is surrounded by negative pressure as the shrinking body backs away from the fluid. As a result, positive thrust is created. The above phenomenon becomes more pronounced as S_t increases, leading to larger thrust generation. The high pressure region in the rear created in the earlier deflation phase will be gradually neutralized in the following inflation process. Consequently, a low pressure area will appear in the rear. Together with high pressure environment in the front, a negative thrust is created. In the case of $S_t = 0.72$ where the jet speed is relatively low, the high pressure effect in the deflation phase is weak so that the thrust force generated in the contraction process is insufficient to overcome the resistance effect in the inflation phase, resulting in negative average thrust over a cycle. On the other hand, when $S_t = 3.5$, the jetting process is strong enough so that the high pressure effect is able to dominate the rear of the body in the deflation phase. Even in the inflation phase there could be small positive pressure area

near the exit as the high pressure field created in the deflation phase is sucked back (see the case with $S_t = 3.5$ at $3T/4$). Thus a positive average thrust is generated under this condition. The case of $S_t = 1.65$ is a transition between those two scenarios.

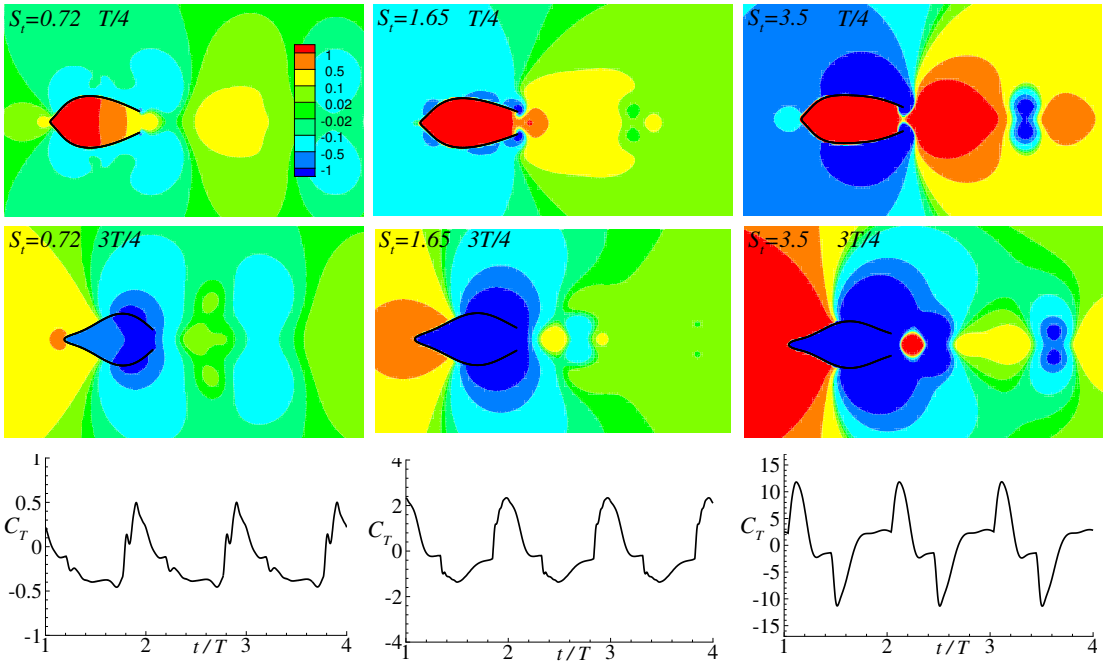

Figure 2.12: (Top) Pressure (normalized by ρu_0^2) contours in the near-body flow field and (bottom) time histories of thrust at $S_t = 0.72, 1.65$, and 3.5.

The interpretation of these results involves the interplay between the drag effect and the jet-related thrust generation. In this system the horizontal force generation comes from three sources: 1) the viscous drag on the body, which is associated with the body-shed vortices; 2) the repulsive force from the jet, which is represented by the exit-generated vortices; and 3) the added-mass related thrust. Among these three the added-mass effects play a negligibly small role in mean force generation due to the tethered motion assumption (see §2.5.1 for a discussion). When the oscillation frequency is low the jet effect is weak - the jet speed at the exit is roughly given as $-\frac{1}{D}\frac{d\Lambda}{dt}$. In these cases the net thrust production is negative or small since the weak jet is not able to overcome the drag. The propulsive efficiency is thus low, albeit the energy expenditure may also be

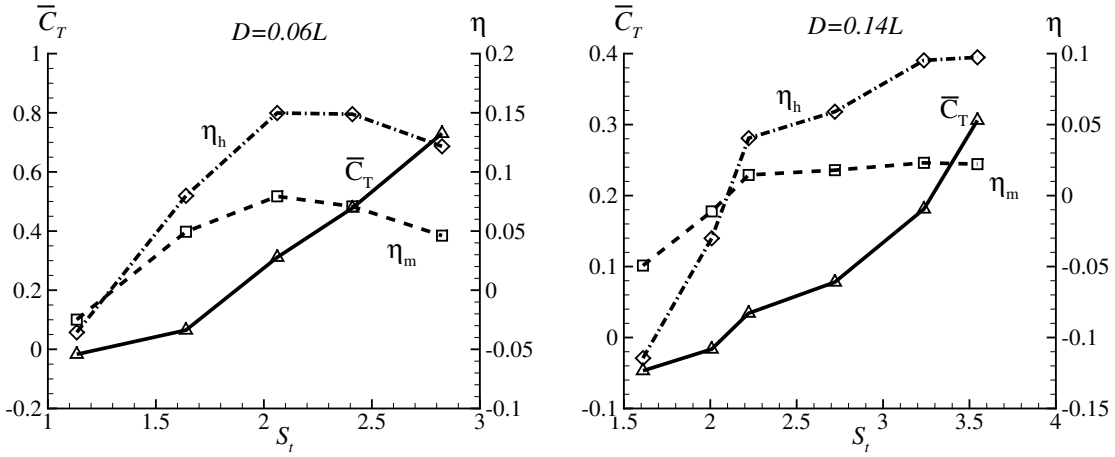

Figure 2.13: Mean thrust $\overline{C}_T$, mechanical efficiency η_m and hydrodynamic efficiency η_h as functions of S_t at $D = 0.06$ and 0.14.

low. With the increasing frequency, the production of thrust rises with the strength of the jet, so does the propulsive efficiency. At higher frequency, however, the efficiency decreases when the jet is too strong.

Another parameter that significantly affects the dynamic of the system is the size of the exit D. In the following we consider different exit diameters ($D = 0.06L$ and $0.14L$) to explore the performance of the system as well as wake characteristics. This range of D is a bit higher than the relative size of the orifice of a squid. The reason is that due to morphological restrictions the volume change of the mantel cavity (corresponding to the volume of water discharged in each jetting) of a squid is limited. The diameter of the funnel tube has to be small to reach sufficient jet speed. Our squid-inspired system does not have this issue. On the other hand, in our system small exit leads to stronger wake, which tends to become unstable after small number of cycles (see §2.5.3).

As demonstrated in Fig. 2.13a, the results (*i.e.* the dependance of thrust generation and efficiencies upon S_t) at $D = 0.06L$ are similar to $D = 0.1L$. The mean thrust C_T increase monotonously with S_t, whereas both η_m and η_h are maximized at $S_t = 2.05$, a bit below the

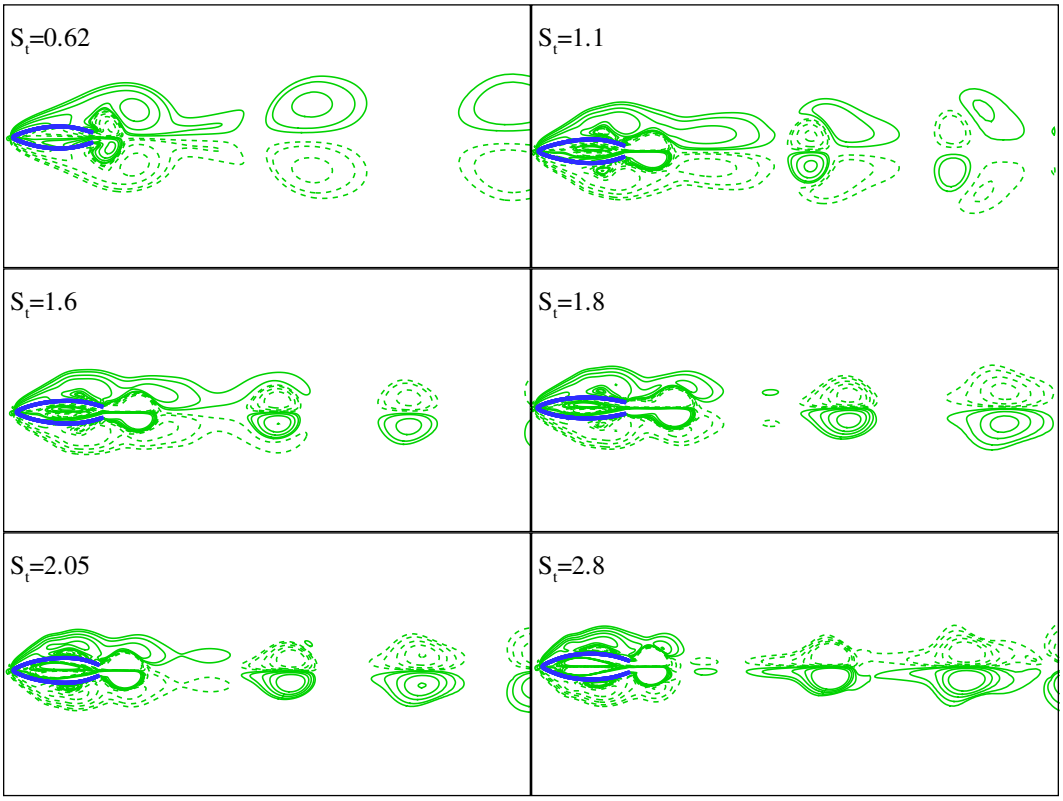

Figure 2.14: Same as Fig. 2.11 except that $D = 0.06L$.

Strouhal numbers corresponding to peak efficiencies in the case of $D = 0.1L$. This is explained by the fact that at the same oscillation frequency, smaller exit increases the speed of the jet flow (and, subsequently, the jet-related thrust generation), while its effect on the drag force (associated with the body-generated wake) is not that big.

Figure 2.14 displays the wake signatures at different frequencies when $D = 0.06L$. All the three distinctive wake patterns are observed in the range of $S_t \in (0.62, 2.8)$. Most importantly, the case of $S_t = 2.05$, in which the highest efficiency is obtained, also lies at the border between the second and the third wake patterns.

The case when $D = 0.14L$, however, is different from the previous two ($D = 0.06L$ and $0.1L$). As shown in Fig. 2.13b, in this case there is no peak for neither the mechanical efficiency η_m nor the hydrodynamic efficiency η_h within the achievable range of S_t, although the mean thrust

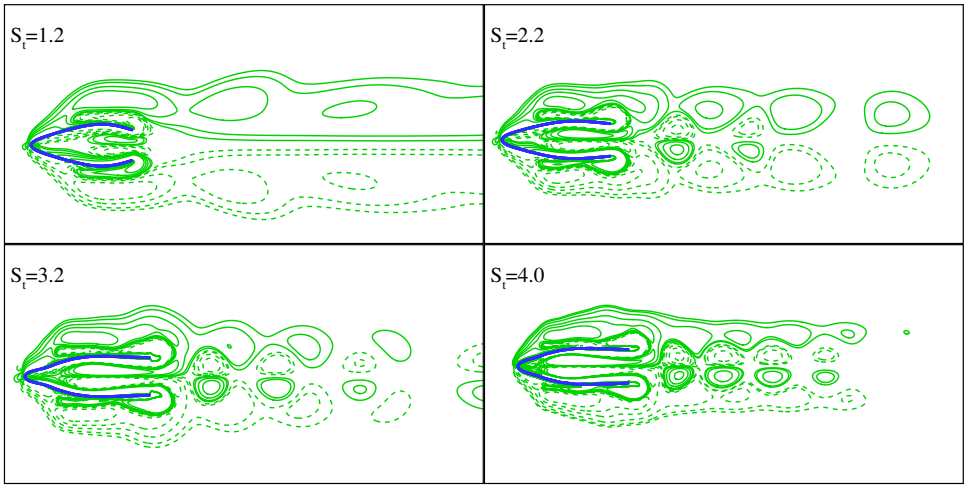

Figure 2.15: Same as Fig. 2.11 except that $D = 0.14L$.

displays the same tendency, *i.e.* it monotonously increases with respect to S_t. The corresponding wake structures are illustrated in Fig. 2.15. It is seen that considerable body-shed vortices remain in the wake over the whole range of S_t that can be reached. It is thus consistent with our observation that the highest propulsive efficiency is achieved at the lowest S_t when the exit vortices dominate the wake.

2.5.3 Symmetry-breaking instability

As mentioned earlier, in our system it takes just one inflation-deflation period to reach steady state. However, in many cases the swimmer can only stay in this state for about $6 \sim 9$ cycles before a symmetry-breaking instability steps in. The consequence of the symmetry-breaking instability on the propulsive performance of the system is clearly demonstrated in Fig. 2.16a, where time histories of the thrust coefficient C_T and the transverse force coefficient C_y are plotted. It shows that lateral force becomes significant around $t = 6.5T_0$. This is also accompanied by decreases in thrust generation, since part of the energy input is utilized to generate the transverse force instead. Further examinations show that the symmetry-breaking instability exists in all cases

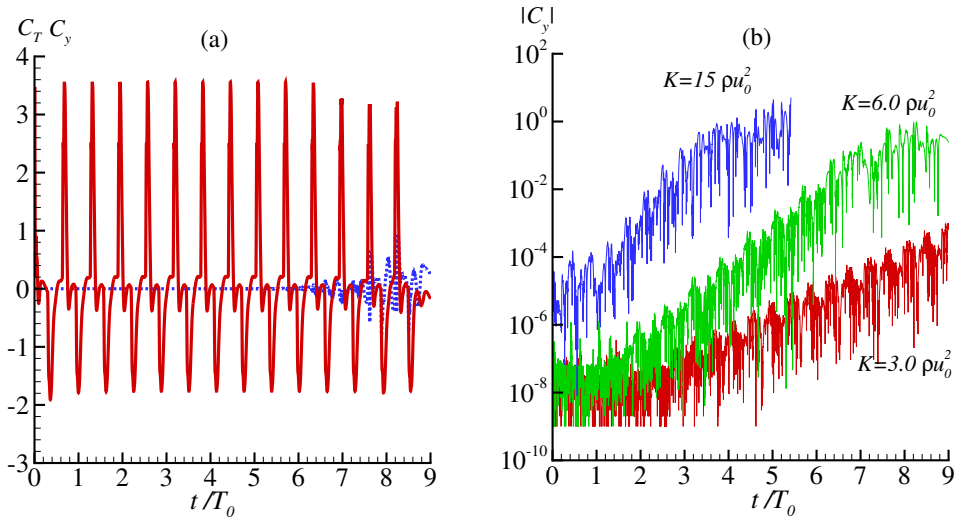

Figure 2.16: (a) Time histories of C_T (solid line) and C_y (dashed line) at $K = 6.0\rho u_0^2$. (b) Time histories of $|C_y|$ for $K = 3.0, 6.0, 15\rho u_0^2$ (for clarity in these three curves the points when $|C_y|$ approaches zero are not included). $D = 0.06L$.

(see Fig. 2.16b). However, in some of the cases we study (*e.g.* the one with $K = 3.0\rho u_0^2$ in Fig. 2.16b) it grows so slowly that within the limited simulation time its effect is not shown. A typical process of such a transition is depicted in Fig. 2.17. It is seen that the instability starts in the wake and eventually affects the deformation of the body itself. For example, when $t = 6.0T_0$ the configuration of the body is almost symmetric, although the wake displays a little asymmetric disturbance. After that, the disturbance in the wake grows quickly with time and its induced velocity soon destroys the symmetric pattern in body deformation (see the snapshot at $t = 6.9T_0$). This phenomenon suggests that the symmetric wake pattern in steady state is unstable and can easily be disturbed under certain perturbation.

The symmetric-breaking instability leads to three issues on the propulsive performance of our system: the need to overcome the lateral force and maintain straight line swimming, the decreased thrust force and propulsive efficiency, and the difficulty to control the body deformation. Indeed, due to deformations associated with fluid-structure interaction it is often impossible to continue the simulation by using the activation method specified in §2.2 since the strain energy

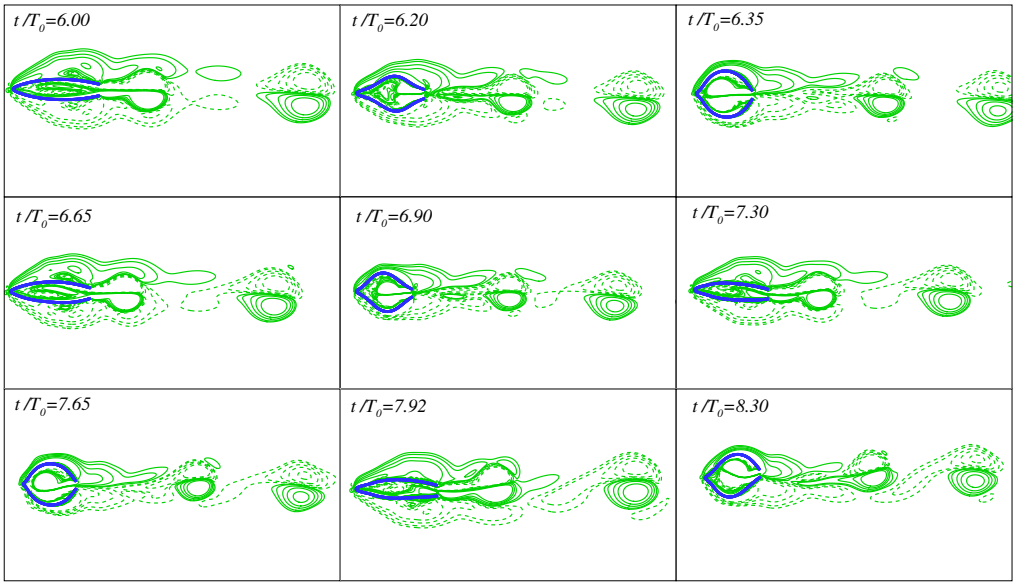

Figure 2.17: The growth of the symmetry-breaking instability. $D = 0.06L$, $K = 6.0\rho u_0^2$.

stored in the springs can not be fully released. A possible solution is to add a resting period after a few inflation-deflation cycles so that the system can be restarted. This, of course, will reduce the average speed of the swimmer.

Finite-core vortex model

The underlying physical mechanism of the symmetry-breaking instability is associated with nonlinear interactions among the vortex pairs in the wake, which essentially form a multiple-body problem. For further insight we consider a simple system of an array of identical vortex pairs consisting of clockwise vortices Γ and counter-clockwise vortices $-\Gamma$, forming a thrust-type wake as shown in Fig. 2.18a. These vortex pairs are artificially added to the flow field at a period of T. In an incoming uniform flow field (with speed u_0 in the x direction), the two points of vortex generation (shown as bullets in the figure) lie at $(0, D/2)$ and $(0, -D/2)$, similar to the upper and lower edges of the exit.

By using the finite-core vortex model [42], the induced angular velocity of each vortex is

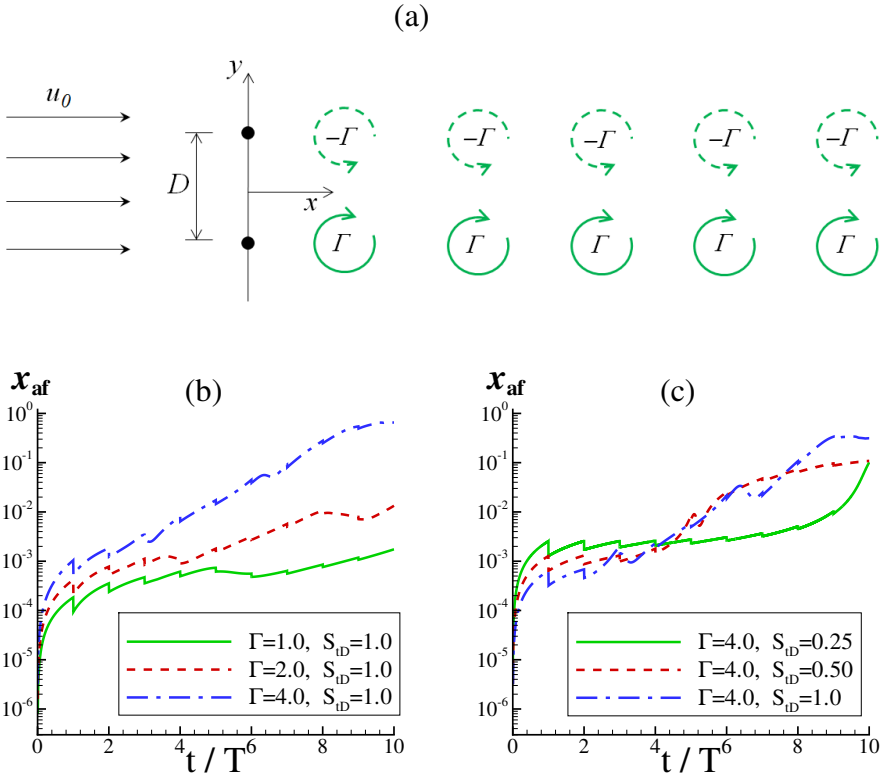

Figure 2.18: (a) Definition of the system with periodically generated vortex pairs forming a thrust-type wake. (b) Growth of the asymmetric parameter x_{af} at three different values of vortex strength Γ with S_{tD} fixed. (c) Growth of the asymmetry factor x_{af} at three different values of S_{tD} with vortex strength Γ fixed.

$\frac{\Gamma}{2\pi r}\exp\{-(r/r_0)^2\}$, where r is the distance measured from the center of the vortex, and r_0 is the size of the core. For illustration, we assume that $u_0 = 1$ and $r_0 = 0.1$. The distance between the centers of the vortices in each pair, D, is chosen to be 1.

An initial disturbance in the form of a 0.1% increase in strength in one of the vortices within the first pair introduced to the flow field is applied. The motion of the vortices is then calculated numerically through an Euler integration algorithm. To monitor the growth of asymmetry in the wake, we define an asymmetry factor x_{af} so that $x_{af} \equiv \sum_1^n \left[|x_i - x_i'| + |y_i + y_i'|\right]/n$, where x_i (y_i) and x_i' (y_i') are the x (or y) locations of the clockwise and counter-clockwise vortices within the $i-$th vortex pair, respectively. n is the total number of vortex pairs in the field, which grows with

time.

As shown in Figs. 2.18b and c, in every case we simulate the instability grows with time and the wake eventually becomes asymmetric with respect to the x axis. The growth rate of the symmetry-breaking instability depends on the vortex strength Γ and the shedding frequency $f \equiv 1/T$ (or, alternatively, the Strouhal number $S_{tD} \equiv fD/u_0$). In general, larger values of Γ contribute to faster growth of x_{af}, indicating that wake with stronger vortices is easier to go unstable. The effect of frequency f is more complicated. On the one hand, higher shedding frequency is associated with more densely packed vortex pairs so that the inter-pair hydrodynamic interaction is more pronounced, which encourages instability growth. On the other hand, in lower frequencies it takes longer time to have the same number of vortices in the field (note that in Figs. 2.18b and c the horizontal aces are t/T, corresponding to the number of vortex pairs in the wake). Therefore in these cases there is longer time for the instability to grow. Indeed, in all the three frequencies we show in Fig. 2.18c, the asymmetry parameter reaches the same level after 10 periods.

In the curves shown in Figs. 2.18b and c, the sawtooth pattern is caused by the periodic introduction of fresh vortex pairs into the wake, which are perfectly symmetric at the moment they appear. With this model it is also easy to show that although the instability itself does not depend on the exact form of disturbance, its detailed growth is affected by when, where, and how strong the asymmetric disturbances are introduced (in our direct numerical simulations the source of disturbance is numerical error).

Further discussion

When fluid viscosity is taken into account, the vortices weaken as they travel downstream due to the dissipation effect. Accordingly it takes longer time for the symmetry-breaking instability to grow. It is also more difficult for instabilities in the wake to prorogate upstream and affect the structural deformation. Thus it is expected that as lower Reynolds numbers this symmetry-breaking

instability is less pronounced. This is consistent with results from our direct numerical simulations.

A similar phenomenon was reported by [43] in a simulation of jellyfish swimming using an immersed-boundary method. It was observed that the wake becomes asymmetric when the Reynolds number surpassed 500. In our system, the instability may be more pronounced since the instability in the wake induces asymmetric responses from the structure and the activation system so that there exists a positive feedback effect.

Most of the simulations in jellyfish swimming, on the other hand, do not show instability in the wake. This may be attributed to the following reasons: a) As illustrated by our simple model, the growth rate of this kind of instability depends on the strength of vortices. The wake created by a jellyfish is usually much weaker than that behind a squid or a squid-like swimmer. b) Many of these studies are focused on relatively low Reynolds numbers, where it takes extremely long time for the instability to grow. To date it is not known if similar instabilities exist in three-dimensional cases with multiple vortex rings in the wake. To answer this question it requires fully three-dimensional studies (rather than axisymmetric models) to examine the interactions between vortex rings in an array.

2.6 Untethered Swimming Mode

To proceed, we consider the dynamics of the aforementioned two-dimensional squid-like swimmer in free-swimming mode. Our focus is on the swimming performance of this system with different design parameters (*e.g.* the frequency of body deformation and the size of the inlet/exit). The near-body flow field and vorticity control mechanisms will also be examined. The swimming performance is measured by the average forward speed per deformation cycle $\overline{V}_x$, travelling distance L_d and cost of transport, which is $CoT = \Delta PE/L_d$.

2.6.1 Measurement of velocity

Through the aforementioned deflation-inflation cycles, the system is able to undergo long-distance swimming, which requires a large computational domain, and subsequently, significant computational effort. To overcome this issue, an uniform background flow with velocity u_0 in the opposite direction of swimming is employed to keep the swimmer from escaping out of a relatively small computational domain during the simulation. Towards this end, the ideal choice of u_0 should be close to the average speed of the swimmer. In practice, for each case a series of testing simulations are required to determine the appropriate value of u_0. The total speed of the swimmer in quiescent water equals u_0 plus the corresponding velocity measured in the imposed stream. Numerically, u_0 is imposed by using a Dirichlet boundary condition at the inflow boundary. The velocity is measured at the center of mass of the internal volume denoted by V_x whose peak value V_{xm} is used to define Reynolds number,

$$Re_m = \frac{\rho V_{xm} L}{\mu}. \tag{2.44}$$

2.6.2 Normalization

u_0 is inappropriate to be the reference velocity since it varies in various simulations. Instead, we then choose $V_0 = \frac{\mu}{\rho L}$ as the characteristic velocity. The characteristic density, length, and time are respectively ρ, L, and $T_0 = \rho L^2/\mu$. All results in this section will be presented in normalized form using these reference variables. Note that since dynamic viscosity μ is involved in the reference framework, most dimensionless quantities will be in large scale.

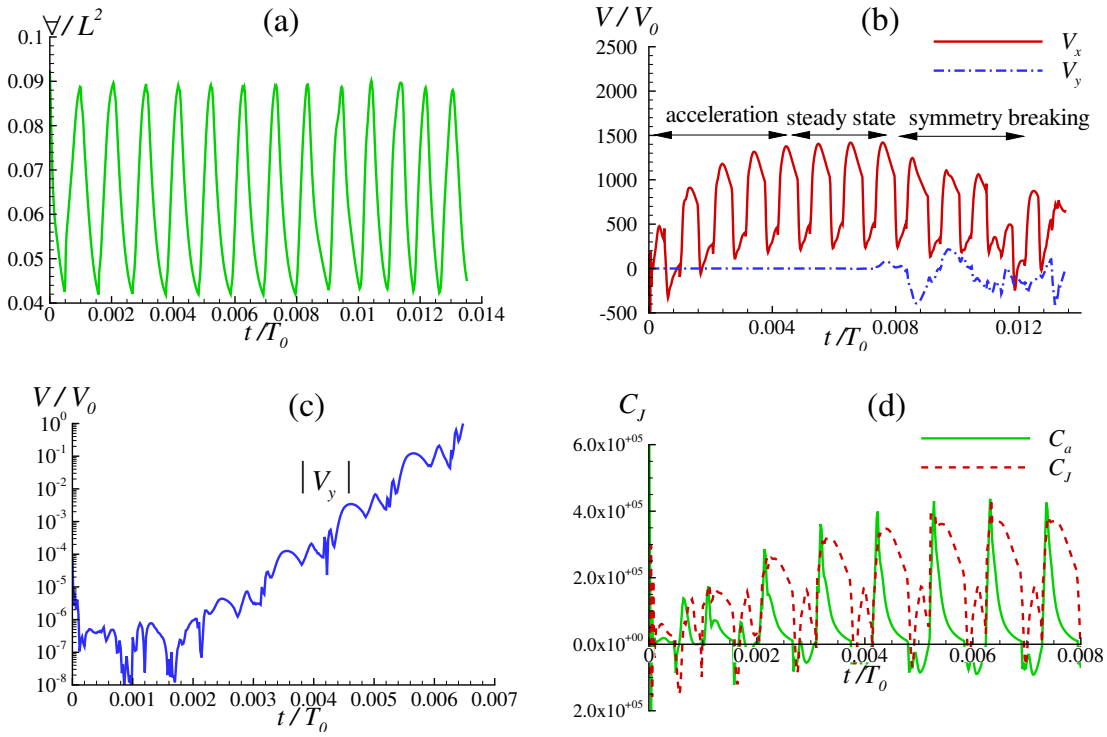

Figure 2.19: Time histories of (a) the inside area of the body $\forall$; (b) instantaneous forward velocity V_x and transverse velocity V_y; (c) logarithmic scale of V_y before $t = 0.07T_0$; and (d) added mass thrust contribution and the jet-related thrust. $K = 2 \times 10^6 \rho V_0^2, D = 0.08L$.

2.6.3 Time histories during the free locomotion

In order to illustrate the locomotion characteristics of the swimmer in long-distance free swimming, in Fig. 2.19 we plot simulation results in the case of $K = 2 \times 10^6 \rho V_0^2, D = 0.08L$, where the background flow speed u_0 is set to be $700V_0$. Following the activation strategy in §2.2, the system undergoes cyclic deformations between deflated and inflated states, leading to periodic variations of the internal area of the swimmer with frequency f (Fig. 2.19a). As displayed in Fig. 2.19b, in this particular case the swimmer experiences a 4-cycle accelerating process before reaching a steady state, whose maximum velocity is around $1400V_0$. Meanwhile a symmetry-breaking instability originates from the wake of vortex pairs comes into play, which grows over time and eventually makes it difficult for the system to maintain straight line swimming, as shown in Fig. 2.19b after two cycles of steady-state swimming. The time evolution of this instability is clearly shown in Fig. 2.19c, where the time history of V_y (the speed of the system in the lateral direction) is plotted in logarithmic scale. Aside from pronounced lateral motion, this instability also considerably diminishes the forward speed (Fig. 2.19b).

In the free-swimming case it is difficult to separate the thrust from the viscous drag. Instead, we use an indirect method to estimate the thrust force F_J produced by the jet. It is known that in free swimming F_J is balanced by 1) the viscous drag and 2) the inertia effect associated with acceleration of the body m_l and its added mass m_a. We approximate the viscous drag by $\frac{1}{2}\rho V_x^2 C_D D_p$, in which C_D is the drag coefficient of the elliptical body with minor axis D_p. For simplicity we choose C_D to be the drag coefficient of an ellipse with eccentricity $e_0 = 0$ (the fully inflated shape) at the instantaneous Reynolds number [44]. The second part (the inertia force) is calculated as $(m_l + m_a)\dot{V}_x$, where the added mass m_a is expressed by $\rho\pi b^2$, in which b denotes the semi-minor axis of ellipse. Figure 2.19d presents the time history of thrust coefficient $C_J = F_J/\rho V_0^2 L$. Meanwhile the added-mass-related thrust coefficient $C_a = F_a/\rho V_0^2 L$, in which $F_a = -V_x \dot{m}_a$ is also displayed in the same figure. Even though C_a is negative during the inflation

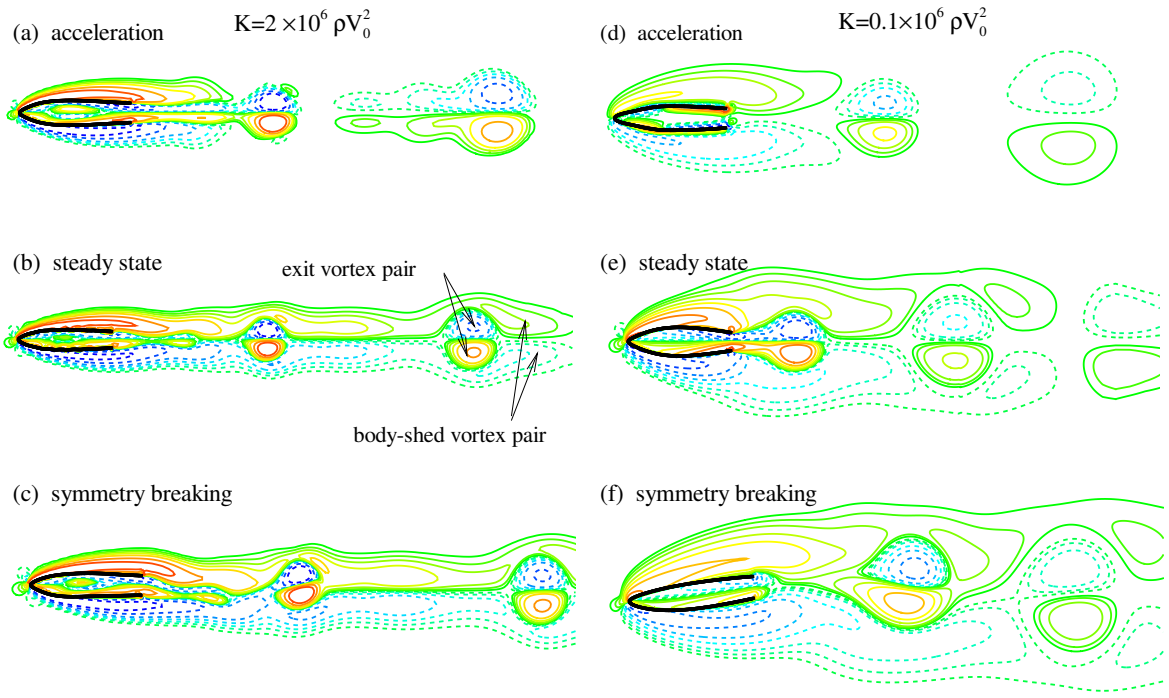

Figure 2.20: Evolution of near-body vorticity contour at $K = 2 \times 10^6 \rho V_0^2$ (a-c) and $K = 1 \times 10^5 \rho V_0^2$ (d-f). $D = 0.08L$.

phase since $\dot{m}_a > 0$, its time-averaged value is still positive since the swimming velocity in deflation is larger than that in inflation. In addition, the magnitude of C_a is comparable to that of the jet-related thrust C_J. This conclusion is different from the one we reached in simulations of a tethered swimmer . The discrepancy is caused by the fact that in the tethered swimmer the forward speed (in that case the speed of the incoming flow) is a constant. In that scenario the positive contribution to thrust generation from added mass during the deflation phase is cancelled by the negative contribution during the inflation phase.

According to simulations of tethered motion of the system, there exist three distinctive types of wake pattern. With constant forward speed that is prescribed, at low pulsating frequencies (corresponding to soft springs) the wake is dominated by body-shed vortices. In these cases the weak jetting fails to overcome viscous drag so that the overall thrust is negative. At relatively high frequencies, however, the exit vortices become sufficiently strong to dominate the vorticity field.

The third pattern is a transit pattern between those two scenarios, *i.e.* vortex pairs from the two origins coexist in the wake.

Unlike the tethered cases, in free-swimming cases the wake signature is found to be dependant upon the stage of motion. For example, Fig. 2.20 displays the wake signatures in two cases, $K = 2 \times 10^6 \rho V_0^2$ and $K = 0.1 \times 10^6 \rho V_0^2$ (in both cases $D = 0.08L$). The Reynolds numbers Re_m for these two case are 1400 and 280, respectively. It is seen that despite the large difference in spring stiffness K (and, subsequently, the frequency of body pulsation), the evolutions of wake in these two cases are similar to each other. During the acceleration stage, the thrust produced by the swimmer (which is associated with the jet-generated wake) is larger than the drag (which is associated with the body-generated wake). For that reason at this stage the wake appears to be dominated by exit vortex pairs (see Figs. 2.20a and d).

As the body is accelerated, the drag effect is getting more pronounced (the drag the body sustains is proportional to the square of speed) until the steady state is reached, in which a balance between time-averaged drag and thrust is achieved. As demonstrated in Figs. 2.20b and e, at this stage the two types of vortices (exit vortices and body-shed ones) are comparable in strength and coexist behind the body. Finally, the asymmetrical vorticity distribution caused by the aforementioned instability is displayed (Figs. 2.20c and f). As a result, lateral force will be induced which deviates the body from its track.

2.6.4 Parametric study

In long-distance swimming the propulsive performance is measured by the average velocity $\overline{V}_x$ as well as the travelling distance L_d and cost of transport CoT over one cycle after the steady state is established. Systematic simulations have been conducted to study the parametric effect. As shown in Fig. 2.21, stiffening the springs tends to increase the deformation frequency f, although its growth rate decreases with K. Higher values of frequency f is associated with larger mean

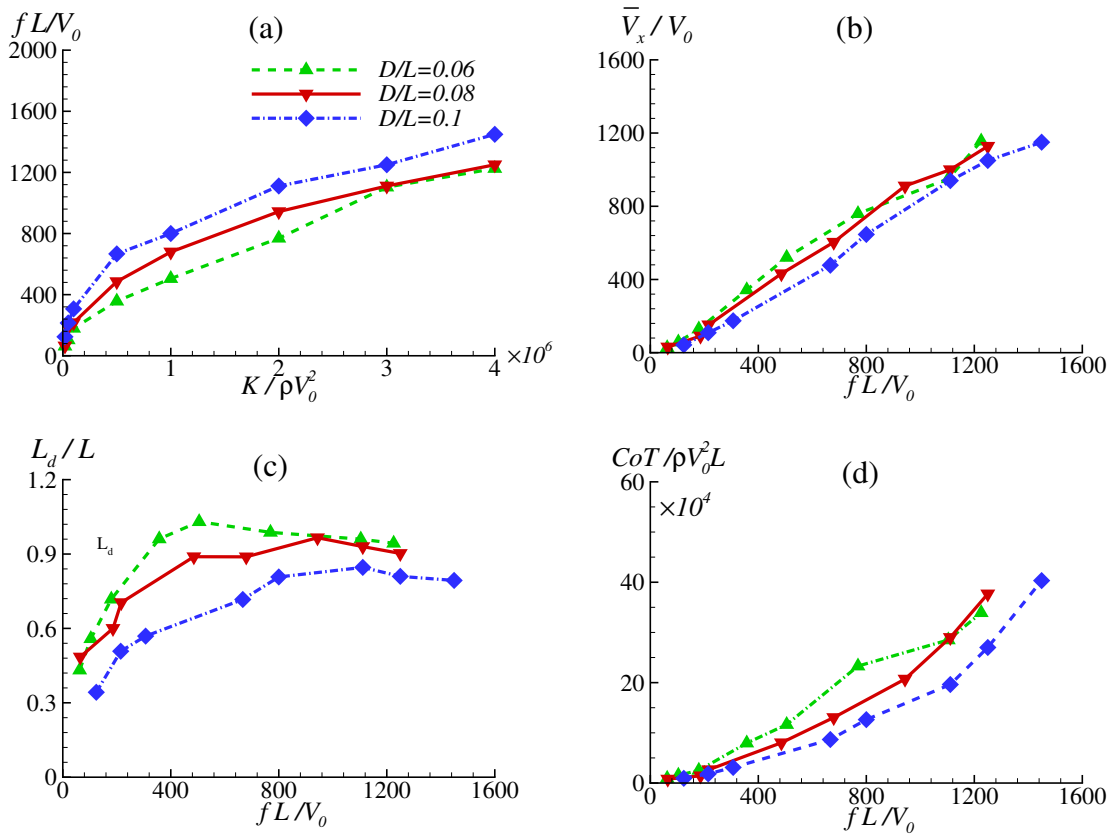

Figure 2.21: (a) Deformation frequency f against K, (b) average speed per cycle $\overline{V}_x$, (c) travelling distance L_d, and (d) CoT as functions of f.

velocity yet lower efficiency (CoT rises steeply with f). The swimming distance $L_d = \overline{V}_x \times T$ grows with f until reaching a peak, after which it will decline slowly due to the fact that the growth of $\overline{V}_x$ fails to compensate the diminish of the time period $T \equiv 1/f$. The maximum value of L_d the is achieved at $f = 600V_0/L$,$900V_0/L$ and $1100V_0/L$ for $D = 0.06L$, $0.08L$ and $0.1L$, respectively.

2.7 Summary and remarks

Inspired by the locomotion mechanism of squids and other cephalopods, we propose a novel underwater propulsion system using pulsed jet enabled by repeated body inflation and deflation deformations. The specific design includes a flexible body with a pressure chamber and an opening

at the rear end, which functions as both the inlet to let water in during the inflation phase and the exit to create the jet during the deflation phase.

To understand the fluid-structure interaction mechanisms involved in the propulsive performance of such a design, a two-dimensional model consisting of a deformable body (depicted as a beam with fixed length) and a number of internal springs is created. The inflation and deflation deformations of the body are achieved through a simple activation strategy using variations in the unstretched lengths of the springs. An immersed-boundary algorithm is employed to solve the fluid-structure interaction problem.

First we concentrate on the tethered swimming performance of this system. The tethered swimming configuration allows us to use the traditional definition of propulsion efficiency, so that our results can be put in context in a broad field of oscillatory propulsive devices such as flapping fins (most of the existing studies in that field use tethered motion as well). In addition, the device we study can not only be used as a stand-alone swimmer, but also be used as a propeller of an underwater vehicle. In the latter case the forward speed is determined by the whole system so that as far as the propeller is concerned the forward motion is similar to a prescribed motion.

Our numerical simulations show that the activation strategy we use is capable of achieving periodic body inflation and deflation. The frequency of oscillation is determined mostly by the stiffness of the springs. The mean thrust generation is found to increase monotonously with increasing frequency, whereas the propulsive efficiency reaches a peak at an optimal frequency before it decays.

The flow field around the system has also been illustrated. In each cycle of oscillation two pairs of vortices are generated and shed into the wake. During the inflation phase a pair of vortices is formed on the outer surface of the body. Another pair is created at the exit during the deflation phase, accompanying the jet formation behind the body. Depending on the frequency of oscillation, there are three distinctive wake patterns, the one dominated by the body-shed vortices,

the one in which the body-shed vortices and the exit vortices are comparable in strength, and the one dominated by the exit vortices. The simulations also suggest that the peak propulsive efficiency is usually reached between the second and the third wake patterns (*i.e.* when the exit vortices start to dominate the wake).

Our long-term simulation shows that due to a symmetry-breaking instability in the wake the steady-state response can only be sustained for a limited number of inflation-deflation cycles before the flow field and the body deformation become asymmetric in the lateral direction. This effect compromises the propulsive performance by reducing the thrust force and inducing a lateral force as well. Moreover, the instability diminishes the controllability of the system so that it is often impossible to continue with the inflation-deflation cycles. A straightforward solution of this problem is to stop the body deformation when the instability occurs and then restart it when the disturbances in the wake are dissipated away. This strategy reduces the average speed the swimmer can reach. The detailed implementation of this working-resting strategy is highly case dependent. Firstly, when the resting period is needed depends on how many inflation-deflation cycles the system can go without being significantly disturbed by the instability. Secondly, the duration of the resting period is determined by how fast the previously shed vortices decay or propagate into the far field, which depends on many factors such as the Reynolds number. It might also be possible to mitigate the effect of this instability through active or passive flow control techniques (*e.g.* active control of body deformation and direction of the exit *via* thrust vectoring). These methods will be explored in future studies.

Second we investigate the dynamics of the propulsive system in free swimming mode. Our results show that in long-distance swimming with multiple inflation-deflation cycles, the swimmer undergoes three different phases, acceleration, steady state and symmetry breaking, each with its own distinctive wake signature. The acceleration stage is associated with wakes dominated by vortices shed from the exit. When steady-state swimming is reached, this pattern is replaced

by a transit wake, in which the strengthes of the exit-generated vortices and the body-shed ones are comparable. Finally, when the symmetry-breaking instability dominates the wake becomes asymmetrical and the swimmer deviates from its track. The increase of the deflation-inflation frequency enhances the swimming speed at the expense of lower efficiency.

Finally, our current design focuses on a two-dimensional system which bears certain resemblance of the jetting mechanism of squids. Nevertheless to closely imitate the dynamics of squid swimming an three dimensional or axisymmetric design may be a better option (although it will still not be representative of real squids, which are not axisymmetric). With a circular exit there will be vortex rings in the wake, which are associated with physical mechanisms somewhat different from the vortex pairs examined in the current work. Moreover, it will be interesting to study if the interaction among these rings may also lead to symmetry-breaking instabilities.

This chapter, in part, is a reprint of the material as it appears in the following papers.

- Xiaobo Bi and Qiang Zhu, "Fluid-structure Interaction of a Squid-inspired Swimmer", *Physics of Fluids*, vol. 31, pp. 101901, 2019.

- Xiaobo Bi and Qiang Zhu, "Dynamics of a Squid-Inspired Swimmer in Free Swimming", *Bioinspiration & Biomimetics*, vol. 15, no. 1, pp. 016005, December 2019.

The dissertation author is the primary investigator and author of these papers.

Chapter 3

Fluid Dynamics of an Axisymmetric Jet Propulsion System via Body Deformation

In this chapter we develop an axisymmetric fluid dynamics model that consists of a deformable body with a pressure chamber similar to the one possessed by a squid in jetting mode and a orifice exit through which fluid is sucked or ejected, imitating the funnel tube of squids. Through this simplified axisymmetric swimmer, we aim at exploring the jetting dynamics of squid-inspired propulsion, especially the effect of jet speed, jet acceleration, the vortex ring formation etc. on the performance of the swimmer.

3.1 Problem statement

Similar to the two dimensional model in the previous chapter, the axisymmetric propulsion system contains a deformable body and an orifice (see Fig. 3.1a). The body is idealized as an ellipsoidal shell of zero thickness with a circular exit whose diameter is D, which is set to be $0.1L$ (L is the contour length of the body). The axisymmetric numerical model used in this study is presented in Fig. 3.1b. The propulsion process includes two phases, deflation and inflation, both

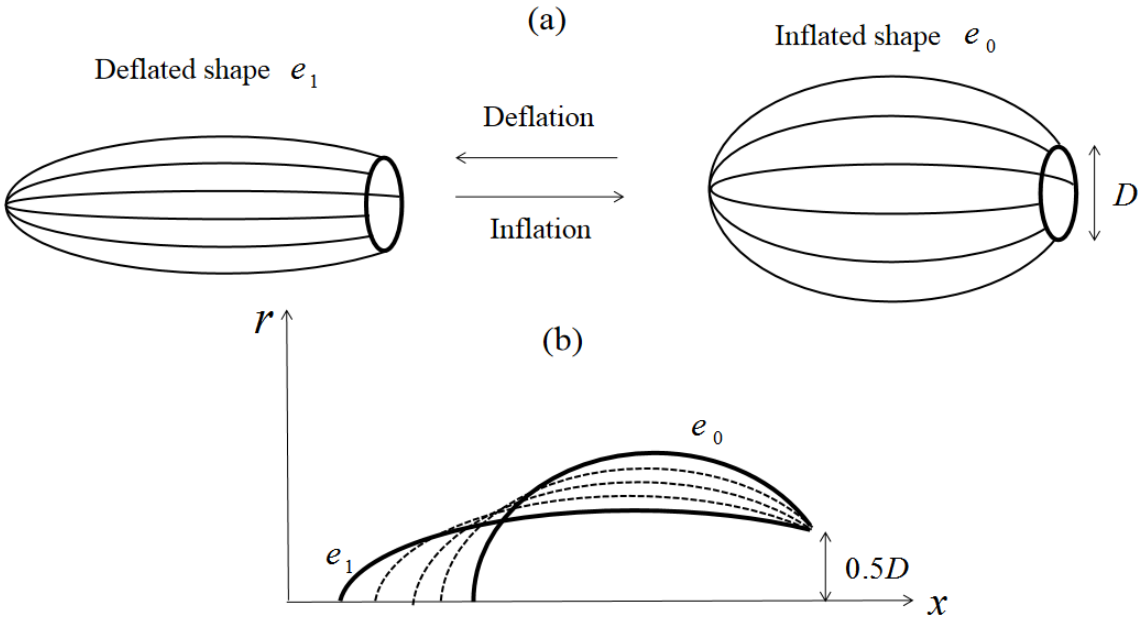

Figure 3.1: (a) Rendition of the axisymmetric squid-inspired system, (b) the simulation model and body deformation.

accomplished by prescribed body shape change. During the body deformation the swimmer is tethered at the orifice plane.

The deformation trajectory is depicted by the time history of the ellipsoidal eccentricity $e(t)$, which in its turn is determined by the jet speed profile $V_j(t)$ we prescribe, where V_j (the spatially averaged axial flow speed at the exit plane) is defined as

$$V_j(t) = \frac{-1}{A}\frac{d\forall}{dt} = \frac{-4}{\pi D^2}\frac{d\forall}{dt}. \tag{3.1}$$

in which $\forall(e)$ is the volume of the internal chamber depending on the eccentricity e, $A = \pi D^2/4$ denotes the area of the exit. Equation (3.1) enables us to determine the time evolution of the internal body volume $\forall$ with the prescribed $V_j(t)$, then map onto $e(t)$, which describes the body deformation trajectory. With L, D and e being known, the geometry of the swimmer can be determined using the algorithm describe in Appendix A.

3.2 Governing equations

The fluid dynamics is governed by the incompressible axisymmetric Navier-Stokes equations. Within the immersed-boundary framework [28–30], an additional forcing term is incorporated into the governing equations to enforces the boundary conditions associated with the solid body and its deformation.

Let $\mathbf{x} \equiv (x, r)$ be a cylindrical frame with x in the direction of the jet and r the radial direction, $\mathbf{u}(\mathbf{x}, t) \equiv (u_x, u_r)$ corresponds to velocity components in each direction, $p(\mathbf{x}, t)$ is the pressure distribution, and $\mathbf{f}(\mathbf{x}, t) \equiv (f_x, f_r)$ stands for the force density exerted by the immersed boundary Γ_{ib} on the surrounding flow. In the immersed-boundary approach the Navier-Stokes equations in the fluid domain Ω_f and the continuity equation are

$$f_x = \rho\frac{\partial u_x}{\partial t} + \rho\mathbf{u}\cdot\nabla u_x + \frac{\partial p}{\partial x} - \mu\left[\frac{\partial^2 u_x}{\partial x^2} + \frac{1}{r}\frac{\partial}{\partial r}(r\frac{\partial u_x}{\partial r})\right] \tag{3.2}$$

$$f_r = \rho\frac{\partial u_r}{\partial t} + \rho\mathbf{u}\cdot\nabla u_r + \frac{\partial p}{\partial r} - \mu\left[\frac{\partial^2 u_r}{\partial x^2} + \frac{1}{r}\frac{\partial}{\partial r}(r\frac{\partial u_r}{\partial r}) - \frac{u_r}{r^2}\right] \tag{3.3}$$

$$0 = \frac{\partial u_x}{\partial x} + \frac{1}{r}\frac{\partial(r u_r)}{\partial r}, \tag{3.4}$$

where ρ represents the fluid density and μ stands for the dynamic viscosity. The corresponding boundary conditions are

- Inflow: $u_x = u_0$, $u_r = 0$, $\frac{\partial p}{\partial x} = 0$;
- Outflow: $\frac{\partial(u_x,u_r)}{\partial t} + u_0\frac{\partial(u_x,u_r)}{\partial x} = 0$, $\frac{\partial p}{\partial x} = 0$;
- Rotating axis: $\frac{\partial u_x}{\partial r} = 0$, $u_r = 0$, $\frac{\partial p}{\partial r} = 0$;
- Far field: $u_x = u_0$, $u_r = 0$, $\frac{\partial p}{\partial r} = 0$.

where $\mathbf{n}$ is the outward normal unit vector of the domain boundaries.

In this axisymmetric numerical model, the body kinematics are described in the same way as the two dimensional problem in chapter 2. The feedback algorithm (see Eqns (2.8)- (2.11))will also be incorporated to treat the fluid-structure coupling in the axisymmetric case.

Integrating the distributed interaction force $\mathbf{F}(s,t)$ in the $-x$ direction along the body Γ_{ib}, we have the net axial hydrodynamic force acting on the body, which is given as

$$F_n = -\int_{\Gamma_{ib}} 2\pi r(s) F_x(s,t) ds. \tag{3.5}$$

3.3 Numerical algorithm

The governing equations (Eqns.(3.2)-(3.4)) are solved to update the fluid velocity, pressure and interacting force at $(n+1)$th time step using data from its previous time step n. Following Kim *et al.* [35], the fluid-dynamics equations are temporally discretized with the Crank-Nicholson scheme and spatially discretized using the finite difference method within a rectangular domain filled with staggered grid (see Fig. 2.3). The discrete governing equations are presented as

$$\begin{aligned}
\rho\frac{u_x^{n+1}-u_x^n}{\Delta t} + \rho\frac{\mathcal{H}(u_x^{n+1})+\mathcal{H}(u_x^n)}{2} &= -\mathcal{G}_x(p^{n+1/2}) + \mu\frac{\mathcal{L}_x(u_x^{n+1})+\mathcal{L}_x(u_x^n)}{2} + f_x^n, \\
\rho\frac{u_r^{n+1}-u_r^n}{\Delta t} + \rho\frac{\mathcal{H}(u_r^{n+1})+\mathcal{H}(u_r^n)}{2} &= -\mathcal{G}_r(p^{n+1/2}) + \mu\frac{\mathcal{L}_r(u_r^{n+1})+\mathcal{L}_r(u_r^n)}{2} + f_r^n, \\
\mathcal{D}_x\left(u_x^{n+1}\right) + \mathcal{D}_r\left(u_r^{n+1}\right) &= 0,
\end{aligned} \tag{3.6}$$

where the operators are defined as

$$\begin{aligned}
\mathcal{G}_x = \mathcal{D}_x = \frac{\partial}{\partial x}, \qquad \mathcal{G}_r = \frac{\partial}{\partial r}, \qquad \mathcal{D}_r = \frac{1}{r}\frac{\partial}{\partial r}r, \qquad \mathcal{H} = u_x\frac{\partial}{\partial x} + u_r\frac{\partial}{\partial r}, \\
\mathcal{L}_x = \frac{\partial^2}{\partial x^2} + \frac{1}{r}\frac{\partial}{\partial r}r\frac{\partial}{\partial r}, \qquad \mathcal{L}_r = \frac{\partial^2}{\partial x^2} + \frac{1}{r}\frac{\partial}{\partial r}r\frac{\partial}{\partial r} - \frac{1}{r^2}.
\end{aligned}$$

The presence of convective terms makes the problem nonlinear since the velocities are

unknown, *e.g.* $\mathcal{H}(u_x^{n+1}) = u_x^{n+1}\frac{\partial u_x^{n+1}}{\partial x} + u_r^{n+1}\frac{\partial u_x^{n+1}}{\partial r}$. Hereby we linearize the equations by employing the scheme of Beam & Warming [45] with second-order temporal accuracy.

$$\frac{\mathcal{H}(u_x^{n+1}) + \mathcal{H}(u_x^n)}{2} = \mathcal{N}_{xx}(u_x^{n+1}) + \mathcal{N}_{xr}(u_r^{n+1}), \tag{3.7}$$

$$\frac{\mathcal{H}(u_r^{n+1}) + \mathcal{H}(u_r^n)}{2} = \mathcal{N}_{rx}(u_x^{n+1}) + \mathcal{N}_{rr}(u_r^{n+1}), \tag{3.8}$$

in which the linear convective operators only include the velocity at n time step:

$$\mathcal{N}_{xx} = \frac{\partial}{\partial x}u_x^n + \frac{1}{2r}\frac{\partial}{\partial r}ru_r^n, \qquad \mathcal{N}_{xr} = \frac{1}{2r}\frac{\partial}{\partial r}ru_x^n,$$
$$\mathcal{N}_{rx} = \frac{1}{2}\frac{\partial}{\partial x}u_r^n, \qquad \mathcal{N}_{rr} = \frac{1}{2}\frac{\partial}{\partial x}u_x^n + \frac{1}{r}\frac{\partial}{\partial r}ru_r^n$$

Assuming $\delta u_x^{n+1} = u_x^{n+1} - u_x^n, \delta u_r^{n+1} = u_r^{n+1} - u_r^n, \delta p = p^{n+1/2} - p^{n-1/2}$, we then rewrite the discretized and linearized equations in matrix form as

$$\begin{bmatrix} A_x & \rho\mathcal{N}_{xr} & \mathcal{G}_x \\ \rho\mathcal{N}_{rx} & A_r & \mathcal{G}_r \\ \mathcal{D}_x & \mathcal{D}_r & 0 \end{bmatrix} \begin{bmatrix} \delta u_x^{n+1} \\ \delta u_r^{n+1} \\ \delta p \end{bmatrix} = \begin{bmatrix} R_x \\ R_r \\ 0 \end{bmatrix}, \tag{3.9}$$

where

$$A_x = \tfrac{1}{\Delta t}\left[\rho\boldsymbol{I} + \Delta t\left(\rho\mathcal{N}_{xx} - \tfrac{\mu}{2}\mathcal{L}_x\right)\right],$$
$$A_r = \tfrac{1}{\Delta t}\left[\rho\boldsymbol{I} + \Delta t\left(\rho\mathcal{N}_{rr} - \tfrac{\mu}{2}\mathcal{L}_r\right)\right],$$
$$R_x = \mu\mathcal{L}_x(u_x^n) + f_x^n - \rho\mathcal{N}_{xx}(u_x^n) - \rho\mathcal{N}_{xr}(u_r^n) - \mathcal{G}_x(p^{n-1/2}),$$
$$R_r = \mu\mathcal{L}_r(u_r^n) + f_r^n - \rho\mathcal{N}_{rx}(u_x^n) - \rho\mathcal{N}_{rr}(u_r^n) - \mathcal{G}_r(p^{n-1/2}).$$

To solve Eqn. (3.9), inversion of the large sparse coefficient matrix is needed, which

requires significant CPU time and memory. Instead, we use LU decomposition to factorize the coefficient matrix so that velocity and pressure are decoupled, yielding

$$\begin{bmatrix} A_x & 0 & 0 \\ \rho\mathcal{N}_{rx} & A_r & 0 \\ \mathcal{D}_x & \mathcal{D}_r & \frac{-\Delta t(\mathcal{D}_x\mathcal{G}_x+\mathcal{D}_r\mathcal{G}_r)}{\rho} \end{bmatrix} \begin{bmatrix} I & \Delta t\mathcal{N}_{xr} & \frac{\Delta t\mathcal{G}_x}{\rho} \\ 0 & I & \frac{\Delta t\mathcal{G}_r}{\rho} \\ 0 & 0 & I \end{bmatrix} \begin{bmatrix} \delta u_x^{n+1} \\ \delta u_r^{n+1} \\ \delta p \end{bmatrix} = \begin{bmatrix} R_x \\ R_r \\ 0 \end{bmatrix} + err(\Delta t^2), \tag{3.10}$$

where the second-order residual error term is

$$err = \Delta t \begin{bmatrix} \left(\rho\mathcal{N}_{xx} - \frac{\mu}{2}\mathcal{L}_x\right)\mathcal{N}_{xr}(\delta u_r^{n+1}) + \left(\mathcal{N}_{xx} - \frac{\mu}{2\rho}\mathcal{L}_x\right)\mathcal{G}_x(\delta p) \\ \rho\mathcal{N}_{xr}\mathcal{N}_{rx}(\delta u_r^{n+1}) + \left(\mathcal{N}_{rr} - \frac{\mu}{2\rho}\mathcal{L}_r\right)\mathcal{G}_r(\delta p) + \mathcal{N}_{rx}\mathcal{G}_x(\delta p) \\ \mathcal{D}_x\mathcal{N}_{xr}(\delta u_r^{n+1}) \end{bmatrix}.$$

Note that since δu_x^{n+1}, δu_r^{n+1} and δp are $O(\Delta t)$, the residual error term is $O(\Delta t^2)$, making the above approximation second order in time.

Let δu_x^* and δu_r^* be the intermediate values of the velocity increments at $(n+1)$th time step, Eqn. (3.10) can be rewritten as

$$\begin{bmatrix} A_x & 0 & 0 \\ \rho\mathcal{N}_{rx} & A_r & 0 \\ \mathcal{D}_x & \mathcal{D}_r & \frac{-\Delta t(\mathcal{D}_x\mathcal{G}_x+\mathcal{D}_r\mathcal{G}_r)}{\rho} \end{bmatrix} \begin{bmatrix} \delta u_x^* \\ \delta u_r^* \\ \delta p \end{bmatrix} = \begin{bmatrix} R_x \\ R_r \\ 0 \end{bmatrix}, \tag{3.11}$$

and

$$\begin{bmatrix} I & \Delta t\mathcal{N}_{xr} & \frac{\Delta t\mathcal{G}_x}{\rho} \\ 0 & I & \frac{\Delta t\mathcal{G}_r}{\rho} \\ 0 & 0 & I \end{bmatrix} \begin{bmatrix} \delta u_x^{n+1} \\ \delta u_r^{n+1} \\ \delta p \end{bmatrix} = \begin{bmatrix} \delta u_x^* \\ \delta u_r^* \\ \delta p \end{bmatrix}. \tag{3.12}$$

The following steps are taken to update the flow field:

Step 1: solve the intermediate velocity increments via $A_x \delta u_x^* = R_x$ and $A_r \delta u_r^* = R_r - \rho \mathcal{N}_{rx} \delta u_x^*$;

Step 2: solve δp from the elliptic equation $\Delta t(\mathcal{D}_x \mathcal{G}_x + \mathcal{D}_r \mathcal{G}_r)\delta p = \rho \mathcal{D}_x \delta u_x^* + \rho \mathcal{D}_r \delta u_r^*$;

Step 3: update the velocity increments at $n+1$ time level via $\delta u_r^{n+1} = \delta u_r^* - \Delta t \mathcal{G}_r \delta p/\rho$ and $\delta u_x^{n+1} = \delta u_x^* - \Delta t \mathcal{N}_{xr} \delta u_r^{n+1} - \Delta t \mathcal{G}_x \delta p/\rho$;

Step 4: update the velocities and pressure at time level $n+1$ via $u_x^{n+1} = u_x^n + \delta u_x^{n+1}$, $u_r^{n+1} = u_r^n + \delta u_r^{n+1}$, and $p^{n+1/2} = p^{n-1/2} + \delta p$.

We proceed by rewriting the equation $A_x \delta u_x^* = R_x$ in the first step as,

$$\frac{1}{\Delta t}\left[\rho \boldsymbol{I} + \Delta t M\right] \delta u_x^* = R_x, \tag{3.13}$$

where $M = \left(\rho \mathcal{N}_{xx} - \frac{\mu}{2}\mathcal{L}_x\right)$. we then split the matrix M into two parts, *i.e* M^x and M^r, which only involve the derivative of x and r, respectively. Hence

$$\frac{1}{\Delta t}\left[\boldsymbol{I} + \Delta t(M^x + M^r)\right] \delta u_x^* = R_x. \tag{3.14}$$

The equation can be approximated by

$$\frac{1}{\Delta t}(\boldsymbol{I} + \Delta t M^x)(\boldsymbol{I} + \Delta t M^r)\delta u_x^* = R_x, \tag{3.15}$$

in which the temporal second order accuracy is preserved. The approximation steers away from the inversion of large sparse coefficient matrix A_x. Instead, we only need to handle tridiagonal matrices M^x and M^r. The same treatment can also be applied to the second equation $A_r \delta u_r^* = R_r - \rho \mathcal{N}_{rx} \delta u_x^*$ in the first step.

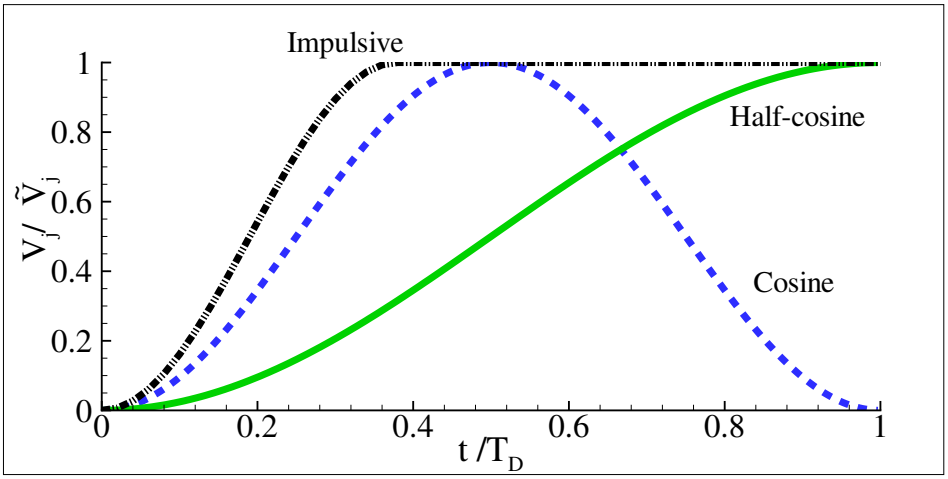

Figure 3.2: Time histories of jet speed of impulsive, cosine and half-cosine profile.

The validity and accuracy of this numerical method is delineated through comparisons with benchmark results of a canonical problem as shown in Appendix C.

3.4 Escaping mode through single deflation stroke

First of all, we consider the escaping locomotion of the swimmer through a pulsed jetting accomplished by body deflation. In this scenario, the simulations are performed in static fluid so that the incoming flow speed u_0 is set to be zero. Three jet velocity profiles, namely impulsive, cosine and half-cosine, are examined. The jet speed V_j are prescribed by following equations

$$\text{Impulsive jet:} \qquad V_j(t) = \begin{cases} 0.5\tilde{V}_j[1 - cos(\frac{\pi t}{o.4T_D})] & \text{if } t \in [0, 0.4T_D] \\ \tilde{V}_j & \text{if } t \in (0.4T_D, T_D] \end{cases} \tag{3.16}$$

$$\text{Cosine jet:} \qquad V_j = 0.5\tilde{V}_j \left[1 - \cos(2\pi t/T_D)\right], \tag{3.17}$$

$$\text{Half-cosine jet:} \qquad V_j = 0.5\tilde{V}_j \left[1 - \cos(\pi t/T_D)\right]. \tag{3.18}$$

where $\tilde{V}_j$ stands for the maximum (or upper-bound) spatially averaged jet speed at the exit plane, T_D is the time duration of the body deflation. Figure 3.2 presents the time histories of jet speed for different jet profiles. A jet-based Reynolds number is defined as

$$Re_j = \frac{\rho \tilde{V}_j D}{\mu}. \tag{3.19}$$

All simulations of this section will be conducted at $Re_j = 150$.

3.4.1 Independence tests

To find proper numerical parameters, a grid independence study has been performed as shown in Fig. 3.3a, where Δx is the size of the fluidic grid in the neighborhood of the body. The effect of time step Δt is also studied (see Fig. 3.3b). These tests show that the results are not sensitive to the grid size and the time step if they are sufficiently small. Hereafter we choose $\Delta r = \Delta x = 0.03D$, $\Delta s = 0.0167D$ and $\Delta t = 5 \times 10^{-4} T_0$, where $T_0 = D/\tilde{V}_j$.

3.4.2 Vortex ring formation and evolution

By using a piston-cylinder apparatus, Gharib *et al.* [46] found that the formation of vortex rings by jet flow was determined by a dimensionless parameter called *formation number*, which was defined as L/D, where L and D are the length and diameter of the jet plug, respectively. The *formation number* coincides with the stroke ratio of the piston. According to their observations, increasing this parameter will enhance the vortex ring until a threshold called critical stroke ratio (*formation number*) is reached. Beyond this threshold, the *Pinch-off* of the vortex ring occurs. Specifically, the fluid discharged thereafter forms minor vortex rings behind the leading ring, rather than being entrained into it, *i.e.* the leading vortex ring reaches saturation state at the critical stroke ratio. Note that the experiment was performed at $Re_j = 2100$.

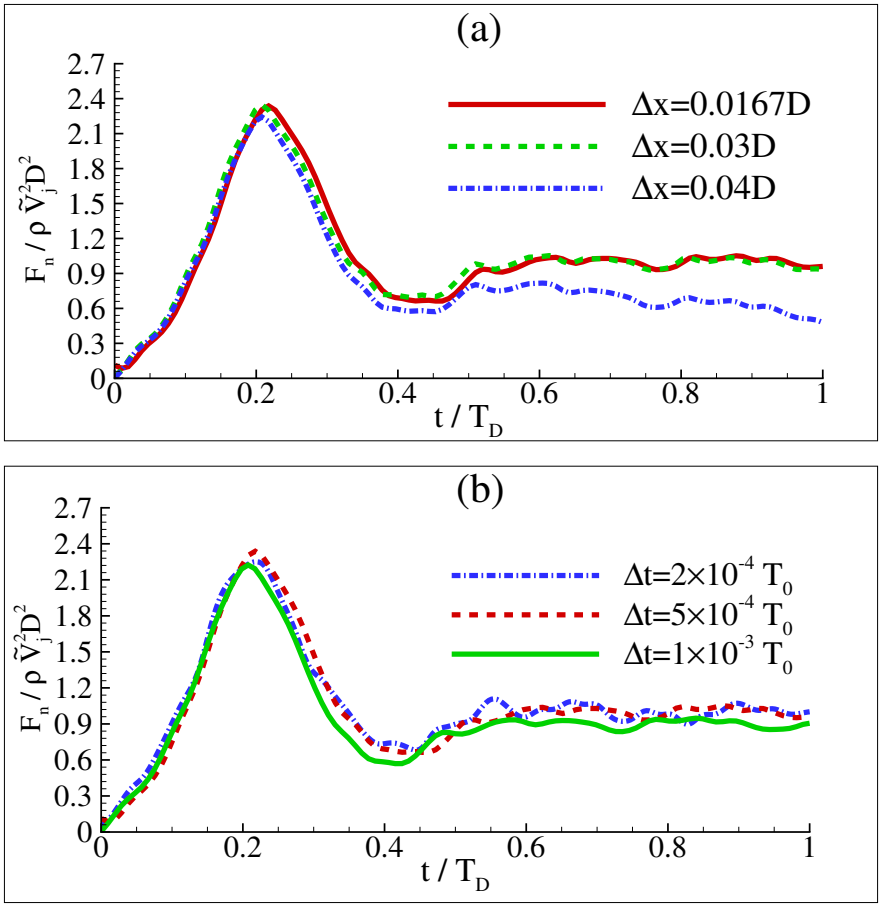

Figure 3.3: (a) Sensitivity tests for fluidic grid size when $\Delta r = \Delta x$ and $\Delta t = 5\times10^{-4}T_0$, where $T_0 = D/\tilde{V}_j$; (b) sensitivity tests for time step when $\Delta x = \Delta r = 0.02D$. The impulsive jet velocity profile (Eq. (3.16)) is used with $\Delta s = 0.0167D$ and $\Gamma_m = 4.6$.

Table 3.1: Maximum formation number Γ_m for various initial states e_0 with the fully deflated state fixed as $e_1 = 0.95$.

e_0	0.92	0.90	0.86	0.80	0.65
Γ_m	2.9	4.6	7.3	10.4	15.0

A theoretical explanation of this phenomenon was provided by Linden and Turner [47]. In that work they compared properties of the jet plug (volume, circulation, impulse, and kinetic energy) with those of a finite-core vortex ring. Their results indicate that the critical formation number corresponds roughly to the limiting case when these properties of the jet plug match those of a single vortex ring, *i.e.* the jet is completely rolled into a vortex ring with maximum strength. They further demonstrated that at this particular case the impulse created by the jet was maximized for given energy input.

Herein, we will explore the effect of the *Pinch-off* phenomenon upon the dynamics of the swimmer. The effective *formation number* associated with the deflation deformation is defined as $\Gamma = 4\Lambda/(\pi D^3)$, where $\Lambda = \forall(e_0) - \forall(e)$ is the fluid volume ejected out of the chamber. The maximum value of Γ, labelled as Γ_m, is reached at the end of body shrinking. Its exact value is $4(\forall(e_0) - \forall(e_1))/(\pi D^3)$. Table 3.1 presents a sequence of cases with different Γ_m that will be examined in this section.

Using the impulsive velocity profiles(see Eqn.(3.16)), we investigate the vortex ring generation process during the deflation deformation. Figures 3.4a and d present the flow field at the end of the deflation for the cases with $\Gamma_m = 2.9$ and $\Gamma_m = 7.3$, respectively. The corresponding flow fields visualized *via* streamlines (Figs. 3.4b and e) and Q criterion (Figs. 3.4c and f) are also displayed. These figures show that in the case of $\Gamma_m = 2.9$ most of the ejected fluid is entrained into a single vortex ring. When Γ_m is 7.3, on the other hand, the wake consists of a leading vortex followed by a trailing flow. The behavior here is somewhat different from previous observations that show additional vortices being formed in the trailing flow [46]. The difference is mostly attributed to

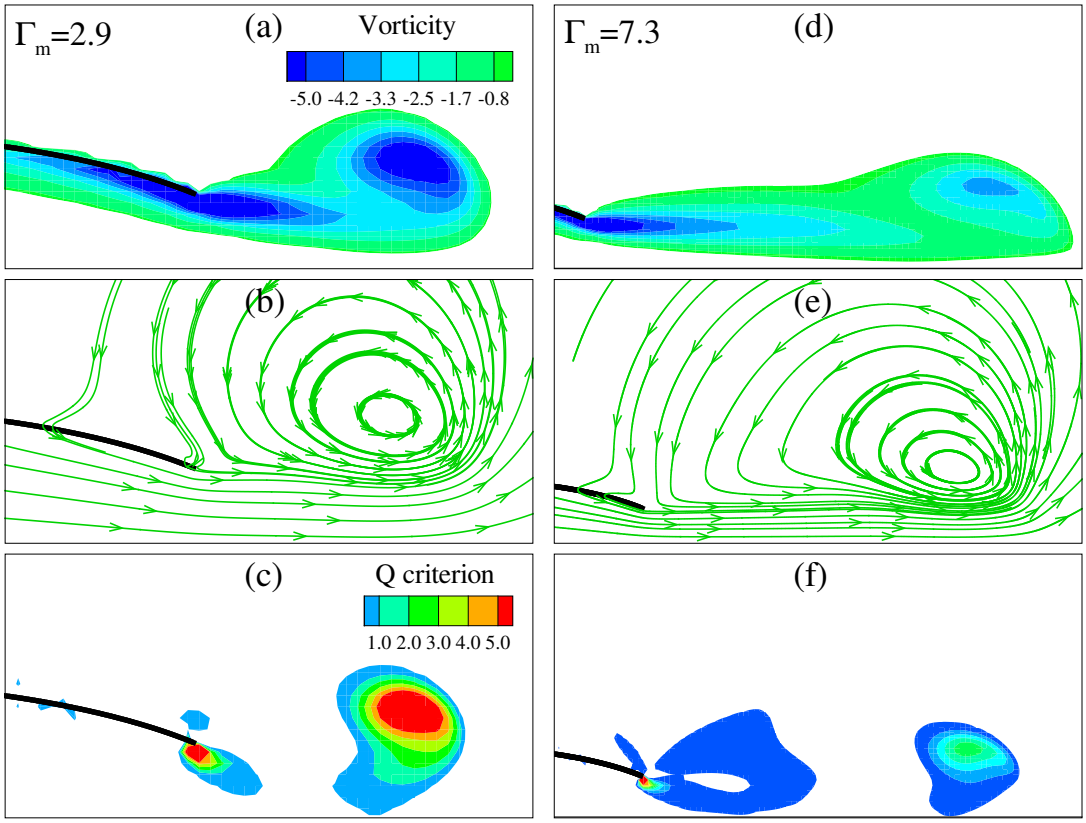

Figure 3.4: Vorticity visualization (a,d), streamline (b,e) and Q criterion distribution (c,f) of the wake at $\Gamma_m = 2.9$ and 7.3. The vorticity is normalized by $\tilde{V}_j/D$. These snapshots are captured at the end of the deflation phase. Impulsive jet profile is applied.

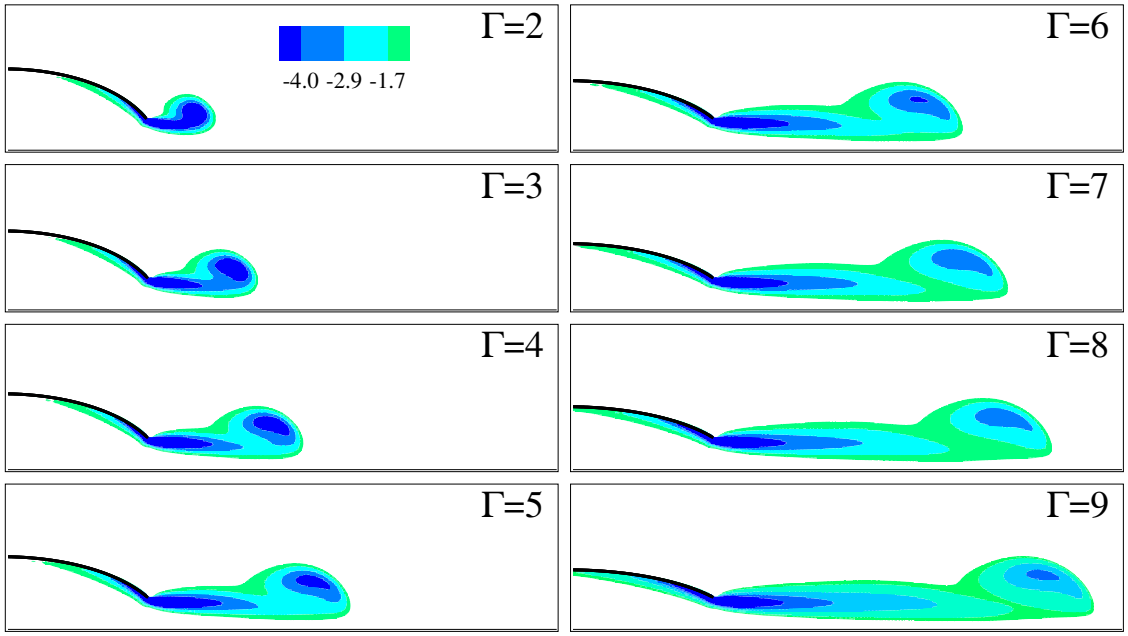

Figure 3.5: Wake evolution at $\Gamma_m = 10.4$ visualized *via* vorticity. Impulsive jet profile is applied.

the Reynolds number effect. Indeed, these results are consistent with experimental data at similar range of Reynolds numbers [2].

For further insight, Fig. 3.5 displays snapshots of the flow field at various time instants throughout the jetting process for the case of $\Gamma_m = 10.4$. It shows that the jet flow continuously feeds the leading vortex ring until around $\Gamma = 4$, when the leading vortex ring detaches from the trailing flow. As mentioned earlier, in this low Reynolds number regime the trailing flow is not sufficiently strong to induce a secondary vortex ring. Instead, it remains connected with the nozzle as well as the leading vortex ring. The consequence is that after $\Gamma = 4$ the trailing flow is still able to feed the leading vortex ring. Although complete disconnection between these two flow structures (the leading vortex ring and its trailing flow) may never occur [48], a clearer separation is observed at $\Gamma = 6 \sim 7$. After that, the strength of the leading ring stops growing and decays slowly due to viscous dissipation. This is clearly shown in Fig. 3.6a, where the circulation of the leading vortex ring C is plotted as a function of Γ.

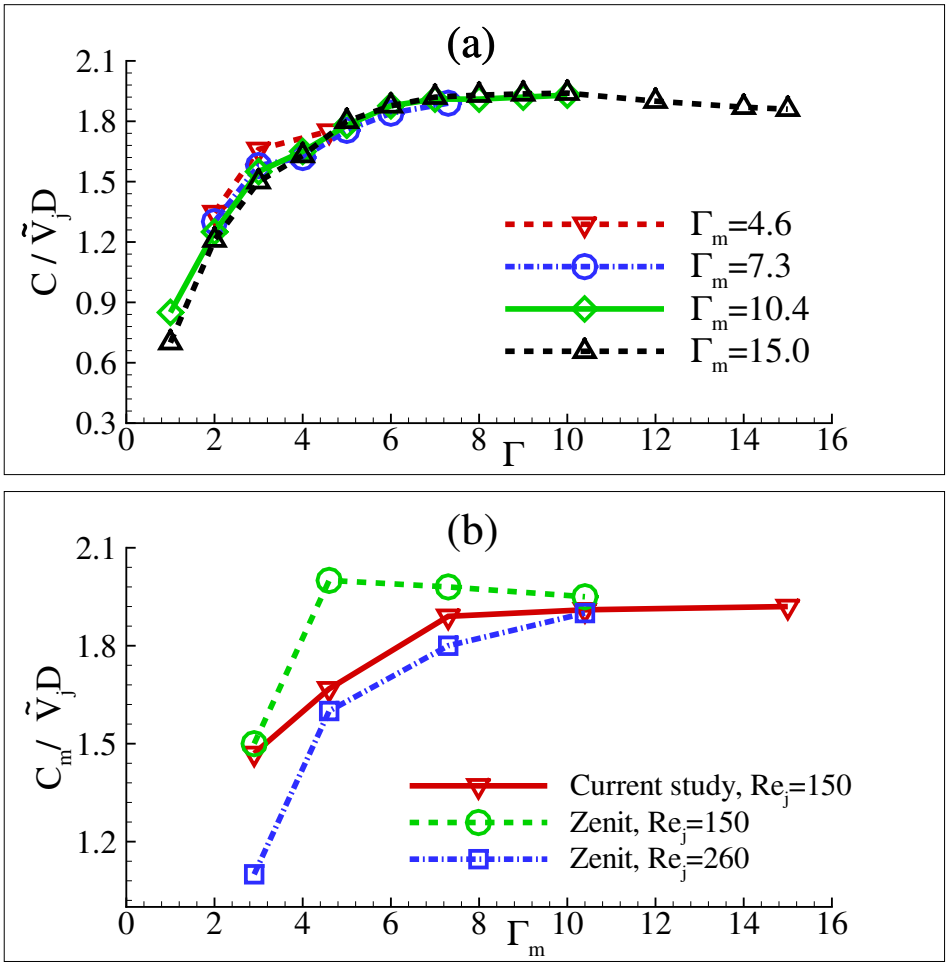

Figure 3.6: (a) Vortex ring circulation C as a function of Γ, (b) peak value of vortex ring circulation C_m as a function of Γ_m. Results from a cylindrical piston experiment by Zenit [2] are presented for comparison.

As displayed in Fig. 3.6a, the normalized circulation of the vortex ring reaches a peak value around 2.0 when $\Gamma = 6 \sim 7$. This implies that after the apparent separation of the vortex ring from the trailing flow, it is still fed by the jet. The supply rate, however, decreases gradually as the ring moves downstream away from the nozzle so that the growth rate of the circulation curve declines prior to the plateau. At $\Gamma = 6 \sim 7$ the supply rate is balanced by the rate of dissipation and the leading ring stops growing. This coincides with a clearer spatial isolation of the leading vortex ring (see Fig. 3.5).

Figure 3.6b displays the peak circulation of leading vortex ring C_m as a function of Γ_m. For comparison, results from a cylindrical piston experiment are plotted in the same figure as well. Even though the maximum value of C_m we obtain is in good agreement with the reported value, there is still certain discrepancy in terms of the critical formation number (stroke ratio). This is likely to be caused by differences in details of the jet profile. First, a constant piston velocity profile without an acceleration phase was applied in the experiment, while our system undergoes an accelerating stage that accounts for about 25% of the whole deformation time. The viscous dissipation is more significant in our model so that higher formation number is needed to attain the saturated state. Second, the difference in nozzle geometry (conical versus tubular) may also cause some difference in vortex ring formation.

Next we examine the two other jet profiles, *i.e.* cosine and half-cosine as described in Eqns. (3.17-3.18). Figure 3.7 presents time histories of the leading vortex ring circulation. For the half-cosine velocity distribution, in which the jet is accelerated throughout the entire deflation process, the circulation of vortex ring keeps growing till the end of jetting because of the continuous vorticity feeding from the jet. Without exception, lower Γ_m yields larger circulation for a fixed Γ since the same amount of fluid mass is ejected with higher speed. For the same reason, the maximum values of circulation in these cases are lower than that with the impulsive velocity profile. With the cosine profile, the circulation reaches a peak after an initial increase. The peak

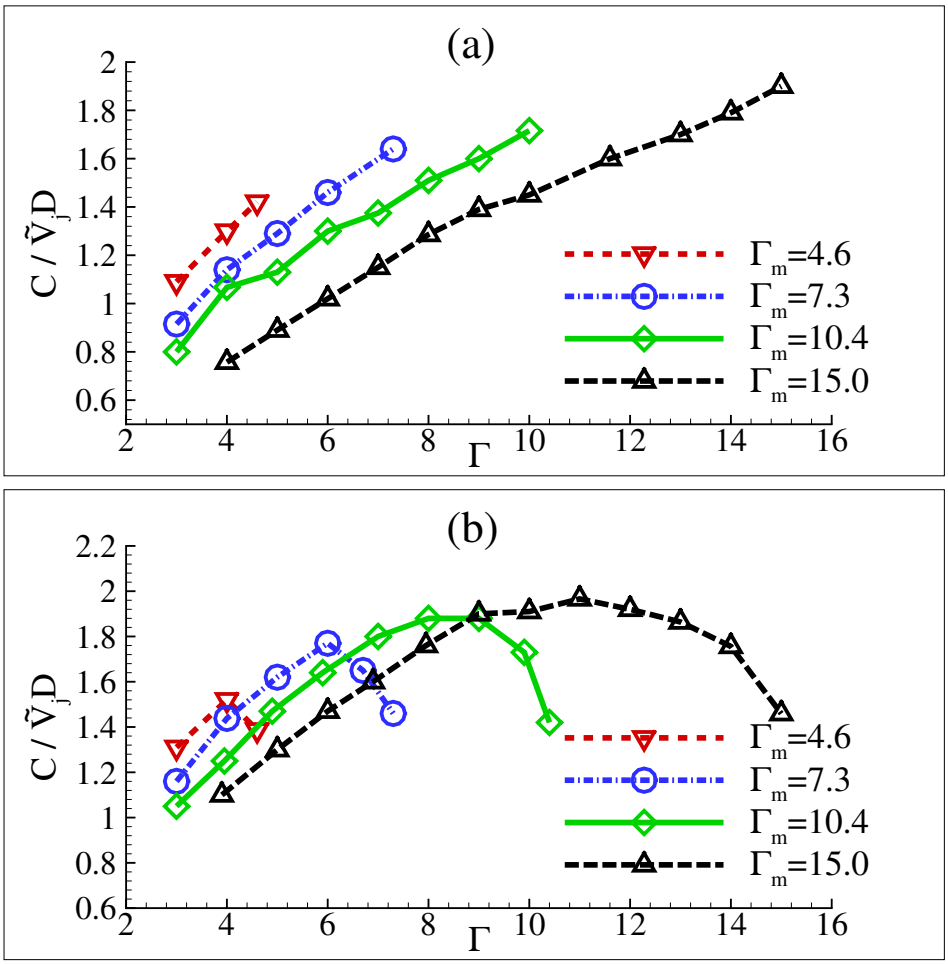

Figure 3.7: Vortex ring circulation C as functions of Γ,(a) half-cosin profile; (b) cosine profile.

occurs approximately at $\Gamma = 0.75 \sim 0.85\Gamma_m$, when the jet speed V_j slows down to $0.3 \sim 0.5\tilde{V}_j$. Afterwards the vorticity supply from the jet is unable to compensate for the viscous dissipation due to the decreasing jet speed and the increasing distance between the ring and the nozzle, so that the circulation of the leading vortex ring is gradually reduced.

An important factor that determines the value of C at any formation number Γ is the time history of the jet speed before that instant. The differences among the impulsive jet profiles with different values of Γ_m are much smaller than those among the cosine (or half-cosine) jet profiles since a significant portion of an impulsive profile is constant. This explains why the C versus Γ curves in the impulsive case are closer to each other than those in the cosine and half-cosine cases.

3.4.3 Thrust generation

We then calculate the instantaneous thrust F_T generated by the jet flow. Since the swimmer is tethered within static fluid, the swimmer sustains negligible drag force so that the net hydrodynamic load on the body F_n is expected to be equivalent to the trust F_T, *i.e.* $F_T \approx F_n$. Note that even though finite drag may be created by the body centroid translation during the body shrinking, its magnitude is far smaller than F_T according to our simulations.

Figure 3.8 displays the instantaneous thrust F_T (approximated by F_n) and jet flux momentum F_j ($\rho D^2 V_j^2$) created by the impulsive jet with various Γ_m. It is shown that after the jet speed V_j reaches its steady value the main source of the thrust F_T is the momentum flux, *i.e.* $F_T \sim F_j$. However, in the initial stage the overall thrust generation is much larger than the contribution from the momentum flux (which is small during the acceleration procedure). The thrust F_T of other two velocity profiles (half-cosine and cosine) are displayed in Fig. 3.9. In the half-cosine profile accelerating jet speed leads to increasing F_T. In the cosine profile positive thrust is created during the accelerating period, whereas during the deceleration period the thrust generation could be negative. Similar to the impulsive profile, the thrust F_T does not match with F_j. It suggests

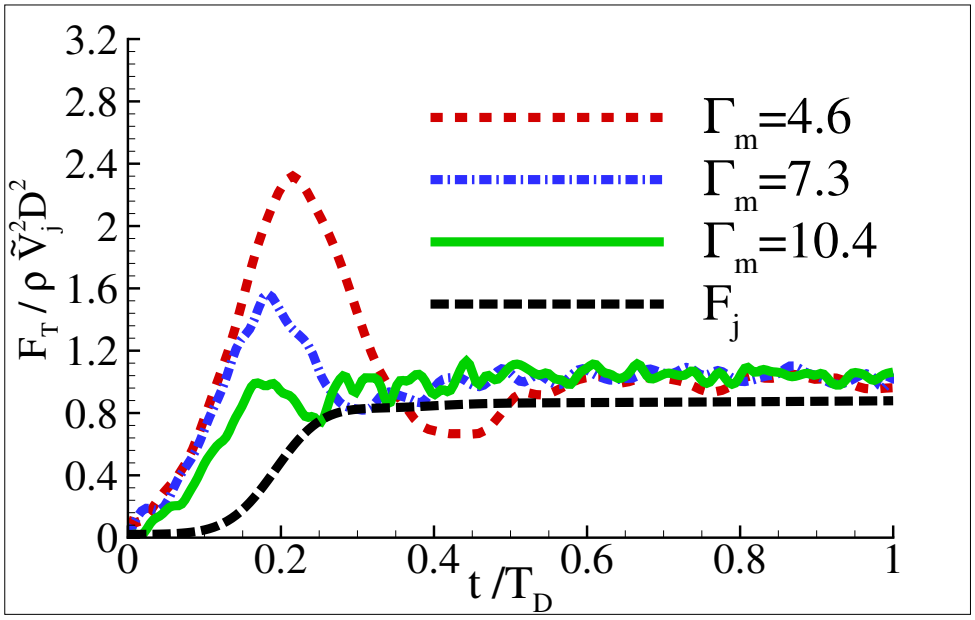

Figure 3.8: Time histories of thrust F_T for various Γ_m. Impulsive jet is applied, and the corresponding jet flux momentum F_j is also plotted.

that there exists other thrust sources that dominate the thrust generation during the unsteady jet process, in which the fluid inertial effect (associated with jet acceleration $a_j = dV_j/dt$) is present. The mechanism of thrust generation will be further illustrated in §3.6.1.

3.5 Recovery process through the inflation deformation

During the recovery (inflation) phase, the swimmer inflates its body back to e_0 to get ready for the next stroke. It is necessary to study the dynamics of the system during the inflation process($t \in (0, T_I)$). Only reversed cosine jet profile (opposite jet direction) will be considered in this section.

Figure 3.10 displays the flow field snapshots visualized through azimuthal vorticity at two different Re_j. It is shown that internal vortices are formed as fluid is sucked into the pressure chamber, yet the vorticity evolution differs significantly between the two cases with different

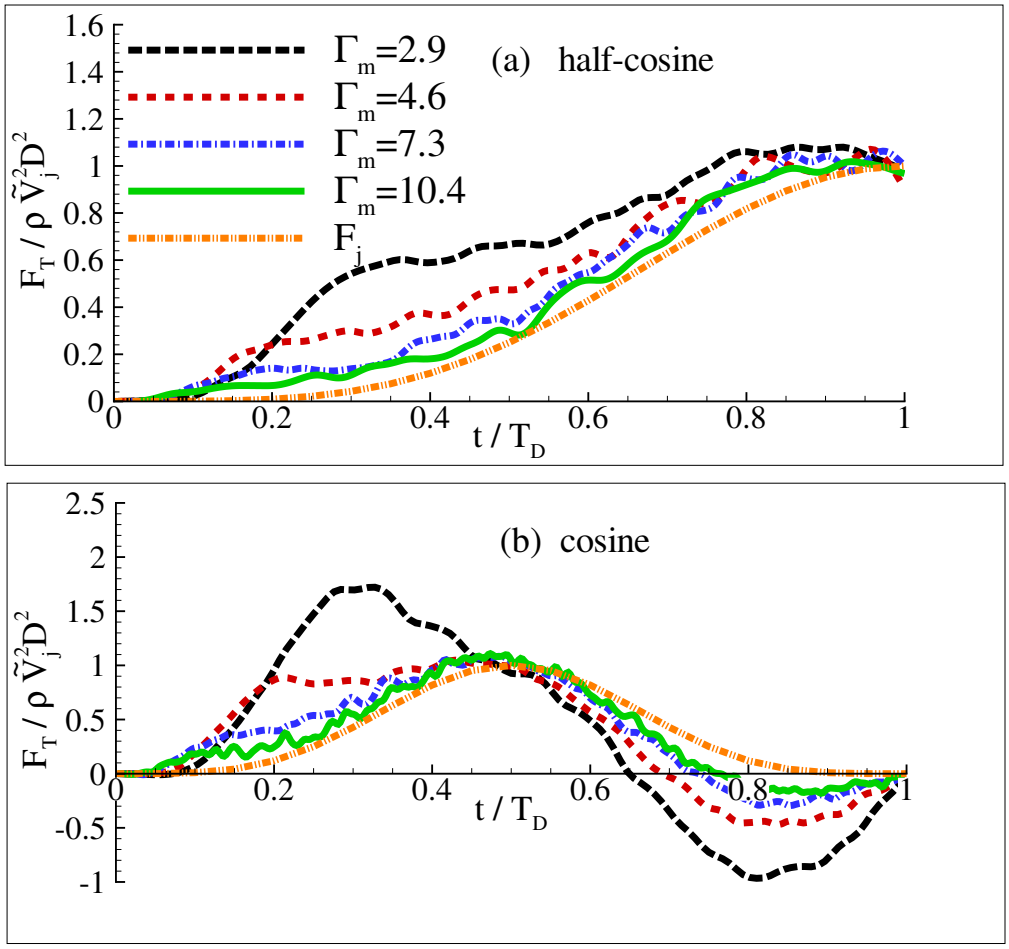

Figure 3.9: Time histories of thrust F_T for half-cosine profile(a) and cosine profile(b).

Reynolds numbers. When $Re_j = 500$, the internal flow consists of a leading vortex and a trailing flow behind. The leading vortex is stopped when it approaches the internal surface of the body, inducing a counter-rotating vortex as the body expands. At $t = 0.75T_I$, this new vortex splits the jet flow into two parts. The leading vortex, the secondary vortex, and the trailing flow then interact with each other till the end of the inflation, when there still exist fairly strong vortices in the chamber. When $Re_j = 50$, however, the jet flow evolution takes a different path. In the chamber no leading vortex is formed due to large viscous effect. Indeed, the jet flow even fails to reach the front wall. At the end of inflation, there is no residual vorticity in the chamber due to dissipation.

Figure 3.11 presents the time evolution of thrust F_T during the inflation. Similar to the deflation phase, F_T is approximated by F_n since the drag force (hydrodynamic load on the outer surface) is negligible. Previously it was believed that the inflation phase generates mostly drag force [49], however we find that although negative thrust is indeed created at the initial stage, it is followed by positive thrust in the remaining time (note that this result is obtained without any incoming flow). Meanwhile, it is shown that the case with $Re_j = 500$ generates greater thrust than the case of $Re_j = 50$. Likewise, the underlying physics will be discussed in §3.6.1.

3.6 Long distance locomotion via cyclic inflation-deflation deformation

To achieve long-distance swimming, the swimmer should perform repeated inflation-deflation body shape change with certain frequency $f = 1/T$(T stands for the time duration of the a whole cycle). We then explore the dynamics of the swimmer in long-distance swimming mode *via* simulations. The computations are conducted within a constant axial free stream u_0. For smooth transition between the deflation and inflation phases, cosine and reversed cosine jet profiles are respectively employed in the two phases, as displayed in Fig. 3.12.

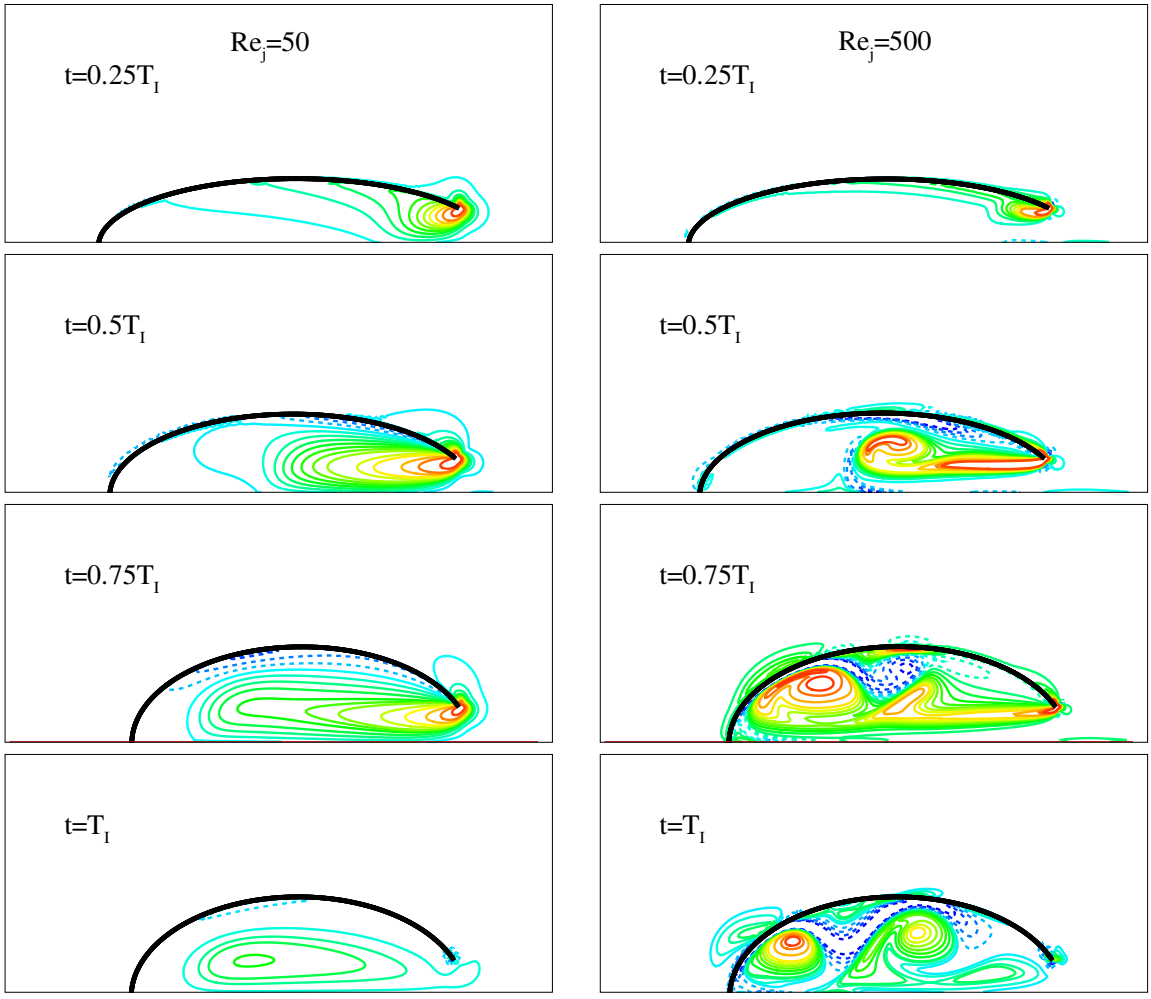

Figure 3.10: Snapshots of vorticity (normalized by $\tilde{V}_j/D$) contour during the inflation. Reverse cosine jet profile is applied.

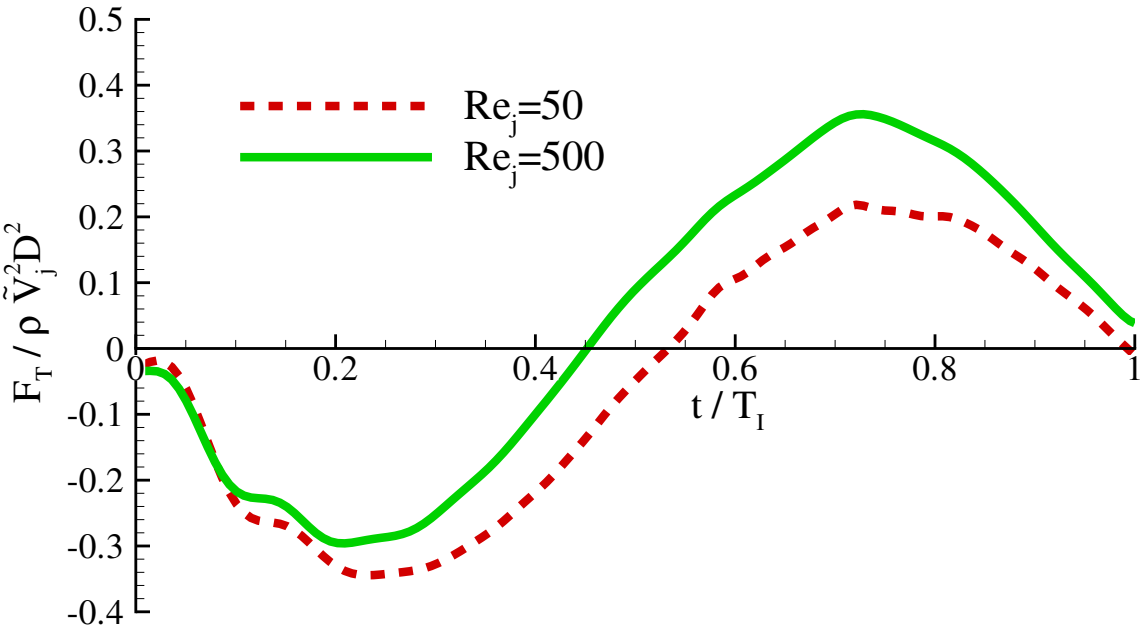

Figure 3.11: Time histories of thrust F_T when $Re_j = 50$ and 500. Reverse cosine jet profile is applied.

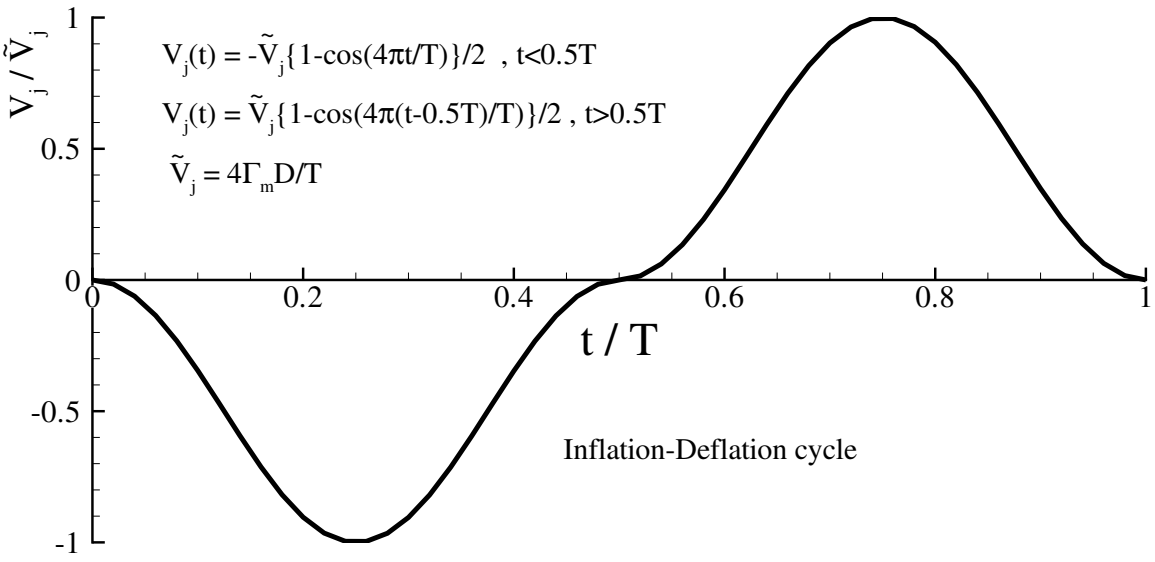

Figure 3.12: The prescribed jet speed profile of a complete deflation-inflation cycle. T is the period of deformation.

Besides the maximum formation number Γ_m (determined by e_0 and e_1) and jet-based Reynolds number Re_j, there are other two important non-dimensional parameters, the incoming-flow Reynolds number Re and the Strouhal number S_t, whose definitions are

$$Re \equiv \rho u_0 D/\mu, \qquad S_t \equiv D/(u_0 T). \tag{3.20}$$

The correlation among those quantities can be expressed as

$$Re_j = 4\Gamma_m S_t Re. \tag{3.21}$$

To ensure that the problem remains axisymmetric, we only consider relatively low Reynolds number ($Re \leqslant 150$). Unless otherwise specified, we choose $\Gamma_m = 10.4$, achieved by setting $e_0 = 0.8$ and $e_1 = 0.95$. The swimming capability is mainly characterized by the mean thrust $\overline{F_T}$ and propulsive efficiency η.

Indeed, the efficiency of locomotion *via* pulsed jetting has been the topic in some existing studies [49–53]. Among these studies, Staaf *et al.* [49] measured the dynamics of squid larvae around 1 mm in body length and found that they could reach swimming efficiency around 20%. Moslemi and Krueger [52,53] experimentally measured the propulsive efficiency of a squid-inspired pulsed-jet propulsion device with a rigid-body design for Reynolds number in the range of $37 - 60$ and $1300 - 2700$, respectively. They found that the efficiency of the jetting process reached $15\% - 32\%$. Hereby the efficiency is defined the conventional way, *e.g.* the useful power (thrust multiplied by forward speed) divided by the total power expenditure (excess kinetic energy shed into the wake plus the useful power). However, in the calculation of thrust these studies rely on simplified models based on the jet flux momentum or the momentum change in the wake (which includes not only the jet but also the body wake; the latter is actually related to drag rather than thrust).

In fact, the efficiency of jet propulsion is often calculated as the Froude efficiency, which has been extended to study pulsed-jet propulsion including both the contraction and the refilling phases [54]. Nevertheless, this is a quasi-steady method using the average forward speed and average jet speed. The detailed time history of the jetting and refilling processes is not considered.

In a broader context of the dynamics of bio-inspired swimmers, for a reasonable estimation of efficiency it is necessary to decompose the overall force on the body into thrust and drag. Otherwise the efficiency based on overall force in steady-swimming scenario, in which thrust and drag are balanced, will be zero. Traditionally, it was proposed to use the drag on a rigid swimmer as a rough approximation for the drag on the deformable body [55]. The accuracy of this approach is limited since body deformation may significantly affect the drag force. In an alternative approach, the longitudinal force is separated into two parts, pressure force and viscous force. At any instant the contribution from each part is counted as either thrust if it is in the swimming direction or drag if it is in the opposite direction [56]. In terms of physical interpretation, this method is very different from the traditional view, in which the thrust force can be either positive (towards the swimming direction) or negative (against the swimming direction). Moreover, with this method there will be nonzero drag force even if the forward speed is zero.

In free swimming mode, our swimmer will sustain three types forces, namely the drag force F_d, the thrust F_T and the added-mass-related force F_a(as described in §1, $F_a = -u_0 \frac{dm_a}{dt}$, where m_a is the added mass [19]). We hereby propose a novel thrust-drag decoupling strategy for pulsed-jet propulsion by utilizing its special characteristics in terms of thrust and drag generation. The thrust-drag decoupling algorithm is based on the physical observations and a control volume analysis on the fluid inside the pressure chamber(see Appendix B). Through the decoupling strategy, the instantaneous thrust F_T is decomposed into three distinct components, namely the jet flux momentum F_j, the excess normal stress at the orifice exit F_σ, and the fluid momentum inside the

body F_m, *i.e.*

$$F_T \approx \iint_A \rho u_x^2 dS + \iint_A (-\sigma - p_\infty) dS + \frac{d}{dt} \iiint_\Omega \rho u_x dV = F_j + F_\sigma + F_m, \tag{3.22}$$

where A denotes the orifice exit plane, p_∞ is the background pressure, Ω represents the fluidic volume inside the pressure chamber. σ is the normal fluid stress, i.e. $-p + \tau$, in which τ is the viscous stress in the axial direction. By using the decoupling method, we can estimate the pure thrust F_T with the information of flow field such as flow velocity and pressure. With F_T being obtained, we can calculate the propulsive efficiency in the traditional manner.

3.6.1 Validation

The validation of our thrust-drag decoupling algorithm is conducted through simulations of three scenarios. The first scenario is a rigid body tethered in background flow ($Re_j = 0$), in which the jet-generated thrust in our definition is expected to be small so that $F_d \approx F_n$ (in this scenario $F_a = 0$ since there is no body deformation). The second and third scenarios involve single deflation and inflation motions without incoming flow (*i.e.* $Re = 0$), in which the incoming-flow-related drag force F_d and added mass force F_a are expected to be negligible so that $F_T \approx F_n$. In these two scenarios the underlying physics of force generation are also examined by using the thrust decomposition technique developed in Appendix B.

a) Rigid body within incoming flow

Physically there should be no thrust generated in this scenario when $Re_j = 0$. Based on our definition, however, there might be a nonzero F_T because due to the disturbance in the wake, the fluid stress at the nozzle plane is not exactly zero. To examine how much error this brings to the result, we simulate the steady flow around a rigid ellipsoidal swimmer with $e = 0.88$ at various values of Re. Table 3.2 lists the measured thrust F_T via Eqn. 3.22 and the drag force F_d calculated

Table 3.2: Thrust, drag comparison when $Re_j = 0$ and $e = 0.88$.

Re	7	20	60	100	150
$F_d/\rho u_0^2 D^2$	-8.15	-3.97	-2.03	-1.52	-1.22
$F_T/\rho u_0^2 D^2$	-0.165	-0.063	-0.034	-0.030	-0.028
F_T/F_d	2.0%	1.6%	1.66%	1.96%	2.29%

as $F_n - F_T$. It shows that even though F_T is non-zero, the values are extremely small (less than 3% in all the cases) in comparison with F_d.

b) Single deflation without incoming flow

In this part we simulate the jetting process through a single deflation when its eccentricity changes from e_0 to e_1 without any incoming flow. Two different values of jet-flow Reynolds number Re_j are considered.

We then calculate the jet-related thrust F_T defined in Eqn. (3.22), *i.e.* $F_T = F_m + F_j + F_\sigma$. Hereby we present the obtained F_T in Figure 3.13a, where the time history of the net force F_n is also plotted. It confirms that F_T stay close to F_n over the whole jetting process, verifying the accuracy of our thrust extraction strategy.

Moreover, the decomposition of thrust into three distinct components helps us understand the underlying physics of force generation. For this purpose we present the three thrust components in Figs. 3.13b, c, d. Based on their definitions, F_j depends on V_j^2, which is always positive. On the other hand, F_m is related to jet acceleration dV_j/dt so that negative F_m is generated when $t > 0.5T_D$. Meanwhile, F_σ is found to be roughly proportional to the jet speed V_j. It is seen that the jet-related thrust F_T could be negative near the end of the deformation when the negative contribution from F_m outweighs the positive ones from F_j and F_σ.

In terms of the effect of Re_j, we found that lower Re_j tends to create larger normalized flux momentum F_j. For further insight, we present the axial velocity distributions along the nozzle radius of these two cases at $t = 0.5T_D$ in Fig. 3.14. The case of $Re_j = 500$ displays a narrower

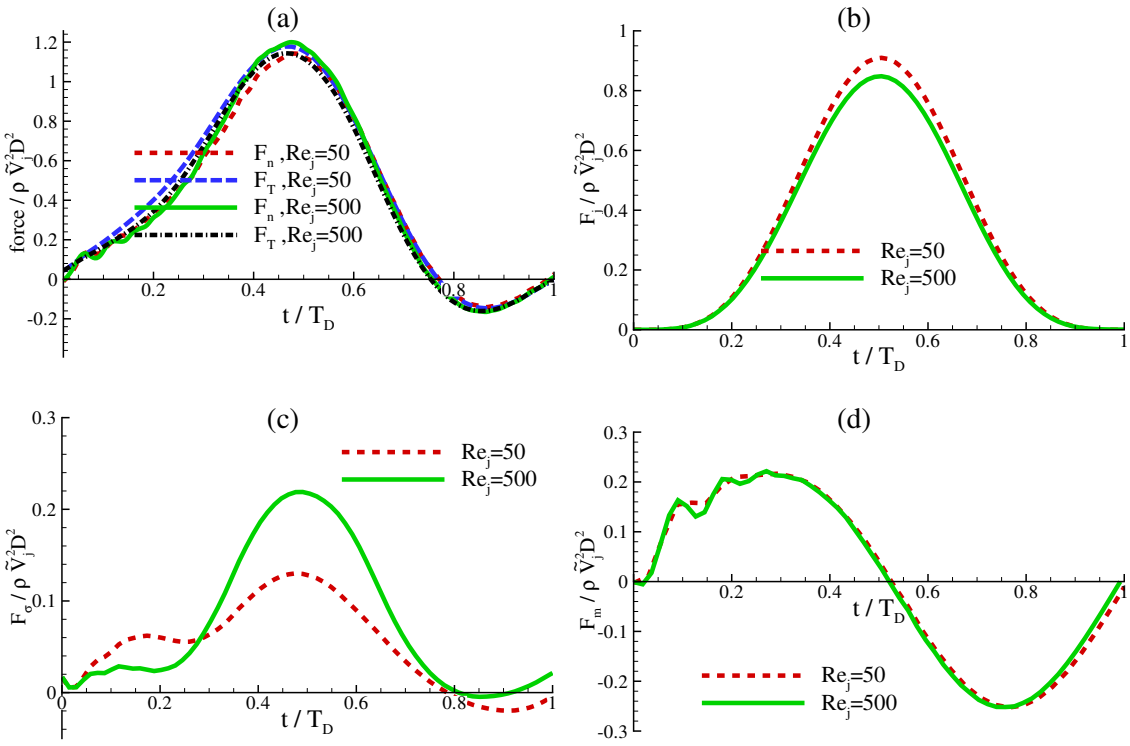

Figure 3.13: (a) Comparison between the net force F_n and jet-generated thrust F_T in a single deflation, (b,c,d) thrust contributions F_j, F_σ and F_m.

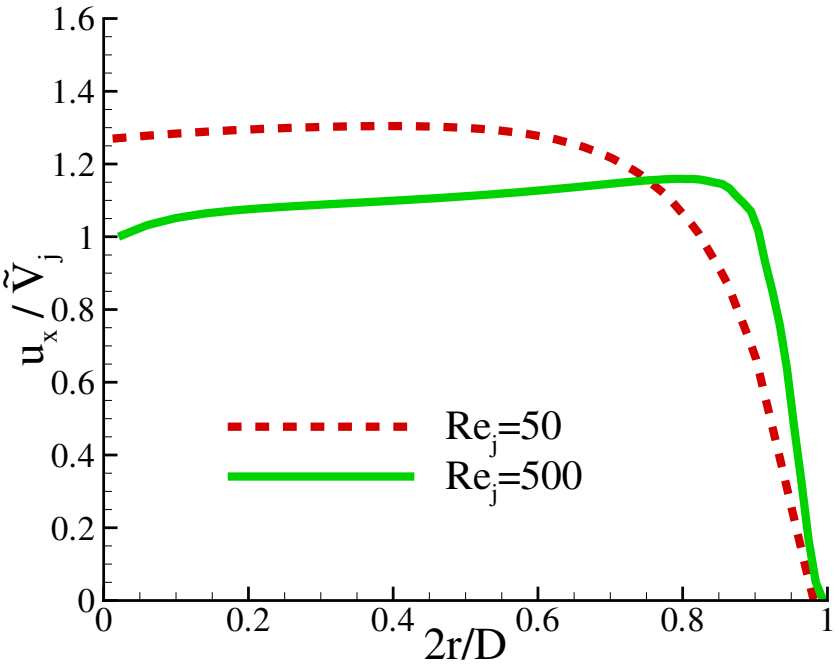

Figure 3.14: Comparison of axial velocity distribution $u_x(r)$ at the nozzle plane between $Re_j = 50$ and 500. Both cases are shown at $t = 0.5T_D$.

boundary layer near the outer surface of the nozzle ($r = D/2$) owing to reduced viscosity, so that the axial flow speed at the nozzle core area, which is the main contributor to F_j, is slightly reduced to keep V_j consistent. Therefore $Re_j = 500$ creates slightly smaller jet flux momentum than $Re_j = 50$ (Fig. 3.13b). It is also seen that higher Re_j leads to larger F_σ due to the reduced viscous stress (Fig. 3.13c). For F_m, Re_j does not play any role since it only depends on jet acceleration.

c) Single inflation without incoming flow

Numerical simulations are also conducted for the dynamics of the system during a single inflation. Similar to the deflation case, F_T matches well with F_n due to the negligibly small effects of F_d and F_a, as shown in Fig. 3.15a.

To understand the physical mechanism, Figs. 3.15b,c and d present the thrust contributions from F_j, F_σ and F_m, which are roughly proportional to V_j^2, V_j and dV_j/dt, respectively. It indicates that F_j is largely balanced by F_σ so that F_T undergoes similar tendency as F_m. The case with

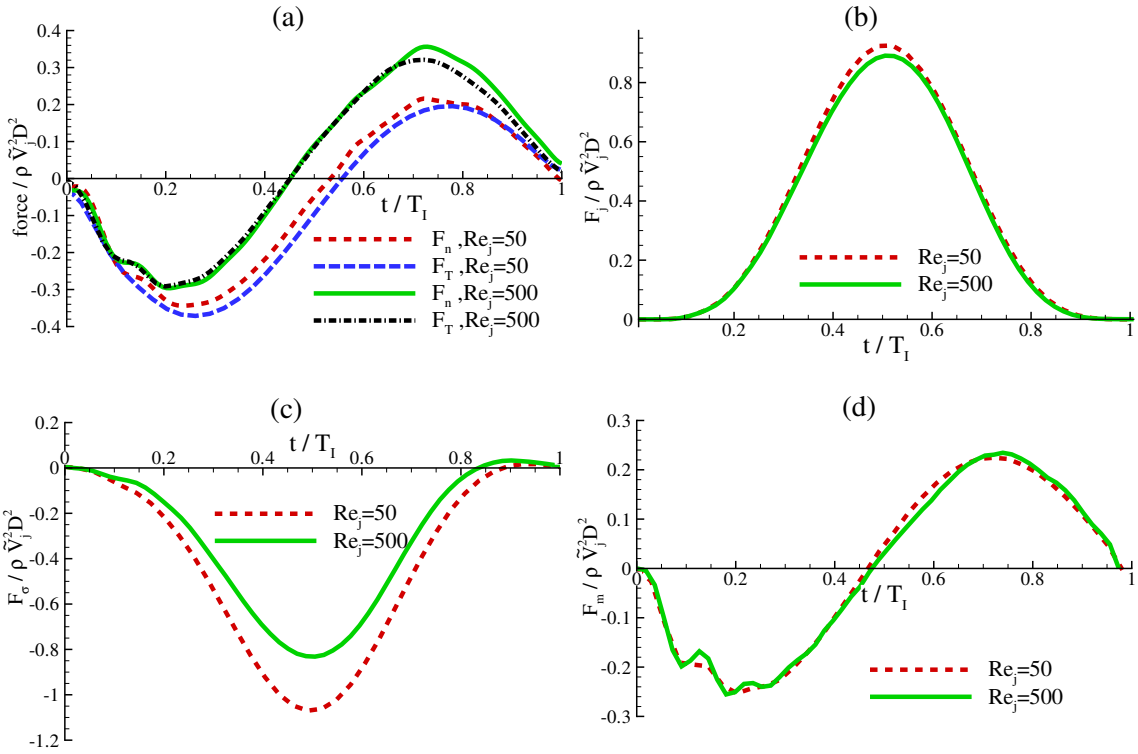

Figure 3.15: Same as Fig. 3.13 except that the deformation is inflation.

$Re_j = 500$ generates greater thrust than the case of $Re_j = 50$. The thrust enhancement mainly results from the decrease of negative F_σ at the nozzle exit while the other two components, F_j and F_m, vary little as Re_j changes.

3.6.2 Time histories over a full cycle

We now consider complete deflation-inflation cycles and study thrust generation and hydrodynamic efficiency in the tethered mode with incoming flow u_0. The thrust-drag decoupling and thrust decomposition methods in Appendix B will be utilized to obtain the jet-generated thrust and the hydrodynamic efficiency. We will examine the effect of Reynolds number and stroke ratio on the whole-cycle propulsive performance. Comparison between the propulsive efficiency obtained using our thrust-drag decoupling method and those from traditional methods will also be conducted.

According to our numerical tests, periodic responses are established after the first deformation cycle. Therefore all results presented in this section will be extracted from the third deformation cycle.

In Figs. 3.16a and b we plot the time evolutions of jet speed and the corresponding body eccentricity over an full deformation cycle for a representative case with $S_t = 0.06$ and $Re = 150$ (in this case $u_0 = 0.4\tilde{V}_j$). Time histories of F_n, F_T (calculated as $F_j + F_\sigma + F_m$) and $F_r = F_d + F_a$ (calculated as $F_n - F_T$) are also displayed in the same figure (see Fig. 3.16c). Since cyclic propulsion is performed in an incoming flow, the drag force F_d and the added-mass-related force F_a can not be ignored. Clearly, F_a is positive during the deflation phase (herein it can be considered as an additional thrust contribution besides the jet-generated thrust) and negative during the inflation phase (thus it can be regarded as additional drag force besides the free stream-generated drag). This explains why the magnitude of F_r is much higher during the inflation phase than during the deflation phase, as shown in Fig. 3.16c. Even though the instantaneous force includes the added

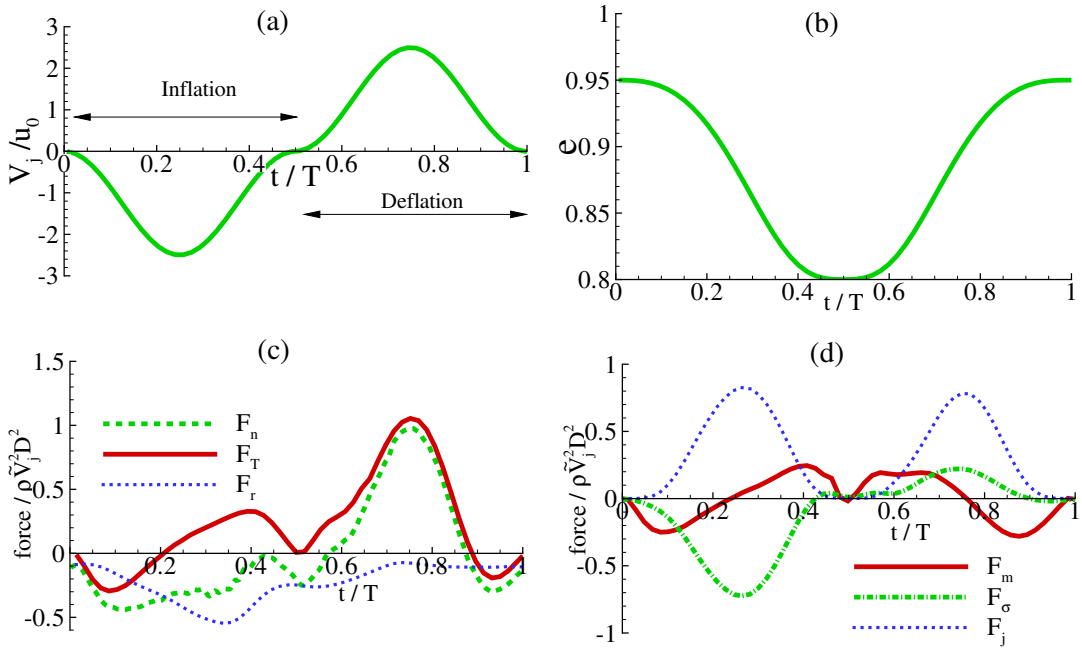

Figure 3.16: Time histories of (a) the jet speed V_j, (b) the body eccentricity e, (c) the net force F_n, the thrust force F_T and $F_r = F_n - F_T$, and (d) the components of the thrust force F_T during a full deflation-inflation cycle. $S_t = 0.06$, $Re = 150$.

mass contribution, the average value of F_a over a full cycle is zero when u_0 is a constant. In this sense, the jet-generated thrust F_T can be regarded as the only source of thrust over a full cycle, and F_d is the only source of resistance.

The components of F_T over a cycle are displayed in Fig. 3.16d. The time-averaged values of F_j, F_σ and F_m are found to be $\overline{F_j} = 0.312\rho\tilde{V}_j^2 D^2$, $\overline{F_\sigma} = -0.105\rho\tilde{V}_j^2 D^2$, and $\overline{F_m} = 0$, respectively. It indicates that only F_j and F_σ contribute to time-averaged thrust generation, and the effect of F_m is negligible with the particular jet profile we use.

3.6.3 Parametric studies

We then perform parametric investigations about the effects of Re and Re_j upon the locomotion dynamics.

Thrust generation

Figure 3.17 summarizes the dependence of the time-averaged thrust $\overline{F_T}$ upon Re under various Re_j. Hereby Γ_m is fixed as 10.4 so that Re_j is determined by the Strouhal number S_t. It shows that when Re_j is relatively small (*e.g.* $Re_j = 20$), the average thrust varies significantly with respect to Re. Specifically, increasing Re tends to cause reduced $\overline{F_T}$. Negative thrust is observed when $Re > 36$. However, the dependence of $\overline{F_T}$ upon Re becomes less pronounced as Re_j increases. Indeed, after normalization $\overline{F_T}$ remains almost a constant within the range of Re when $Re_j > 100$ ($\overline{F_T} \approx 0.21\rho\tilde{V}_j^2 D^2$).

To further understand the effect of Re upon thrust generation, we present the two thrust components F_σ and F_j for the cases of $Re_j = 20$ in Fig. 3.18 (as mentioned earlier the other component F_m does not contribute to time-averaged thrust). According to its definition, the jet flux F_j is determined by the jet velocity, so that Re has negligible effect on it. Therefore the impact of Re on thrust generation rests solely on F_σ (see Fig. 3.18b). It shows that increasing

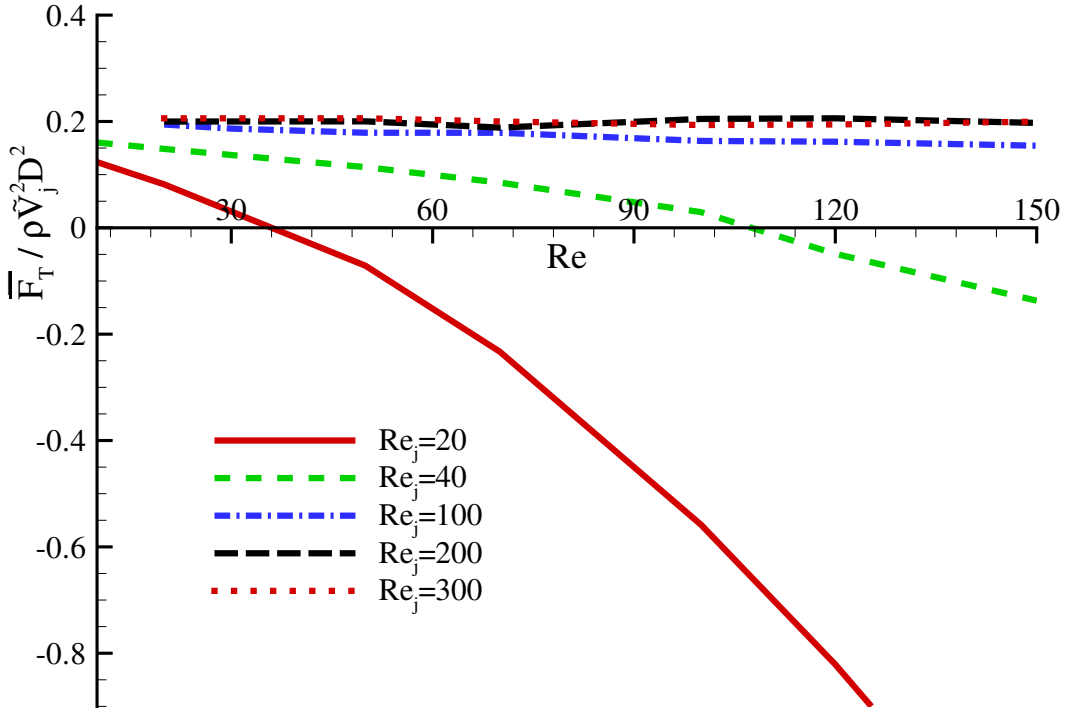

Figure 3.17: Dependence of the time-averaged thrust $\overline{F_T}$ upon Re with different values of Re_j.

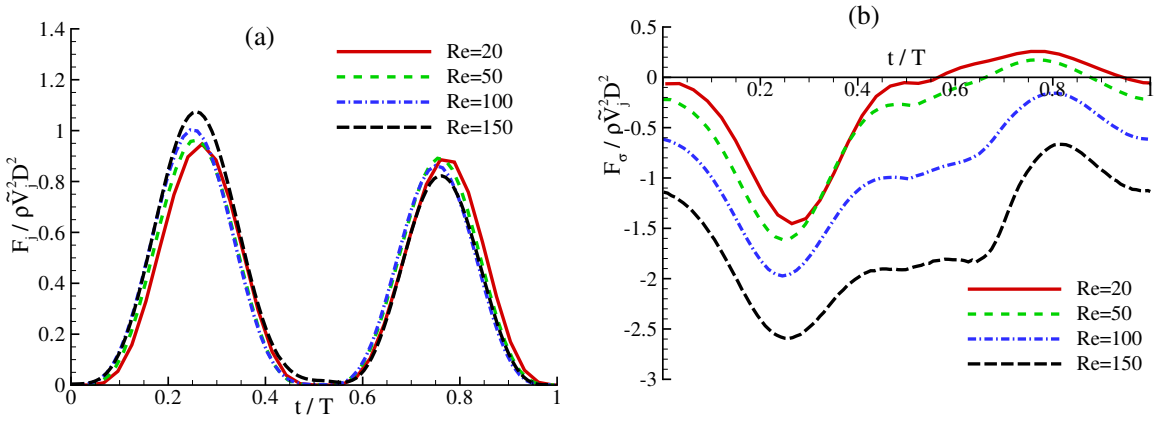

Figure 3.18: Time histories of F_j and F_σ for various Re. $Re_j = 20$.

Re tends to generate reduced stress term F_σ. For further insight, Fig. 3.19 displays the pressure (the predominant contribution to F_σ) and streamline distributions of the flow field at different time instants. It is demonstrated that for low Re cases (*e.g.* $Re = 10$), the free stream starts to separate from the surface of the outer shell, forming a closed recirculating vortex ring in the wake at $t = T/2$ (the end of inflation phase). The body-generated vortex ring is quickly pushed downstream and dissipated away in the deflation phase under the effect of the high-speed jet flow (note that in this case the jet flow is relatively strong compared with the incoming flow). As Re grows (*e.g.* $Re = 100$), a much stronger body-generated vortex ring exists after the inflation phase, accompanying the presence of a negative pressure region on the rear side of the body (see Figs. 3.19f,g). This can be the reason why higher Re leads to lower F_σ, as displayed in Fig. 3.18b. Meanwhile, we find that this vortex ring is sufficiently strong to survive well into the deflation phase. Indeed the reverse flow within the vortex ring forms a 'virtual wall' that blocks the jet flow. However, the influence of this virtual 'ground effect' on thrust generation is not pronounced in our simulations.

For relatively high Re_j (*e.g.* $Re_j = 100$), The jetting dynamics will be dominated by the high-speed jet and insensitive to the free stream. Figure 3.20 displays the time histories of F_j and F_σ when $Re_j = 100$. As expected, Re makes little difference on both of them.

Propulsive Efficiency

As noted earlier, the thrust-drag decoupling method allows us to define the propulsive efficiency in the traditional manner. We have

$$\eta = \frac{\overline{F_T} u_0}{\overline{P_{in}}}, \tag{3.23}$$

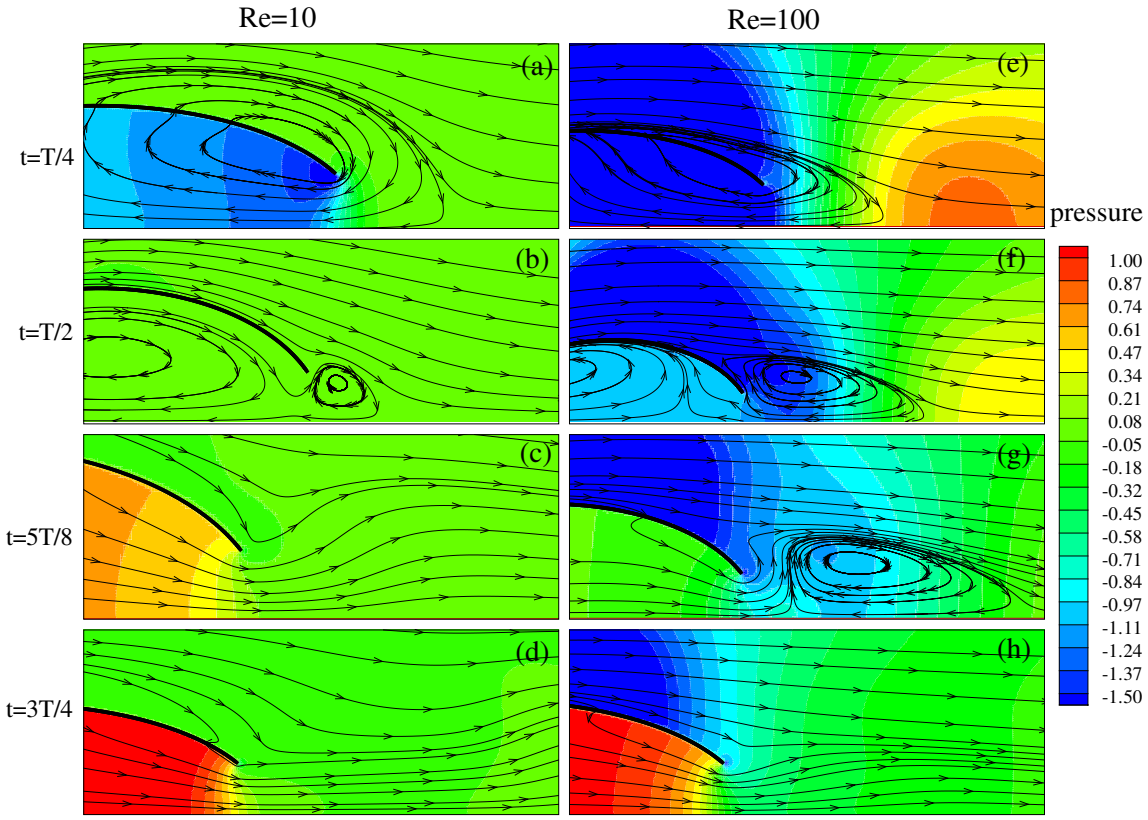

Figure 3.19: Snapshots of the flow fields for the case of $Re = 10$ and 100 with $Re_j = 20$. The flow fields are visualized through streamlines and normalized pressure distribution ($p/\rho\tilde{V}_j^2$).

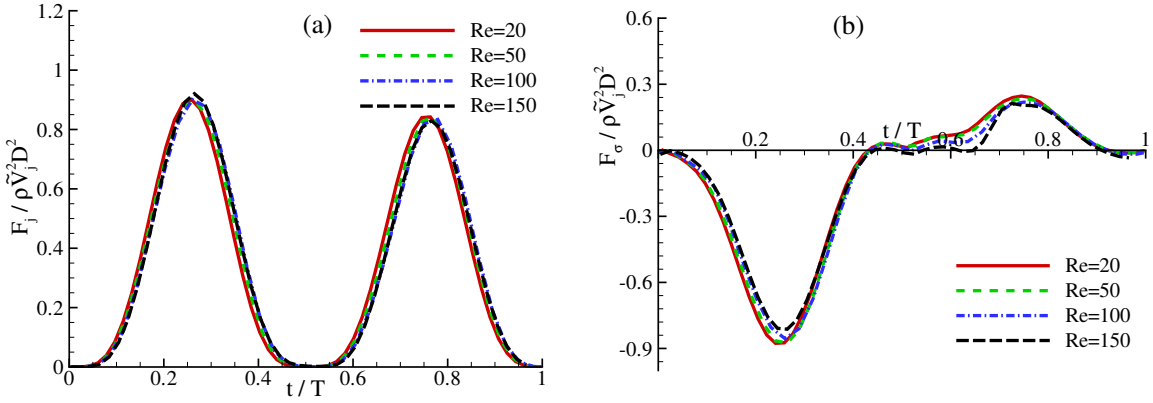

Figure 3.20: Same as Figure 3.18 except that $Re_j = 100$.

where $\overline{P_{in}}$ represents the average power expenditure per cycle, *i.e.*

$$\overline{P_{in}} = \frac{\int_T \int_{\Gamma_{ib}} 2\pi r(s) \boldsymbol{F} \cdot \boldsymbol{U} ds dt}{T}. \tag{3.24}$$

In Fig. 3.21a we present the dependencies of efficiency η, average net force $\overline{F_n}$ and average drag $\overline{F_r}$ over a complete cycle upon Re for the case of $Re_j = 200$ (since the time-averaged value of the added-mass-related force F_a is zero, in the cyclic motion case $\overline{F_r}$ coincides with the time-averaged drag force). As expected, both efficiency and drag force rise with increasing Re. This efficiency definition is physically relevant in the scenario when the propeller is applied in an underwater locomotion system with constant swimming speed u_0. However, it is inappropriate for efficiency measurements if the propeller works as a stand-alone swimmer since the prescribed u_0 does not necessarily match the free-swimming speed. To address this issue, we approximate the average free-swimming speed as the free-stream speed u_0 (or, alternatively, the incoming flow Reynolds number Re) when the average net force on the system $\overline{F_n}$ disappears. For example, this 'steady-swimming' (or 'free-swimming') state of $Re_j = 200$ is reached at $Re = 60$, where the efficiency η equals 0.21. Through this approach, the steady-swimming efficiency at other values of Re_j and the corresponding steady-swimming Re can be obtained. As shown in Fig. 3.21b, increasing the jet speed (Re_j) requires higher Re to achieve steady swimming. The efficiency η is also increased as Re_j rises.

Meanwhile, we have also evaluated the steady-swimming efficiencies using existing approaches discussed in the introduction. These definitions of efficiency are physically equivalent to the one used in the present study. Specifically, $\eta_{_R}$ is defined by using the traditional thrust-drag decoupling method in which the drag on the deforming body is approximated by the drag on a rigid body [55], *i.e.*

$$\eta_{_R} = \frac{(\overline{F_n} - F_{D_{_R}})u_0}{P_{in}}, \tag{3.25}$$

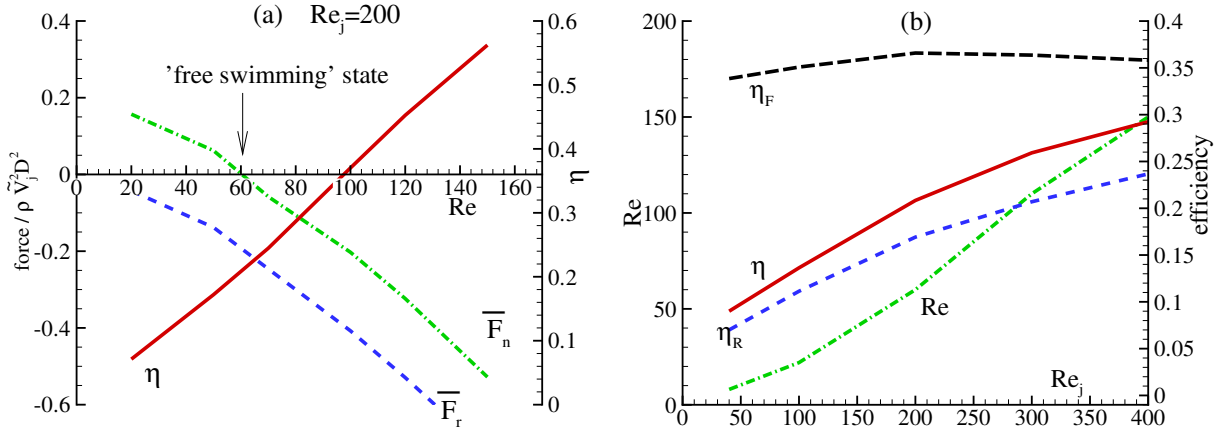

Figure 3.21: (a) Dependencies of the average net force $\overline{F_n}$, average drag $\overline{F_r}$ and efficiency η upon Re when $Re_j = 200$, (b) steady-swimming efficiency and Re as functions of Re_j.

where F_{D_R} is the drag force on the body whose eccentricity $e = (e_0 + e_1)/2$.

Another propulsive efficiency, η_F, is calculated as

$$\eta_{_F} = \frac{2u_0\overline{V_j}}{2u_0\overline{V_j} + 3u_0^2 + \overline{V_j}^2}, \tag{3.26}$$

where $\overline{V_j}$ is the average jet speed. Originated from the Froude efficiency, $\eta_{_F}$ was proposed by Anderson and Demont [54] to calculate the whole-cycle propulsive efficiency of jet-propelled organisms such as squid and scallops. Note that Eqn. (3.26) is valid when the average jet speed in deflation equals the average flow intake speed in inflation, which is consistent with the jet profile we consider herein.

As shown in Fig. 3.21b, $\eta_{_R}$ is only slightly below η and they share the same trend as Re_j increases. $\eta_{_F}$, on the other hand, is significantly higher than η or $\eta_{_R}$, especially when Re_j is small. The implication is that this simplified definition may significantly overestimate the propulsive efficiency, at least in the low Reynolds number regime.

It is necessary to point out that the 'steady-swimming' or 'free-swimming' state in this

analysis is defined in the time-averaged sense. In a real free-swimming case the forward speed is unlikely to be a constant. In fact, a more likely scenario is that the forward speed is larger in the deflation phase and smaller in the inflation phase. The net contribution of the added mass related thrust F_a averaged over a cycle will be positive [57]. Due to this effect the analysis based on the tethered scenario may underestimate the propulsive performance of the system. The predicted steady-swimming efficiency is thus a lower bound of the actual efficiency in free swimming.

Effect of stroke ratio

As demonstrated in §3.4.2, there is a universal scaling law that governs the vortex ring formation of pulsed jetting at intermediate and high Re_j ($\simeq 2000$) [46]. Nevertheless, at low Re_j ($\simeq 150$) the pulsed jetting is a very smooth process, in which the *pinch-off* scenario does not happen. With the sinusoidal jet profile there does not exist a universal formation number featuring the saturated state of the vortex ring. For this reason we anticipate that the maximum stroke ratio Γ_m plays a less important role in the performance of the system we consider. Instead, it is indirectly involved since it determines the value of Re_j in the steady-swimming case (see Eqn. (3.21)). To illustrate its effect we conduct simulations by using two additional values of Γ_m, 2.9 and 4.6, in which the fully inflated states correspond to $e_0 = 0.92$ and 0.9, and the fully deflated state e_1 is fixed at 0.95 (see Table 3.1).

As shown in Fig. 3.22a, the variation of Γ_m does not lead to much difference in the thrust with Re_j unchanged. However Γ_m is found to play certain role in drag generation. As displayed in Fig. 3.22b, less drag force is generated in $\Gamma_m = 4.6$ than in $\Gamma_m = 10.4$, particularly within the large Re regime. This is because smaller Γ_m corresponds to less inflated body. Therefore, at $\Gamma_m = 4.6$ higher Re is required to compensate the drag loss to maintain the steady-swimming state. As shown in Fig. 3.22b, at $Re_j = 200$ the steady-swimming Re for $\Gamma_m = 4.6$ rises to 70 (instead of 60 for $\Gamma_m = 10.4$). We note that the inflated state at $e_0 = 0.92$ is geometrically close to the

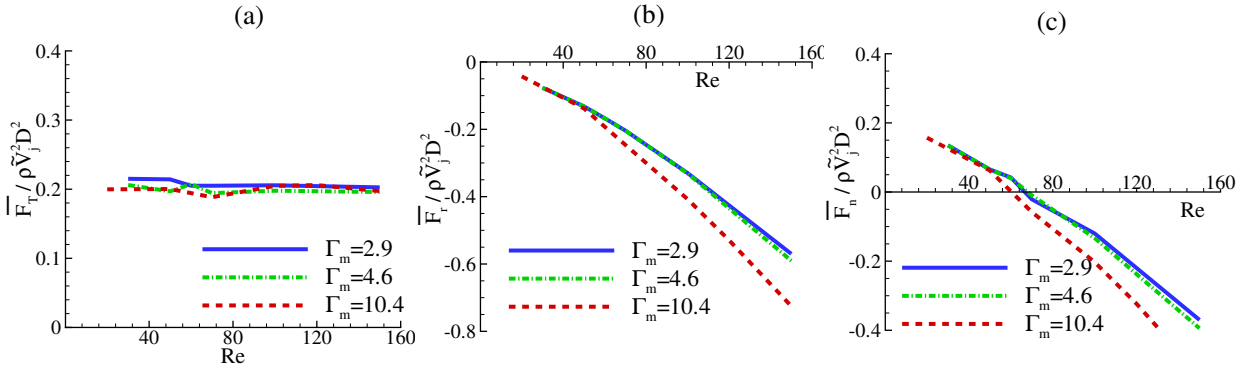

Figure 3.22: Dependencies of (a) the average thrust $\overline{F_T}$, (b) the average drag $\overline{F_r}$ and (c) the average net force $\overline{F_n}$ on Re at various values of Γ_m. $Re_j = 200$.

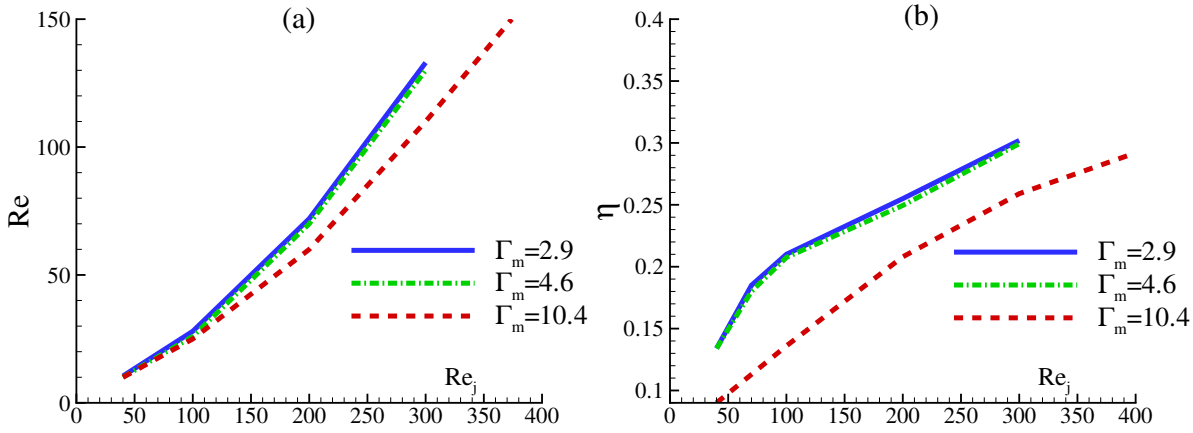

Figure 3.23: (a) Steady-swimming Reynolds number Re and (b) steady-swimming efficiency as functions of Re_j at various values of Γ_m.

one at $e_0 = 0.9$ so that the difference between $\Gamma_m = 2.9$ and 4.6 is far less pronounced. We then present the steady-swimming Re and efficiency as functions of Re_j for these three stroke ratios in Fig. 3.23. As expected, decreasing Γ_m results in higher steady-swimming Re and propulsive efficiency.

3.7 The impact of nozzle geometry

A key component of a squid's jet propulsion system is the funnel tube, which functions as a nozzle from which the jet flow is formed (see Fig. 1.1). Other species, *e.g.* jellyfish, do not have such a morphological feature so that they are not capable of creating high-speed jet flows. This significantly limits the swimming speed they are able to reach. A squid's funnel tube can be pointed at a range of directions so that maneuvers can be achieved through thrust vectoring. The exact shape and size of the nozzle are also important factors in determining the performance. It is thus of interest to examine effects of the design of a nozzle on the propulsion performance through pulsed jetting.

The dynamics of pulsed-jet propulsion utilized in squid swimming have been investigated through laboratory observations and measurements of live animals [21–23], experiments on bio-inspired jetting tubes or robotic devices [25, 26, 46, 58, 59], and numerical studies [17, 60–62]. However, few of these studies examine the effect of detailed geometry of the nozzles on the dynamics of the system. One exception is the experiment conducted by Krieg & Mohseni [63]. By measuring the thrust generation of a piston jetting device with either tubular or conical nozzles, they concluded that conical tubes outperform tubular ones in terms of force generation.

Inspired by these studies, we hereby conduct a numerical investigation concentrating on the force generation capacity of the axisymmetric jet propulsion system with a nozzle. Systematic simulations will be conducted to study the dynamics of the system with different nozzle character-

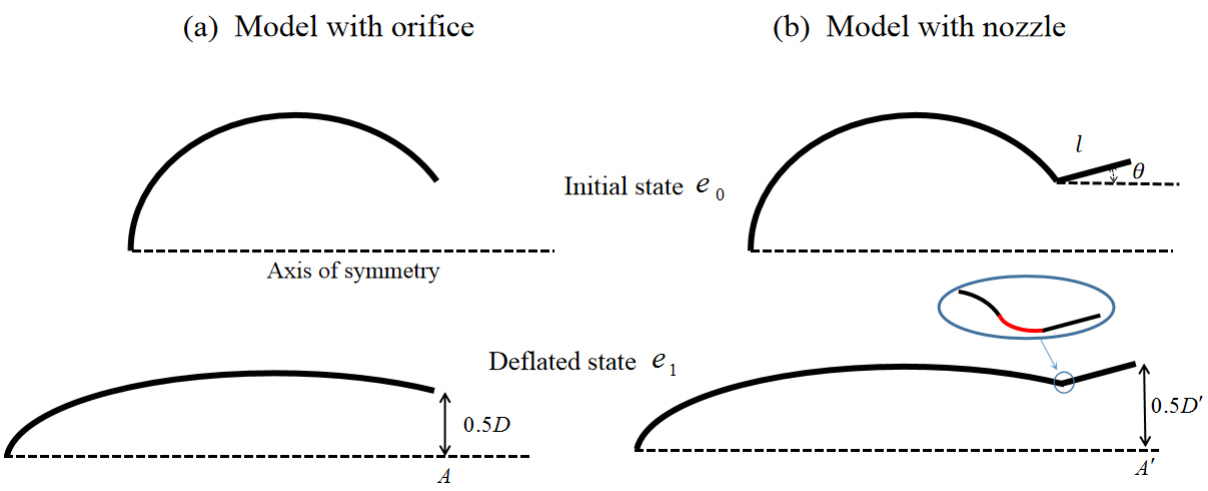

Figure 3.24: Rendition of the axisymmetric squid-inspired system with orifice(a) and nozzle tube(b).

istics (*e.g.* length and angle). Figure 3.24a displays the geometry of the original squid-inspired propulsive system which includes a pressure chamber and an orifice. We attach an axisymmetric nozzle to the ellipsoidal body at the orifice (Fig. 3.24b). To minimize energy loss the nozzle and the body are joined smoothly as demonstrated in the inset. The nozzle configuration is characterized by two independent parameters, *i.e.* the contour length l and angle of inclination θ. Hereby a variety of nozzles with different l and θ will be tested while the body geometry (including the size of the orifice) and deformation remain unchanged. In this section, we consider the escaping mode (via single body deflation) without incoming flow u_0. Thereafter, cosine jet profile will be used for all simulations and Re_j is chosen to be 50.

Quantities with subscript '1' are related to quantities on the deformable body, while subscript '2' is used to depict quantities on the nozzle. For instance, let F_1 and F_2 be the hydrodynamic force acting on the deformable body Γ_{ib} and the nozzles Γ_n, respectively. We have

$$F_1 = -\int_{\Gamma_{ib}} 2\pi r F_x(s,t)ds, \qquad F_2 = -\int_{\Gamma_n} 2\pi r F_x(s,t)ds. \tag{3.27}$$

The overall thrust F_T of the whole system (with a nozzle) is then the summation of F_1 and F_2, *i.e.* $F_T = F_1 + F_2$. Note that by definition positive F_T, F_1 and F_2 all point towards the $-x$ direction. The instantaneous power expenditure P is calculated by

$$P = \int_{\Gamma_{ib}} 2\pi r \boldsymbol{F} \cdot \boldsymbol{U} ds. \tag{3.28}$$

To evaluate the efficiency, we then define a dimensional quantity called the cost of impulse COI, which is the ratio between the overall energy expenditure and the generated impulse calculated as

$$COI = \frac{\overline{P}}{\overline{F_T}}, \tag{3.29}$$

where $\overline{F_T}$ is the time-averaged thrust and $\overline{P}$ is the mean power expenditure. Higher COI corresponds to lower efficiency. The concept of cost of impulse stems from cost of transport that has been widely used to evaluate the locomotion efficiency of aquatic animals.

Quantities with subscript '0' are related to the system without nozzles. We first analyze the dynamics of the model with no nozzle as shown in Fig. 3.24a. The results will be used as a reference for the subsequent simulations with various nozzles included. After normalization, the time-averaged thrust, power expenditure and the cost of impulse in this particular case are $\overline{F_0} = 0.42$, $\overline{P_0} = 0.35$, $COI_0 = 0.831$, respectively. The first two quantities are actually F_1 and P for the case of orifice jetting.

Next, a variety of nozzles with different combinations of l and θ will be affixed to the body and tested with the prescribed body deformation. We will evaluate the influence of nozzles on the original propulsion system (see Fig. 3.24a) by using $\lambda_1 = \frac{\overline{F_1} - \overline{F_0}}{\overline{F_0}}$. The synthetic performance of the entire system (including the deformable body and the nozzle), characterized by $\lambda = \lambda_1 + \lambda_2$ (where $\lambda_2 = \overline{F_2}/\overline{F_0}$), $\overline{P}/\overline{P_0}$ and COI/COI_0, will also be examined.

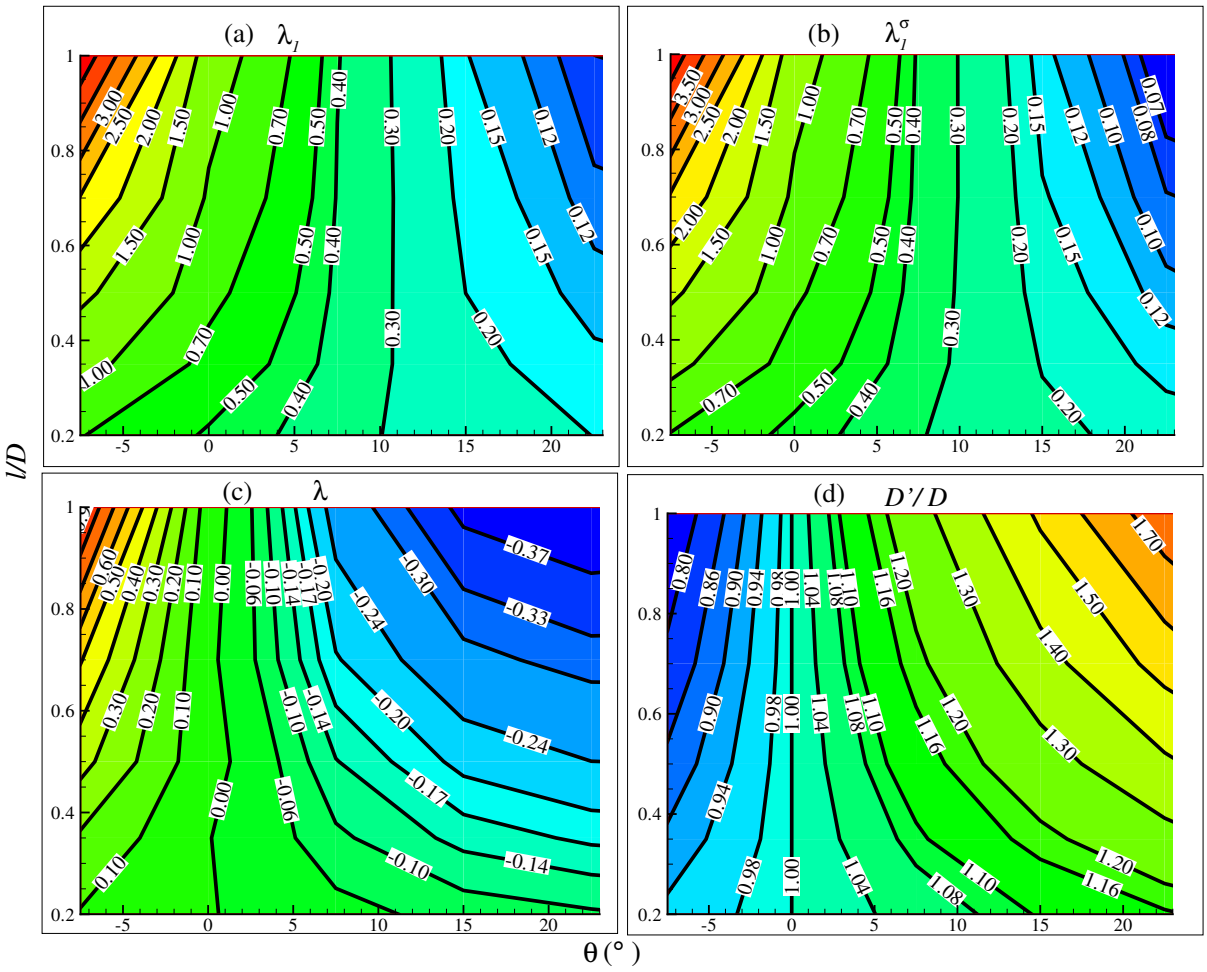

Figure 3.25: λ_1,λ_1^σ,λ and the nozzle exit diameter D' as functions of the nozzle contour length l and the inclination angle θ.

3.7.1 Thrust generation

The thrust decomposition scheme (Eqn. (3.22)) can be applied to the thrust F_1. After time averaging, we have $\overline{F_1} \approx \overline{F_1^j} + \overline{F_1^\sigma} + \overline{F_1^m} \approx \overline{F_1^j} + \overline{F_1^\sigma}$ (since $\overline{F_1^m} \approx 0$ as discussed in §3.6.2). Therefore λ_1 can be decomposed into $\lambda_1^j = \frac{\overline{F_1^j} - \overline{F_0^j}}{\overline{F_0}}$ and $\lambda_1^\sigma = \frac{\overline{F_1^\sigma} - \overline{F_0^\sigma}}{\overline{F_0}}$. Since the body deformation remains unchanged, the mean axial flow speed at the orifice is expected to be unchanged as well ($\overline{F_1^j} \approx \overline{F_0^j}$). Subsequently, λ_1^j is small so that λ_1 is dominated by λ_1^p. Figures 3.25a,b demonstrate the values of λ_1 and λ_1^σ as functions of l and θ. The consistency between λ_1 and λ_1^σ confirms that after the installation of nozzles, the enhancement of thrust on the deformable body is mainly attributed to the pressure augmentation at the orifice plane A.

Even though with a nozzle added there is significant increase in the thrust on the deformable body ($\overline{F_1} > \overline{F_0}$ according to Fig. 3.25a), the nozzle itself may sustain considerable drag force (*i.e.* $\lambda_2 < 0$) when the flow goes through them so that it is not clear if there is a net gain in the thrust on the whole body including the deformable part and the nozzle. It is necessary to measure the overall thrust created by the whole system, which is characterized by λ. In Fig. 3.25c, we present the value of λ as a function of l and θ. It is shown that tubular nozzles ($\theta = 0$) has little impact on the thrust generation of the whole system (*i.e.* $\lambda \sim 0$), which means that the thrust increase on the deformable part is almost canceled by the drag force acting on the nozzle. Systems with converging nozzles ($\theta < 0$) tend to produce higher thrust ($\lambda > 0$) while those with diverging nozzles ($\theta > 0$) will produce reduced thrust ($\lambda < 0$).

Figure 3.25d presents the dependence of the nozzle exit diameter D' on l and θ. Note that hereafter the quantities defined at the nozzle exit plane A' are labeled by adding primes to their counterparts at the orifice plane A. Upon closer inspection, it is found that the contour lines of D' (Fig. 3.25d) are roughly correlated with those of λ (Fig. 3.25c), which implies that the thrust generation of the entire system is closely related to the nozzle exit diameter D', or alternatively the jet speed at the nozzle exit V_j' since the body deformation is given.

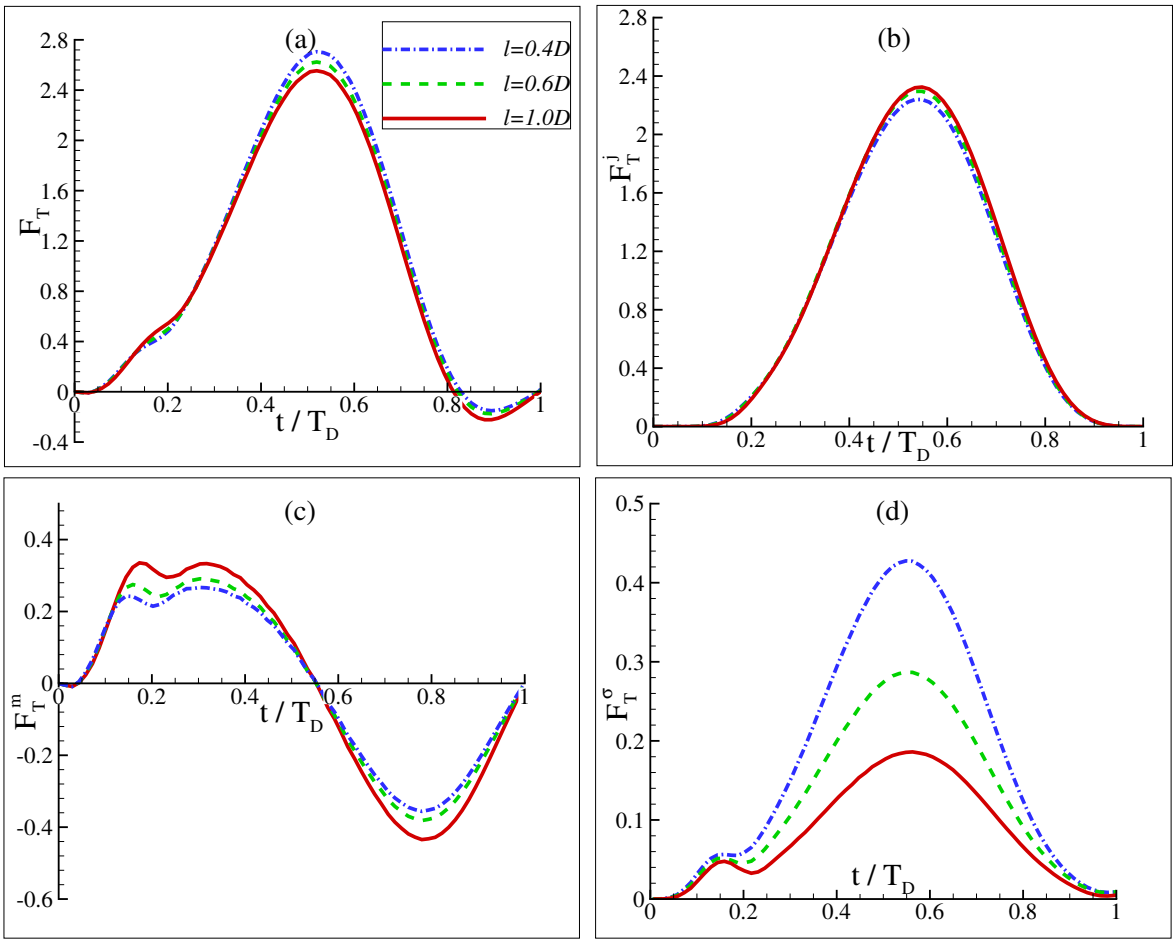

Figure 3.26: (a) The whole-system thrust F_T and (b,c,d) their three components for different converging nozzles. The force is normalized by $\rho \tilde{V}_j^2 D^2$.

To throw light upon the above phenomenon, we apply the decomposition strategy to the entire propulsive system. Via this approach, the whole-system thrust $F_T = F_1 + F_2$ can be decoupled into three parts: F_T^j,F_T^σ and F_T^m, where F_T^j and F_T^σ are defined at the nozzle exit A' and F_T^m is based on the overall fluidic volume including the fluid inside the pressure chamber and the nozzle. In the following we will use the thrust decomposition to study the force generation at three different scenarios, converging nozzle, tubular nozzle, and diverging nozzle.

a) Converging nozzles

We examine three converging nozzles ($\theta < 0$) with the exit size being fixed at $D' = 0.7D$. The

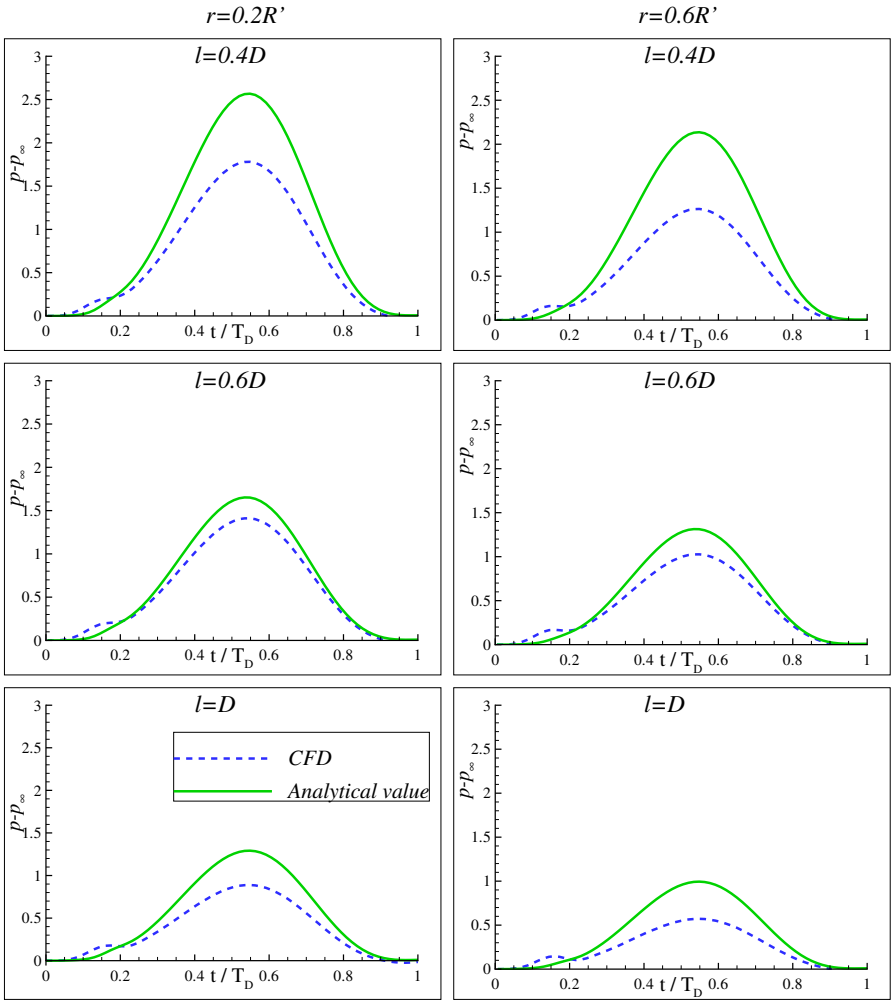

Figure 3.27: Comparisons between the numerically obtained over-pressures and the analytical values at the monitoring locations for the converging nozzles. The pressure is non-dimensionalzied by $\rho \tilde{V}_j^2$

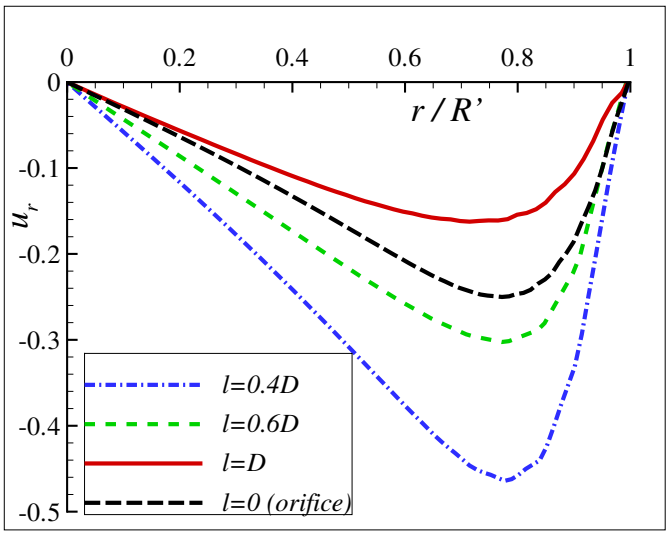

Figure 3.28: Comparison of radial velocity profiles on the exit of converging nozzles, $t = 0.5T_D$. The velocity is normalized by $\tilde{V}_j$.

combinations of geometry parameters (l, θ) for these nozzles are, respectively, $(0.4D, -22°)$, $(0.6D, -14.5°)$ and $(D, -8.6°)$. Figure 3.26a shows that these three cases generated almost the same thrust F_T. With the nozzle exit diameter D' being a constant, F_T^j is nearly unchanged for various converging nozzles as shown in Fig. 3.26b (the slight difference is attributed to the discrepancy in spatial distribution of the axial velocity at A'). Figure 3.26c demonstrates the time histories of F_T^m, which is found to have similar dependence upon the jet acceleration as F_0^m. Although the magnitude of F_T^m becomes higher as l increases, the time-averaged values are always close to zero. We then present the fluid stress term F_T^σ in Fig. 3.26d. There is indeed significant differences among the three cases. However, it is observed that F_T^σ only accounts for a small percentage of the overall thrust F_T. Instead, F_T^j is the dominant source in F_T, which depends on the nozzle exit size D'.

Interestingly, the time evolution of F_T^σ displays a twin-peak feature. A minor peak occurs in the initial stage, followed by a major peak near the middle of the jetting process. The magnitude of the first peak varies very little among the three cases, whereas there is a notable difference for

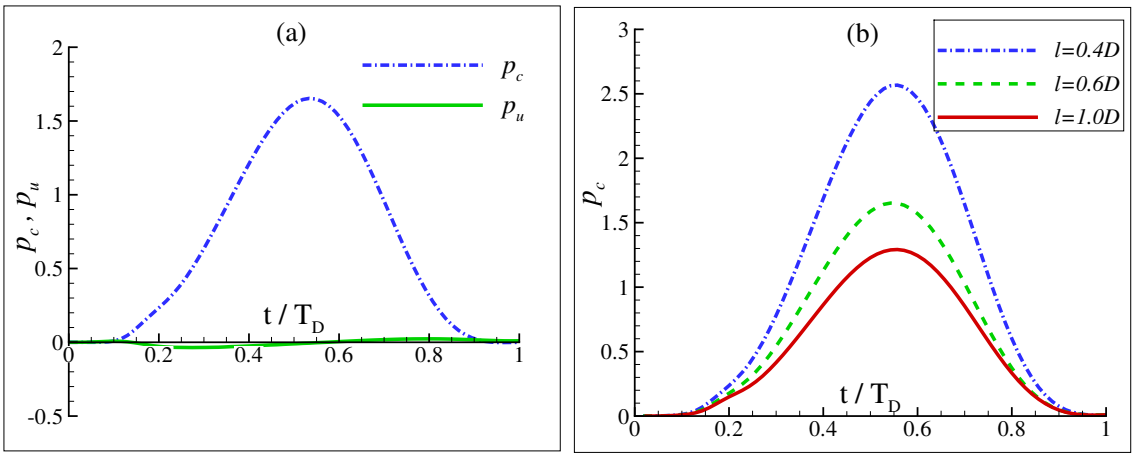

Figure 3.29: (a) p_c and p_u for a converging nozzle with $l = 0.6D$ and $\theta = -14.5°$; (b) comparison of p_c for various converging nozzles. The monitoring point is $r = 0.2R'$. The pressure is normalized by $\rho\tilde{V}_j^2$.

the second one. In order to investigate the mechanism of F_T^σ generation during the jet pulsation, in Fig. 3.27 we plot time histories of the over-pressure $p - p_\infty$ at two representative locations on the nozzle exit, $r = 0.2R'$ and $0.6R'$ (where $R' = 0.5D'$) since F_T^σ is mostly contributed from $F_T^p = \iint_{A'}(p - p_\infty)dS$ (see Appendix B). The over-pressure is found to experience similar tendencies as F_T^σ. It is thus necessary to study the underlying mechanism of over-pressure on the exit.

Based on the unsteady inviscid flow theory, Krieg & Mohseni [63] derived an analytical model to determine the over-pressure distribution along the exit boundary for axisymmetric jet flow, *i.e.*

$$\frac{p(r) - p_\infty}{\rho} = \int_r^{R_\infty} \left(\frac{\partial u_r}{\partial t} + \mathbf{u} \cdot \nabla u_r \right) d\varpi, \tag{3.30}$$

where R_∞ is the infinity in the radial direction, ϖ is the dummy variable for the integration along the radius. The formulation shows that the exit over-pressure is related to the material derivative of the radial velocity on the exit, which indicates that a non-zero radial velocity is required for any non-negligible over-pressure on the nozzle exit. Therefore, we present the radial velocity $u_r(r)$ distributions along the exit radius at time instant $t = 0.5T_D$ for the three nozzles considered here in

Fig. 3.28, where the corresponding result from the orifice scenario is also presented for comparison. The converging nozzles produce negative radial velocity $u_r < 0$ on the exit due to geometric effect. Likewise, the orifice jetting also experience negative radial velocity because as body shrinks, the orifice forms a conical nozzle, through which the flow is ejected with converging streamlines.

Figure 3.27 also presents the time evolution of the analytically obtained over-pressure obtained using Eqn. (3.30). It is seen that the analytical model can qualitatively predict the tendency since the two results are consistent in phase, especially during the second peak. The quantitative inconsistency might be because viscosity is ignored in the analytical model. Figure 3.27 shows that more converging nozzles (with shorter l) result in higher exit pressure, which then translates to higher F_T^σ as shown in Fig. 3.26d.

Notwithstanding its quantitative accuracy, the analytical model is still useful for physical insights. Let p_u and p_c respectively denote the integration of u_r unsteady acceleration and convective acceleration ($p_u = \int_r^{R_\infty} \frac{\partial u_r}{\partial t} d\varpi$, $p_c = \int_r^{R_\infty} \mathbf{u} \cdot \nabla u_r d\varpi$), then the analytical over-pressure (Eq. (3.30)) can be expressed as $p_u + p_c$. Figure 3.29a displays the time histories of p_c and p_u for a representative case with $r = 0.2R'$, $l = 0.6D$, and $\theta = -14.5°$. It shows that the exit over-pressure is predominantly contributed from the convective acceleration related p_c. Increasing the nozzle convergence (achieved through decreasing l) leads to larger radial velocity u_r, as displayed in Fig. 3.28. This is accompanied by the augmentation of spatial derivative of u_r along the streamline direction (the convective acceleration) on the exit, leading to p_c enhancement as shown in Fig. 3.29b, which eventually translates to higher F_T^σ (see Fig. 3.26d). In addition, $p_c(r)$ can be rewritten as $\int_r^{R_\infty} u_x \frac{\partial u_r}{\partial x} d\varpi - 0.5u_r^2$, in which the second term is much smaller than the integration term according to our simulations. Since $\frac{\partial u_r}{\partial x} > 0$ is satisfied for converging nozzles, this new expression explains the reason why F_T^p (or alternatively F_T^σ) is more or less proportional to the jet speed, hereby forming the second peak with the prescribed jet speed profile.

The mechanism for the first peak of F_T^σ will be illustrated by using tubular nozzles as an

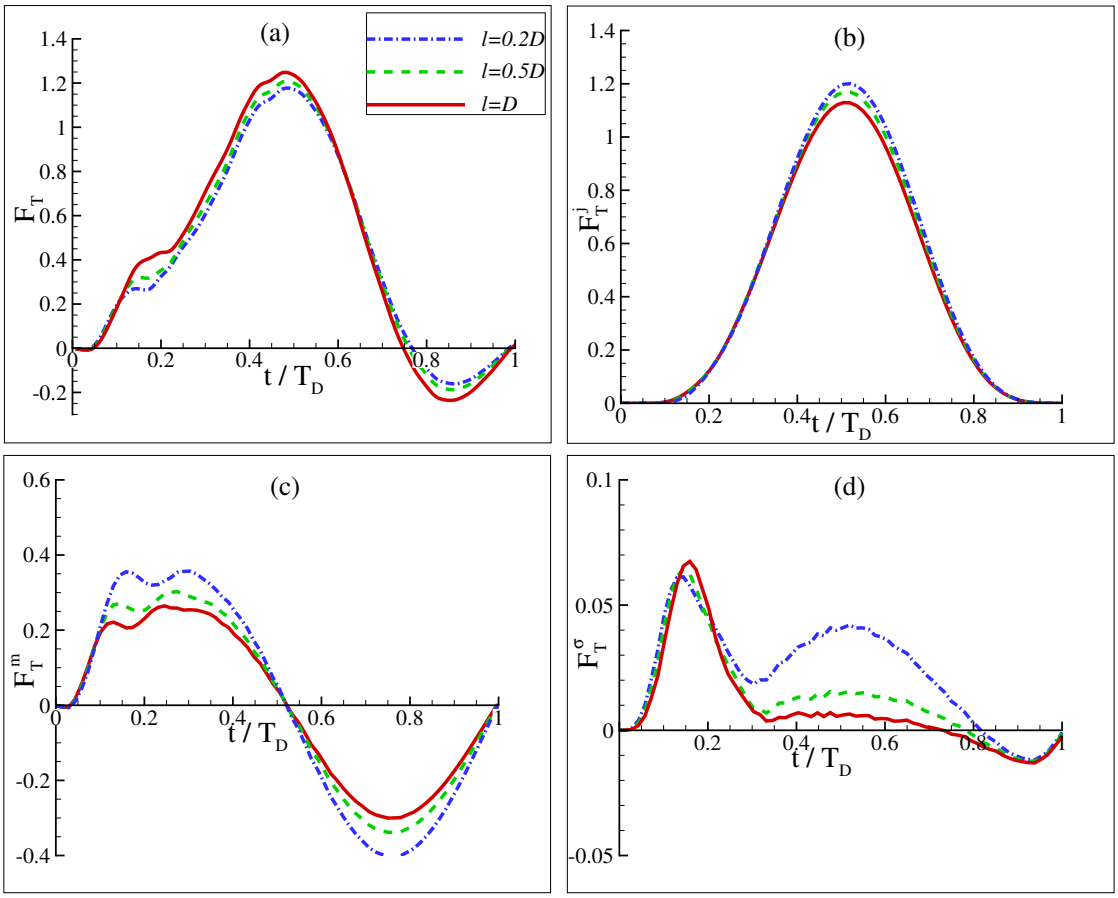

Figure 3.30: Same as Fig. 3.26 except that tubular nozzles are used.

example since in that scenario the twin-peak phenomenon becomes more pronounced.

b) Tubular nozzles

We then examine three tubular nozzles ($\theta = 0$ so that the nozzle exit diameter is a constant, *i.e.* $D' = D$) with different contour lengths $l = 0.2D, 0.5D, D$. Not surprisingly, Fig. 3.30a confirms the consistency of the overall thrust F_T in these three cases. The thrust components F_T^j and F_T^m have similar time histories as those with the converging nozzles (see Figs. 3.30b,c). Indeed, tubular nozzles may share some characteristics with converging nozzles since in both cases converging streamlines are generated at the orifice, which may not be fully flattened in the nozzle when l is not sufficiently long. As a result, with tubular nozzles the other thrust component F_T^σ also behaves

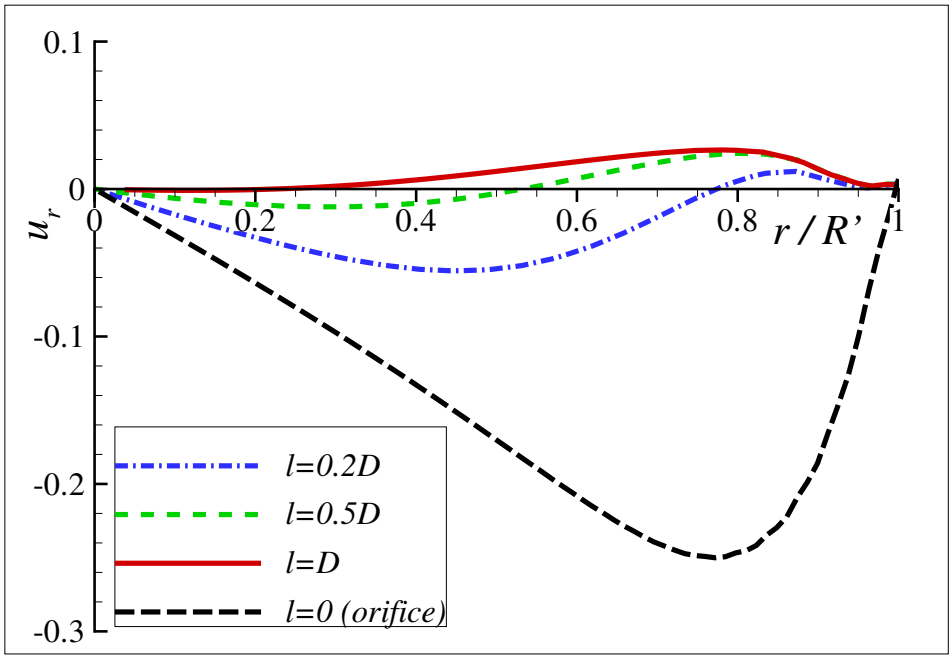

Figure 3.31: Comparison of radial velocity (normalized by$\tilde{V}_j$) profiles on the exit of tubular nozzles and orifice, $t = 0.5T_D$

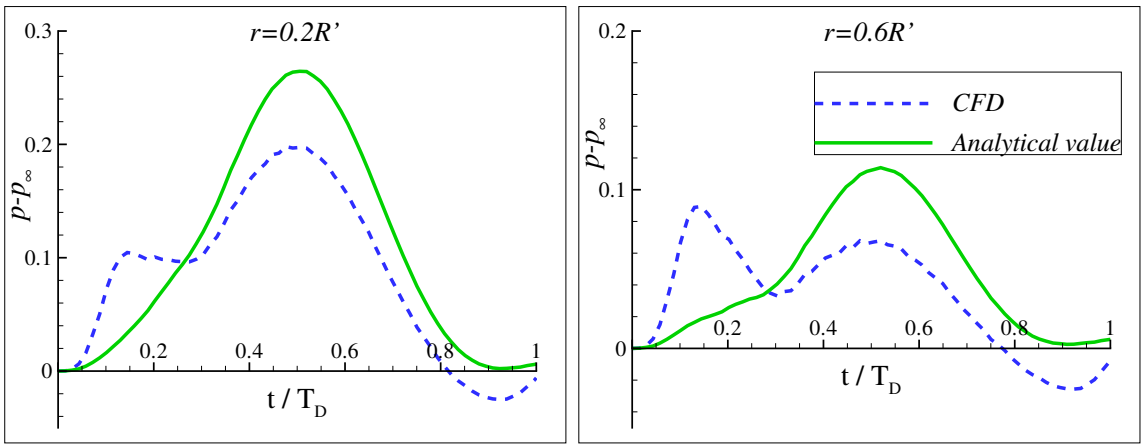

Figure 3.32: Comparisons between the numerically obtained over-pressures and the analytical values at the monitoring locations. The nozzle is tubular with $l = 0.2D$.

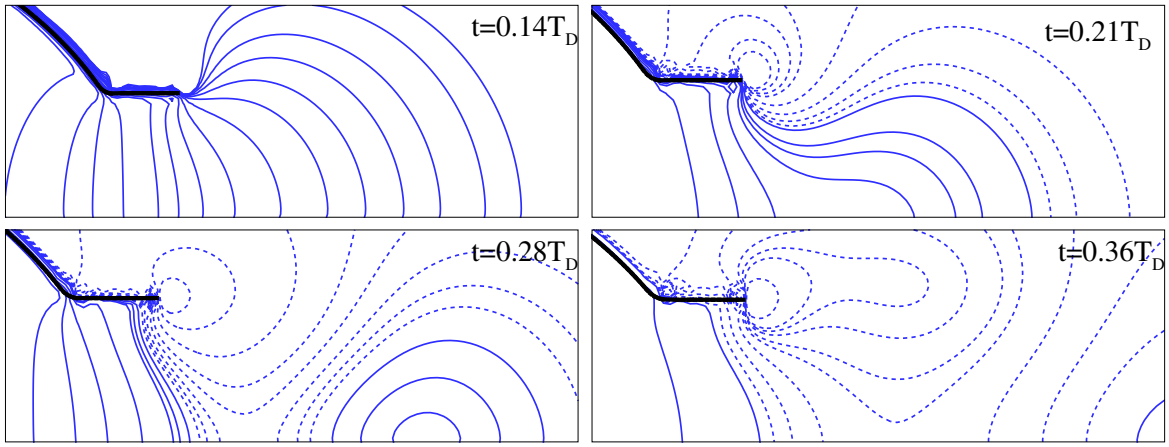

Figure 3.33: The evolution of the pressure field for the tubular nozzle with $l = 0.2D$, The solid lines represent the positive pressure contours and the dashed lines indicate the negative pressure contours.

similar to that of the converging nozzles (both have twin peaks) as shown in Fig. 3.30d.

Figure 3.31 displays the radial velocity $u_r(r)$ at time instant $t = 0.5T_D$ with the three tubular nozzles. As expected, the radial velocity is significantly reduced after applying tubular nozzles to the orifice. For this reason, small over-pressure is created on the nozzle exit and subsequently F_T^σ is also small, as shown in Fig. 3.30d. As a result, the second peak is significantly diminished due to the reduced radial velocity, making the twin-peak feature in F_T^σ more pronounced. Figure 3.32 presents the comparison between the numerically obtained over-pressure and the analytical predictions at the two monitoring locations for a sample case with $l = 0.2D$. Similar to the case with converging nozzles, the analytical model is not able to predict the first peak.

A likely source of the first peak in F_T^σ is the generation and evolution of the leading vortex ring. When the jetting is initiated, a single vortex ring is generated and starts to grow in the wake very close to the exit plane. The pressure on the exit is thus influenced by the coupled effect of the jet flow and the wake flow associated with the vortex ring. In Fig. 3.33, we exhibit the evolution of the pressure field near the nozzle exit during the initial stage ($t < 0.36T_D$). It shows that the exit is initially surrounded by positive pressure (*e.g.* $t = 0.14T_D$). When it reaches $t = 0.21T_D$, there

appears a negative pressure region close to the nozzle boundary layer, corresponding to the vortex ring generation (negative pressure has been found to coincide with the cores of vortex rings in experiments [64]). Afterwards the negative pressure region grows gradually and eventually almost fills the exit plane. When this vortex-induced negative pressure steps in, the exit pressure will decline, a phenomenon related to the reduced F_T^σ in $0.2T_D < t < 0.3T_D$ in Fig. 3.30d. Similar discoveries have been reported by Gao *et al.* [65]. As the vortex convects downstream, its effect on the exit pressure will be diminished and the radial velocity will become the dominant factor.

Besides the vortex-induced negative pressure, the jet acceleration may also play a role in the formation of the first peak. According to control volume analysis (see Appendix D), to certain extent F_T^σ is dependent on the jet acceleration, particularly during the initial stage when the leading vortex ring is near the exit plane. The time history of jet acceleration for cosine profile undergoes the first peak at $t \approx 0.2T_D$, which implies that the acceleration peak may be another source of the first peak of F_T^σ, which occurs near that instant.

c) Diverging nozzles

For diverging nozzles ($\theta > 0$), three configurations, $(l, \theta) = (0.4D, 22^\circ)$,$(0.6D, 14.5^\circ)$, and $(D, 8.6^\circ)$ are chosen with the nozzle exit set to be constant ($D' = 1.3D$). Figure 3.34 presents the time histories of F_T and its three components F_T^j, F_T^m, F_T^σ. Like the previous cases with converging and tubular nozzles, slight variations of these components among the three cases fail to cause significant difference in F_T. Unlike the converging and tubular nozzles, a diverging nozzle produces positive radial flow speed (see Fig. 3.35), which creates a negative trough instead of the second peak as displayed in Fig. 3.34d. For this reason in diverging nozzles $\overline{F_T^\sigma}$ contributes negatively to the thrust.

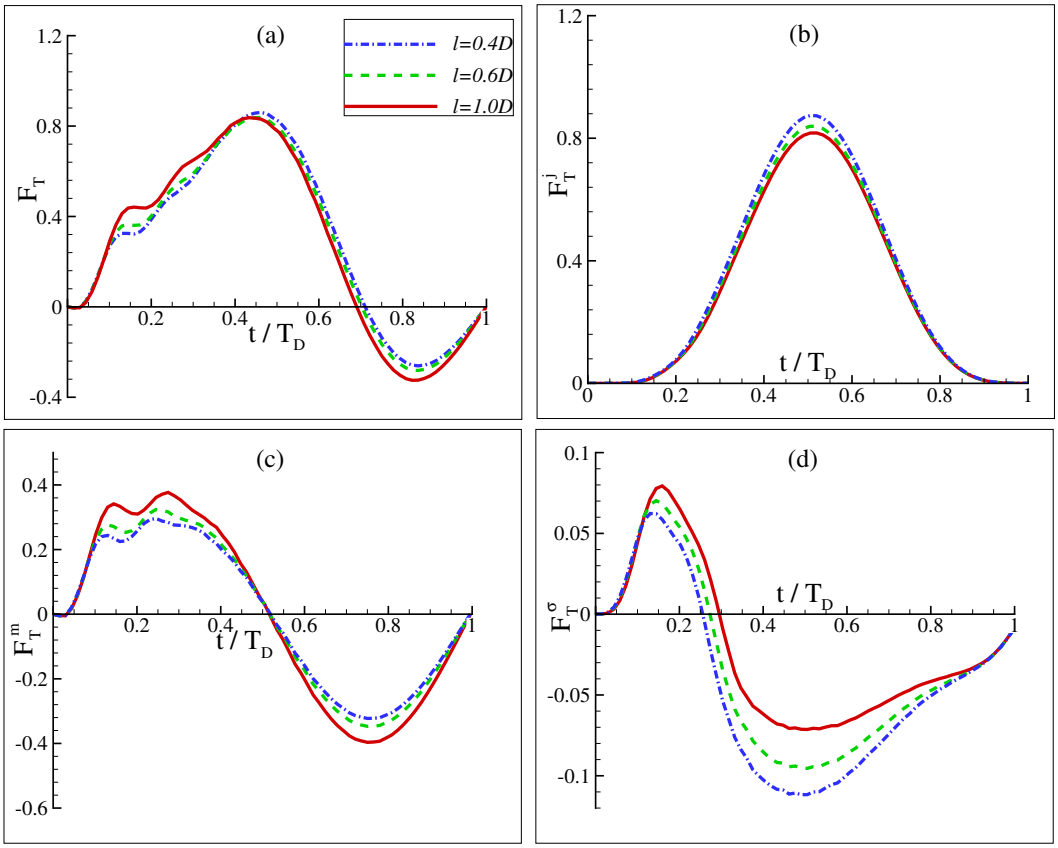

Figure 3.34: Same as Fig. 3.26 except that diverging nozzles are used.

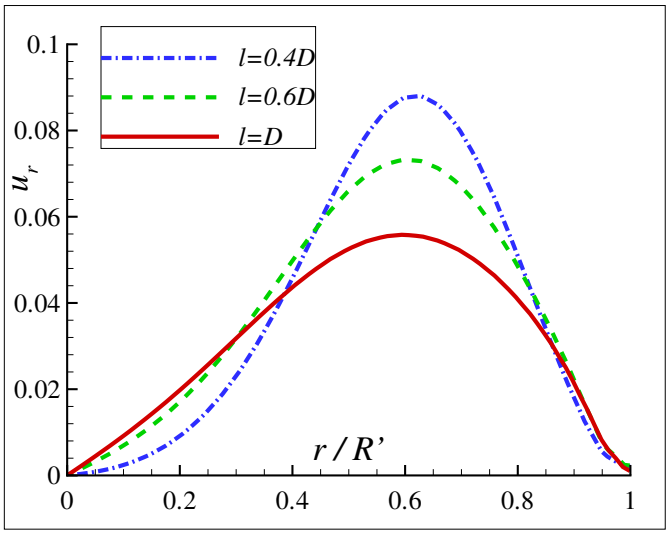

Figure 3.35: Comparison of radial velocity (normalized by $\tilde{V}_j$) profiles on the exit of diverging nozzles, $t = 0.5T_D$.

3.7.2 Cost of impulse

Figure 3.36a plots the time-averaged power expenditure $\overline{P}$ (normalized by $\overline{P_0}$) as function of θ and l. It shows that when $\theta \leqslant 0$, $\overline{P} > \overline{P_0}$ so that it takes additional energy to expel fluid through tubular or converging nozzles. For diverging nozzles, however, it depends on the inclination angle θ. Specifically, additional power expenditure is still needed when $\theta < 20°$. Otherwise, when a sufficiently diverging nozzle (*e.g.* $\theta > 20°$) is installed, $\overline{P}$ is close to $\overline{P_0}$. Figure 3.36b presents the dependencies of the normalized cost of impulse COI/COI_0 upon θ and l. Note that higher cost of impulse corresponds to lower efficiency. We find that the shorter the nozzle is, the more efficient the system will be. In fact, the orifice jetting in which $l = 0$ turns out to be the most efficient. Moreover, It is found that the propulsive efficiency tends to be higher as the nozzle gets more diverged till it reaches a threshold (approximately $\theta = 20°$), beyond which the efficiency becomes insensitive to the inclination angle θ.

In summary, the geometry of nozzles affects the propulsion performance in terms of thrust generation and efficiency. Specifically, after adding diverging nozzles, both thrust and efficiency are decreased. The usage of tubular nozzles tends to reduce the efficiency while has negligible effect on thrust generation. The converging nozzles, however, will improve the thrust at the cost of efficiency.

3.8 Conclusions

Fluid dynamics of a squid-inspired jet propulsion system in low Reynolds number have been numerically investigated by using the immersed-boundary method. The idealized axisymmetric system includes a pressure chamber enclosed within a shell with zero thickness and a circular nozzle. The body deformations (inflation and deflation) are prescribed to achieve three different jet speed profiles with the nozzle size fixed. Three swimming modes, namely the escaping mode

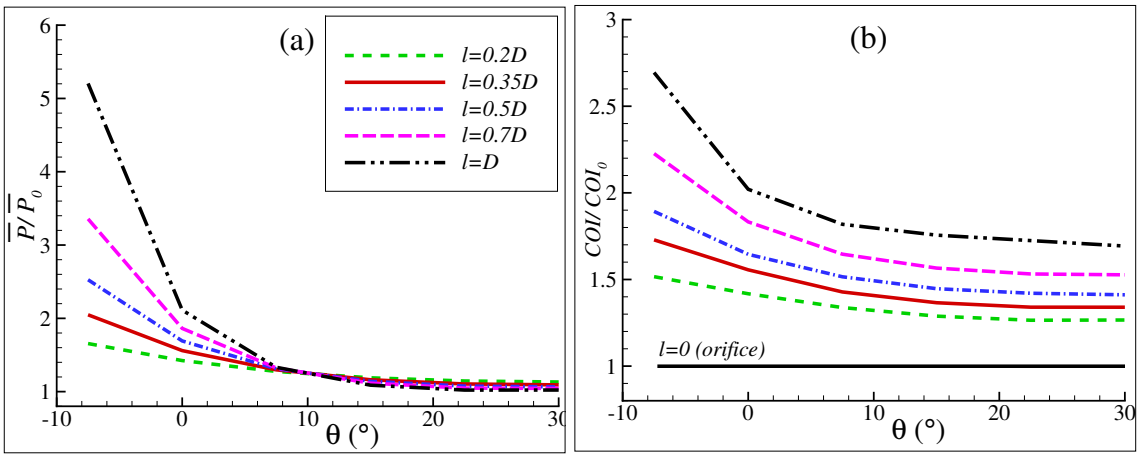

Figure 3.36: (a) Normalized power expenditure $\overline{P}/\overline{P_0}$ as functions of θ and l, (b) normalized cost of impulse COI/COI_0 as functions of θ and l.

through body deflation, recovery mode through inflation and long-distance locomotion via cyclic deformation are investigated.

First, we found that in low Reynolds number regime, the vortex ring does not pinch off completely from its trailing jet throughout the jetting process, neither are there any secondary vortex rings formed in the trailing flow. It suggests that the pulsed jetting in low Reynolds number is a smooth vortex ring generation process, which is different from cases in high Reynolds numbers.

In order to predict the thrust and thrust-based propulsive efficiency of the system in long-distance swimming mode within free stream u_0, a thrust-drag decoupling strategy designed specifically for this problem is proposed based on control volume analysis. The jet-related thrust in our definition can be further decomposed into three distinct components, the jet flux force F_j, the exit fluid stress F_σ and the flow momentum force inside the body F_m. F_j and F_σ are closely associated with jet speed, whereas F_m is proportional to jet acceleration. The feasibility and accuracy of the thrust-drag decoupling method are demonstrated through three special scenarios, rigid-body dynamics and single deflation or inflation dynamics without incoming flow. The thrust-drag decoupling method enables the calculation of jet-related thrust, which is then used to define the propulsive efficiency of repeated inflation-deflation cycles in a uniform free stream.

Through systematic simulations, we found that the whole-cycle propulsive performance depended mostly on the incoming flow Reynolds number Re and the jet flow Reynolds number Re_j. For relatively low Re_j (*e.g.* 20), the time-averaged thrust varies considerably within the range of Re we consider. This variation mainly results from the nozzle pressure force F_p, which is sensitive to wake characteristics. It is shown that at low Re_j when the jet is relatively weak, the nozzle pressure can be easily affected by the negative pressure region induced by the vorticity shed from the outer side of the shell. However, for relatively high Re_j in which high-speed jet is discharged, the body-shed vortex ring becomes too weak to affect the jet flow or the nozzle pressure. In these cases the effect of Re on thrust generation is negligible. Our results suggests that the time-averaged thrust over a full cycle is linearly dependent on the jet speed when $Re_j > 100$.

The propulsive efficiency at the steady-swimming state (*i.e.* the state when the time-averaged net force on the body is zero) is then calculated at various values of Re_j. The results show that the efficiency increases as Re_j goes up. Finally, the effect of the maximum stroke ratio has also been examined. It is demonstrated that within the current range of Re_j, and with the prescribed sinusoidal jet speed profile, the maximum stroke ratio does not directly affect thrust generation.

Systematic computations were conducted to simulate the pulsed jetting of the system with different nozzles added. After installing nozzles, there could be considerable thrust enhancement on the deformable body (without the nozzle), mainly attributed to augmentation of the orifice fluid stress. For the performance of the whole system including the deformable body and the nozzle, the thrust production is mostly from the jet flux term at the nozzle exit. The other two components account for relatively small percentage of the overall thrust. As a result, variations in these two components associated with different nozzles do not affect the overall thrust significantly. Therefore the thrust generation of the whole system depends mostly on the nozzle exit size. For example, tubular nozzles generate thrust close to the one by the system without nozzle. Converging and diverging nozzles result in increased and declined thrust production, respectively. The propulsive

efficiency of the whole system was also examined. It is shown that the usage of nozzles makes the jet propulsion less efficient.

The current study concentrates on a simple sinusoidal jet profile, yet we are aware that performance of the system can be highly sensitive to the detailed time history of the jet, an effect beyond the reach of methods stemming from the concept of Froude efficiency since they are based on time-averaged values. On the other hand, the method proposed in this study is fully capable of studying cases with different jet profiles. Future studies will be conducted to understand how this factor will affect the efficiency of the system.

The thrust-drag decoupling strategy proposed here is a novel method to compute thrust force and the corresponding propulsive efficiency of squid-like underwater locomotion. It can be easily extended to other locomotion problems involving pulsed-jet propulsion, *e.g.* locomotion of other cephalopods such as octopuses and cuttlefish, salps, or jellyfish.

This chapter, in part, is a reprint of the material as it appears in the following papers.

- Xiaobo Bi and Qiang Zhu, "Pulsed-Jet Propulsion via Shape Deformation of an Axisymmetric Swimmer", *Physics of Fluids*, 32: 081902,2020.

- Xiaobo Bi, Qiang Zhu, "Efficiency of Pulsed-Jet Propulsion via Thrust-Drag Decoupling",*Physics of Fluids*, 33: 071902,2021.

- Xiaobo Bi, Qiang Zhu, "Effect of Nozzle Geometry on the Performance of Pulsed-Jet Propulsion", under review.

The dissertation author is the primary investigator and author of these papers.

Chapter 4

Three Dimensional Potential-Flow Model of Squid-Inspired Locomotion with Intermittent Bursts

In this chapter, we will investigate the squid-inspired locomotion at high Reynolds number regime by using the potential flow theory. We hereby propose a three dimensional propulsion system that is capable of long-distance locomotion through repeated body shape change. A numerical model using the boundary element method is developed to computationally study the swimming process and the dynamic characteristics of this system. In this particular work the deformation of the body itself will be prescribed, whereas the forward motion will be simulated by solving the fluid-structure interaction problem.

4.1 Description of the physical problem

Similar to the axisymmetric swimmer in Chapter 3, the system we consider is axisymmetric (the axis of symmetry is shown as a dash-dotted line), as displayed in Fig. 4.1a. The diameter

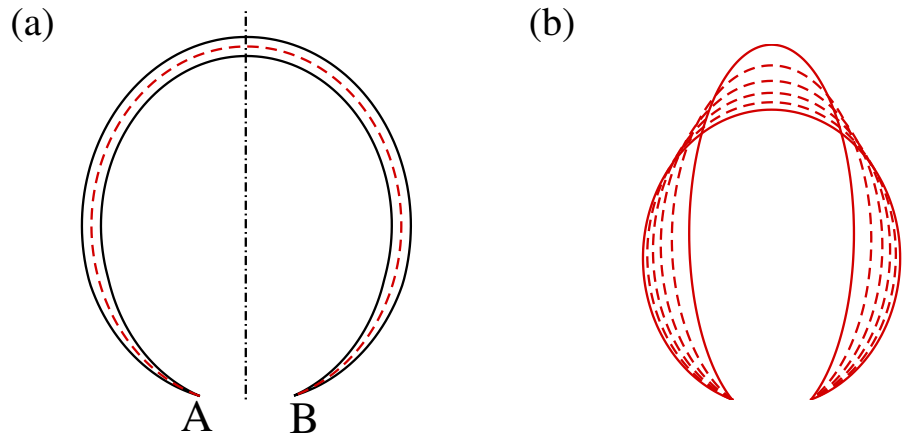

Figure 4.1: (a) Geometry and (b) deformation of the centerline of the wall (the starting and ending positions are shown in solid lines).

of the opening is $\overline{AB}$. The centerline of the wall (the dashed line) is part of an ellipse with an eccentricity of e. The contour length from A to B along the centerline is L (see the Appendix A for the determination of these curves). The thickness of the wall is much less than L (in the following simulations its initial value is chosen to be around $0.04L$) with tapering near the nozzle to create a sharp trailing edge. The density of the wall is assumed to be the same as the surrounding fluid so that the body is neutrally buoyant.

The body deformation is achieved by varying the value of e while keeping both D and L unchanged (Fig. 4.1b). In the deformation process we adjust the wall thickness so that the overall volume of the solid body (not including the fluid inside it) remains a constant to avoid any change in the mass of the body itself. Furthermore, the deformation shown in Fig. 4.1 results in a (albeit small) shift in the position of the center of gravity of the solid body. In simulations this drifting motion due to deforming body is removed so that without the hydrodynamic loading the center of gravity of the body itself remains at its initial position.

Unlike the swimmer in Chapter 3, the inlet of our model is in the upstream side so that the swimmer is able to move forward for a certain distance during the recovery phase. Meanwhile

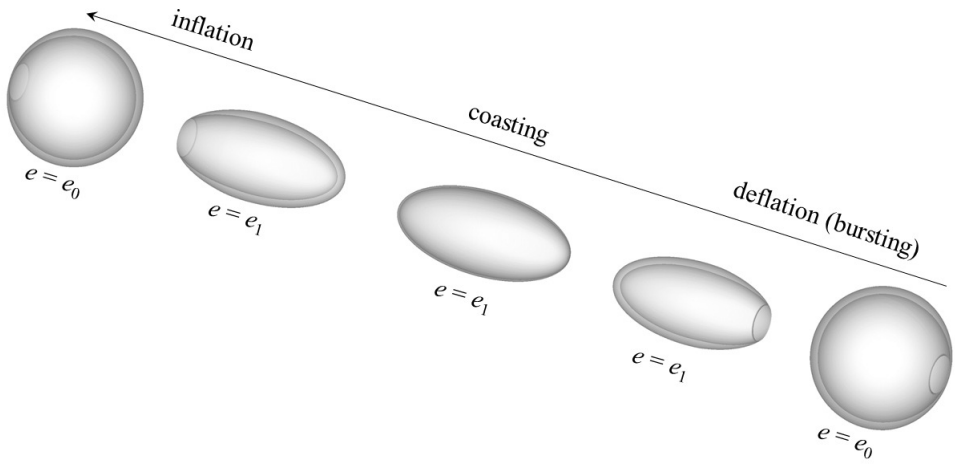

Figure 4.2: A complete deflation-inflation cycle during cephalopod-inspired swimming.

a coasting phase follows behind the deflation phase to make the kinetic energy of the body be mostly released before initializing the inflation process. In Fig. 4.2 we illustrate a complete deflation-inflation cycle, including a deflation period, a coasting period, and an inflation period. The durations of these three periods are T_D, T_C, and T_I. The corresponding traveling distances are L_D, L_C, and L_I, respectively. During deflation the exit is open and the compression chamber is shrunk by increasing the eccentricity of the body from e_0 to e_1. This is followed by the coasting period, during which both the inlet and the exit are closed so that the vehicle is depicted as a rigid spheroid with eccentricity e_1. The inflation phase starts when the residue speed is negligibly small. In this phase the eccentricity increases from e_1 to e_0. In the inflation phase the body geometry and deformation is described the same way as the one shown in Fig. 4.1, although the opening (*i.e.* the inlet) is in the upstream side and its size is tagged D_I to distinguish it from the size of the orifice D. In the following simulations, we consider a complete cycle with three periods, deflation ($0 \leq t \leq T_D$), coasting ($T_D \leq t \leq T_D + T_C$) and inflation ($T_D + T_C \leq t \leq T_D + T_C + T_I$).

In the deflation period the eccentricity e increases linearly with time from its initial value e_0 to the end value e_1 as $e = e(t) = e_0 + (e_1 - e_0)t/T_D$. In the inflation period, on the other hand,

linearly varying e causes numerical issues associated with sudden changes at the beginning of the deformation. Thus a smooth starting curve $e = e(t) = e_1 + (e_0 - e_1)\left[(t - T_D - T_C)/T_I\right]^3$ is adopted. The initial speeds in the deflation and the inflation periods are both assumed to be zero.

4.2 Mathematical Model and Numerical Implementation

4.2.1 Mathematical formulations

The problem is described within a Cartesian coordinate system (x, y, z), in which x coincides with the axis of symmetry and the body swims in the $-x$ direction. In the high Reynolds number regime we employ the potential flow assumption and define a flow potential Φ to describe the flow fields both inside and outside of the body. In addition, the wake behind the body is depicted as a zero-thickness shear layer originated from the sharp trailing edge at the nozzle.

The potential Φ satisfies the Laplace equation $\nabla^2\Phi = 0$ inside the fluidic domain. On the interface between the fluid and the solid body we impose the no-flux condition so that $\partial\Phi/\partial\mathbf{n} = \mathbf{V}_b \cdot \mathbf{n}$, where $\mathbf{n}$ is the unit normal vector pointing into the body and $\mathbf{V}_b$ is the velocity of the body.

By invoking Bernoulli's equation, the distribution of pressure p in the fluid is given as

$$p(\mathbf{x}, t) = -\rho\left[\frac{\partial\Phi}{\partial t} - \frac{1}{2}\nabla\Phi\cdot\nabla\Phi\right], \tag{4.1}$$

where $\mathbf{x} = (x, y, z)$. ρ is the density of the fluid. The fluid forcing on the body $\mathbf{F}$ and instantaneous power expenditure P of the body are then calculated as

$$\mathbf{F}(t) = \iint_{S_b} p\mathbf{n}ds', \tag{4.2}$$

and

$$P(t) = \iint_{S_b} p\mathbf{V}_b \cdot \mathbf{n} ds', \tag{4.3}$$

where S_b stands for surface of the body (including both the inner and the outer surfaces).

The displacement of the body is depicted by x_{bc} and x_c, the x locations of the centroids of the solid body (without the fluid inside) and the body with inside fluid, respectively. Among them, x_{bc} is obtained by solving the dynamic equation

$$m_b \ddot{x}_{bc} = F_x, \tag{4.4}$$

where m_b is the mass of the solid body and F_x is the $x-$component of $\mathbf{F}$. x_c is then determined through geometric relations. The corresponding speeds of the two centroids are calculated as $V_{bc} = -\dot{x}_{bc}$ and $V_c = -\dot{x}_c$ (the minus signs reflect the fact that the actual motion is in the $-x$ direction), respectively.

To study the energetics of the system, we define the energy transferred from the body to the flow field from the beginning of the (deflation or inflation) deformation to time t as E. We have

$$E(t) = \int_0^t P(t')dt'. \tag{4.5}$$

During the deflation period, the instantaneous energy efficiency is defined as

$$\eta(t) = \frac{1}{2} \frac{[m_b + m_f(t)]\, V_c^2(t)}{E(t)}, \tag{4.6}$$

where m_f is the mass of the fluid remaining inside the body. The quantity η measures how much of the energy spent by the body is transferred to the kinetic energy of the system (including the body and the fluid inside it). In this definition we assume the inner fluid moves together with the body and its motion relative to the body is not considered.

The performance of the system in the deflation phase is measured with the following quantities: (1) the normalized speed $V'_D = V_{bc}(T_D)T_D/L$ after the deflation; (2) the normalized drifting distance after the deflation $L'_D = \left[-x_{bc}(T_D) + x_{bc}(0)\right]/L$; (3) the normalized energy expenditure $E'_D = E_D T_D^2/(\rho L^5)$ (where $E_D = \int_0^{T_D} P(t')dt'$), and (4) the overall deflation efficiency $\eta_{_D} = \eta(T_D)$. The performance in the inflation phase is represented by the normalized energy expenditure $E'_I = E_I T_I^2/(\rho L^5)$ ($E_I = \int_{T_D+T_c}^{T_D+T_C+T_I} P(t')dt'$) and the distance gained during inflation defined as $L'_I = \left[-x_{bc}(T_D + T_C + T_I) + x_{bc}(T_D + T_C)\right]/L$.

4.2.2 Numerical method

To numerically solve the mathematical problem defined above, the flow potential Φ is first decomposed into two parts, ϕ_b and ϕ_w. ϕ_b represents the contribution from the solid body, and ϕ_w is the influence potential of the wake (*i.e.* the shear layer). These two potentials are solved separately.

The body potential ϕ_b satisfies the boundary-integral equations, which suggests that the solid surface can be replaced by distributions of singularities (*e.g.* sources) to satisfy the no-flux condition. This condition leads to an integral equation for the strength of these singularities. We employ the boundary element method to solve this problem. In this approach, quadruple elements are distributed on the body surface (Fig. 4.3). Each element contains a constant distribution of sources in it. The no-flux condition is then reformulated as a system of linear equations, which can be solved numerically to find the source distribution on the body surface so that ϕ_b at that instant is determined subsequently.

The wake is mathematically represented by distributions of dipole on a zero-thickness flexible sheet. A similar boundary element approach is applied, in which the wake sheet is segmented into quadruple elements. Within each element, the dipole strength is approximated as a constant. It can be proven that such an element is equivalent to a small vortex ring around its

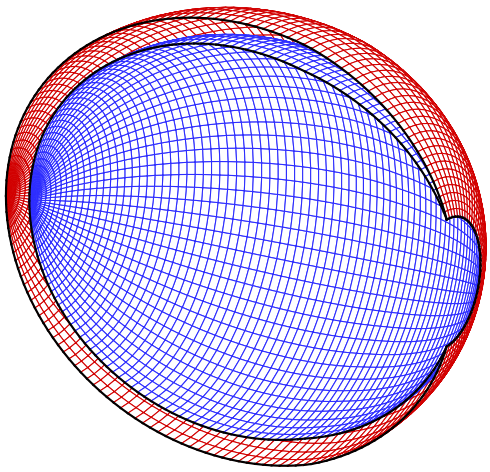

Figure 4.3: Boundary elements on the inner (blue) and outer (red) surfaces of the body. For clarity only half of the body is shown.

boundary. At each time step, a new row of wake elements are generated from the trailing edge at the nozzle, where their strengthes are determined *via* the Kutta condition. Meanwhile wake elements shed earlier are convected into the wake under the combined effect of induced velocity of the body and the self-induced velocity of the wake. The strengthes of these wake elements remain unchanged due to the lack of dissipation effects. The wake potential ϕ_w is evaluated by summarizing contributions from all of these wake elements.

The boundary-element problem for ϕ_b and the determination of wake potential ϕ_w are essentially coupled. In our model the decoupling is conducted in time domain in a staggered manner. The wake sheet is physically unstable so that a desingularization technique is applied [66]. This method not only stabilizes the wake within the duration of the simulation, but also spread the wake vorticity into a finite region so that it can be visualized (please refer to Fig. 4.8).

After the flow potential Φ is obtained with this method, the pressure field, the fluid dynamic force on the body, and the power expenditure are calculated with Eqns. (4.1) to (4.3). The location and velocity of the body is then updated through Eqn. (4.4) with a forward Euler algorithm. In this

particular problem the added mass of the body is much larger than its own mass, leading to the well-known added-mass-related instability. To avoid this issue, a special treatment is needed, in which the contribution from added mass is removed from both sides of Eqn. (4.4) [67].

Details of this method have been included in our previous papers [66, 67]. In these studies the validity and accuracy of the model have been tested extensively through convergence tests as well as comparisons with experimental, numerical, and theoretical results in the literature. For example, we have compared experimental measurements from a robotic fish and our numerical predictions [66]. The model has also been compared with theoretical data about a flapping foil near the free surface [68]. The fluid-structure interaction part has been validated in a comparison with experiments of flexible flapping plates [67]. In all of these examinations predictions of our model match well with the benchmark data.

4.3 Results

We hereby apply the boundary element model to numerically study the locomotion performance of the cephalopod-inspired system described in §4.1. All the results in this section will be normalized by the contour length L, the fluid/solid density ρ, and the deformation time T_D (in the deflation phase) or T_I (in the inflation phase).

A convergence test has been conducted to examine the sensitivity of the results with respect to mesh density and time step. In this test we consider the deflation phase and calculate the normalized speed V_D' right after the deflation. As shown in Table 4.1, the results converge with both mesh density and time step. In the following simulations we will use 12800 elements. The time step Δt is chosen to be $T_D/100$. Based on the convergence test the numerical error is expected to be smaller than 3%. Unless otherwise specified, the eccentricity of the swollen state of the body e_0 is set to be 0, the one of the slender state (e_1) is 0.9.

Table 4.1: Convergence of the normalized peak speed V_D' with respect to the number of elements and time step. $e_0 = 0$, $e_1 = 0.9$, $D/L = 0.1$.

$T_D/\Delta t \setminus N_e$	4800	6400	12800
50	1.116	0.999	1.020
100	1.177	1.026	1.058
200	1.225	1.039	1.032

4.3.1 Deflation period ($0 \leq t \leq T_D$)

Time histories during the deformation

In our simulations within the deformation time $0 \leq t \leq T_D$ the eccentricity of the body increases from e_0 to e_1 following the path defined in §4.1. Under this condition the variation of the internal volume $\forall$ over time is shown in Fig. 4.4. In the same figure we plot the jet speed V_j at the exit relative to the exit plane itself. It is seen that through this deformation a peak jet speed of 2.1 L/T_D is achieved at $t = T_D$. This will be a key mechanism of thrust generation.

In Fig. 4.5 we plot the time histories of the overall thrust F_T and the contribution from added-mass effect, $F_a = -\dot{m}_a V_{bc}$. According to the result F_T remains positive and increases quickly till the end of the deflation period, so that the body accelerate over the whole duration of deflation. Meanwhile, the portion in F_T attributed to the added mass effect also increases with time. For example, at $t = T_D/2$ about 53% of the thrust is due to F_a. At the end of the deflation period ($t = T_D$), one the other hand, F_a accounts for 71% of the thrust. This is explained by the fact that F_a is proportional to speed of the body, which increases monotonically during the deflation period (Fig. 4.6).

Accompanying the positive thrust, the speed of the body increases until it reaches the peak value at the end of the deflation phase. In this particular case (with $e_0 = 0$, $e_1 = 0.9$ and $D/L = 0.1$) the peak speed is $1.058L/T_D$. If we choose L/π as the characteristic body length of the system, with $T_D = 0.33$ s it is able to reach 10 body lengths per second, the recorded speed of larger squids [15]. To reach the speed of smaller squids (25 body lengths per second [14]) T_D has to

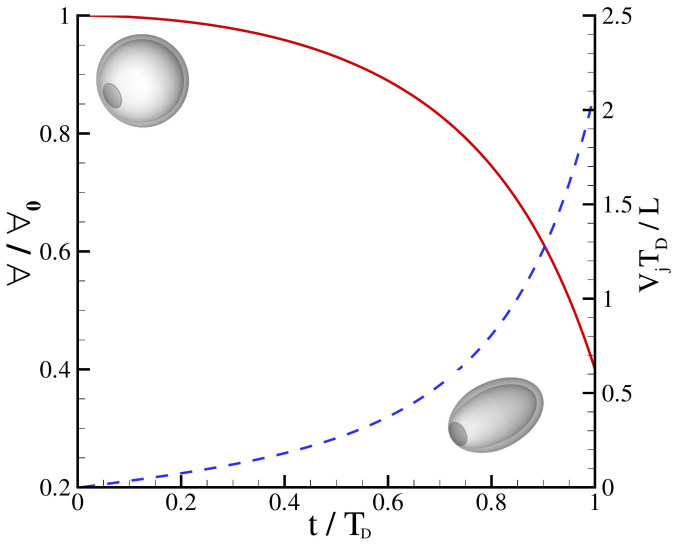

Figure 4.4: Time histories of the internal volume $\forall$ of the system normalized by it initial value $\forall_0$ (solid line) and the average speed of the jet V_j related to the nozzle (dashed line) during the deformation. The insets show the shapes of the system before and after the deformation.

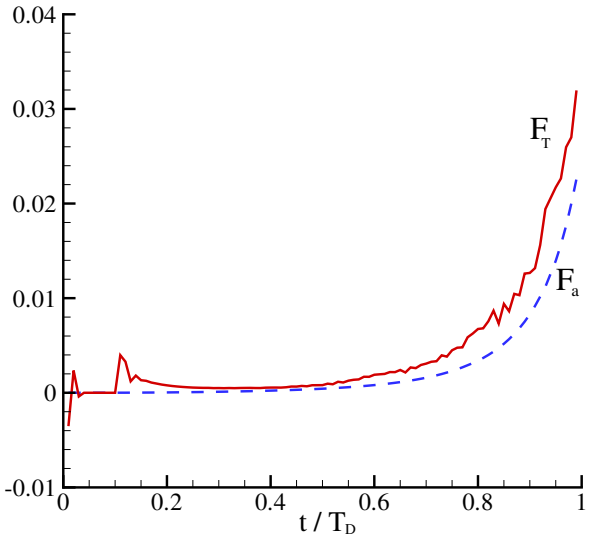

Figure 4.5: Time histories of the total thrust force F_T on the body (solid line) and the contribution of the added mass effect to thrust F_a. Both of the forces are normalized by $\rho L^4/T_D^2$.

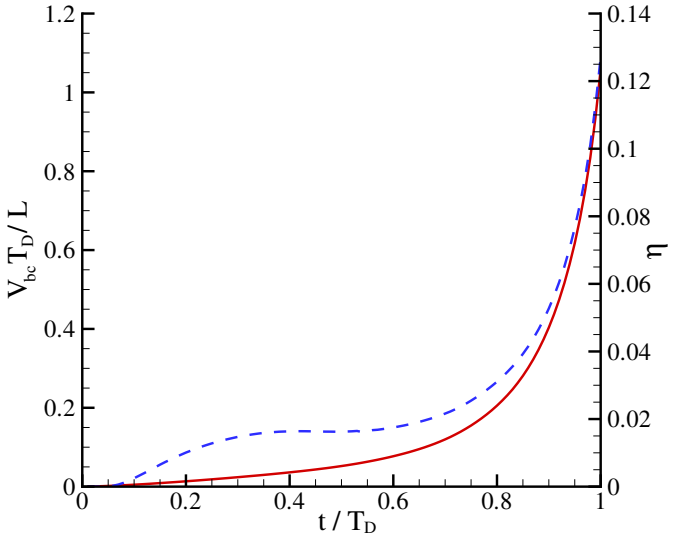

Figure 4.6: Time histories of the speed of the centroid of the body V_{bc} (solid line) and the instantaneous energy efficiency η (dashed line) during deflation.

be 0.13 s. The corresponding energy efficiency approaches 0.13 so that at that moment about 13% of the energy spent by the body to push the fluid out is transferred to its kinetic energy (including the kinetic energy of the fluid remaining inside) in forward motion.

Characteristics of the wake

In the boundary element approach the vorticity distribution in the wake is assumed to be concentrated on zero-thickness layers. New wake elements are generated from the nozzle at every time step so that the wake sheet grows as it propagates downstream. As mentioned in the methodology part, in our method a desingularization technique is employed so that this wake sheet remains stable within the duration of a deformation period (*i.e.* $t \leq T_D$).

Figure 4.7 shows the evolution of the wake sheet during the simulation. It is clear that under its self-induced velocity it rolls up into the shape of a torus behind the body. To visualize the actual vorticity wake, in Fig. 4.8 the iso-surface of vorticity distribution in the wake is plotted (the

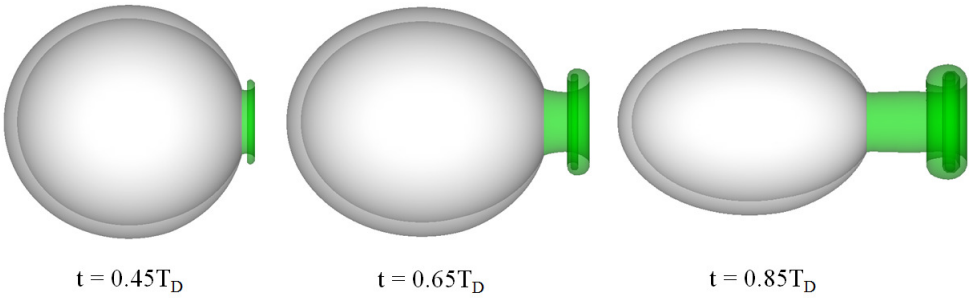

Figure 4.7: Evolution of the wake elements during the deflation deformation. $D/L = 0.1$.

Table 4.2: Formation number Γ at different values of e_0 and D/L. e_1=0.9.

$e_0 \setminus D/L$	0.06	0.08	0.10	0.12	0.14	0.16	0.18
0.0	57.42	25.4	13.6	8.1	5.3	3.6	2.6
0.8	22.3	9.8	5.2	3.1	2.0	1.4	1.0

desingularization technique allows vorticity to be spread into the flow field rather than concentrated on the wake sheet). The flow pattern is recognized as a single circular vortex ring.

Parametric effects

As clearly demonstrated in Figs. 4.7 and 4.8, a circular vortex ring is generated in the wake by the jet flow from the nozzle. The formation of this vortex ring will thus play a role in the dynamics of the system. This is reminiscent of the existence of a universal scaling law that governs formation of such vortex rings as discussed in §3.4.2. It was proposed that the critical formation number is related to optimal propulsion performance in pulsed thrust mechanisms involving vortex ring generation [46, 48, 51, 69]. The exact value of the critical Formation number may vary depending on different jet velocity profiles [70] and velocity distribution at the nozzle [71].

Following Gharib *et al.* [46], in our problem we define an equivalent stroke distance as $4(\forall_0 - \forall_1)/\pi D^2$ so that our formation number is given as $\Gamma = 4(\forall_0 - \forall_1)/\pi D^3$, where $\forall_0$ and $\forall_1$ are the internal volumes at $t = 0$ and T_D, respectively. When the size (represented by L) of the

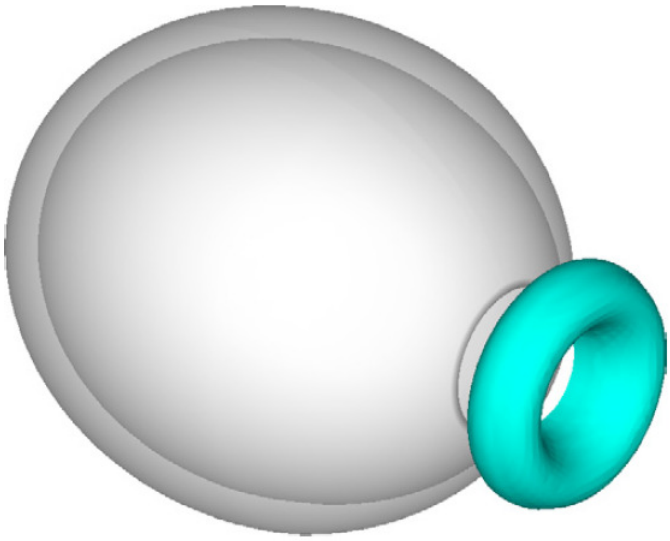

Figure 4.8: Formation of a vortex ring behind the system visualized through iso-surface of vorticity. $t = 0.65T_D$. $D/L = 0.1$.

body is given, this formation number depends on three parameters, the initial eccentricity e_0 (which determines $\forall_0$), the final eccentricity e_1 (which determines $\forall_1$), and the nozzle diameter D. We hereby fix e_1 to be 0.9, choose two values of e_0 (0 and 0.8) and study a range of D/L from 0.06 to 0.18. The corresponding values of formation number Γ in these cases are included in Table 4.2.

Figure 4.9 displays the dependencies of the normalized final speed V'_D, the traveling distance L'_D, the energy expenditure E'_D, and the efficiency $\eta_{_D}$ upon the formation number Γ with the aforementioned ranges of e_0 and D/L. The figure shows that the optimal performance in terms of the speed and traveling distance is achieved at $\Gamma \sim 12$. It implies the critical formation number under this condition (*e.g.* the jet profile displayed in Fig. 4.4) might be around 12. On the other hand, the efficiencies decrease monotonically with Γ, *i.e.* larger exits lead to higher energy efficiency, although the speed they can achieve may be small.

To explain the dependence of performance upon the formation number we examine characteristics of the wake in different cases. It is found that in the cases when Γ is above its critical value (12), the vortex ring in the wake becomes unstable and break into smaller ones before the end of

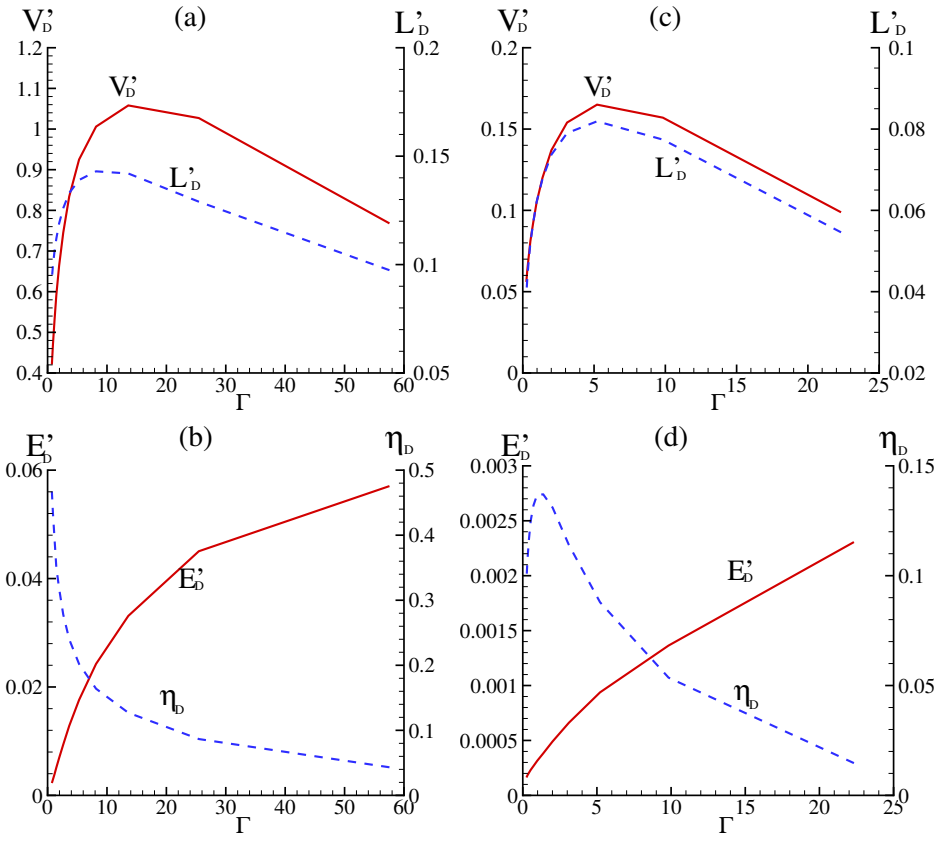

Figure 4.9: The normalized final speed of the body, traveling distance, energy expenditure, and efficiency as functions of the formation number. (a) and (b) are from the case with $e_0 = 0$. (c) and (d) are from the case with $e_0 = 0.8$. $e_1 = 0.9$.

the deflation period, as is demonstrated in Fig. 4.10a via the wake sheet. This is consistent with the wake pattern referred to as mode 2 in the DPIV visualization of flow around live squids [21]. If its value is below the critical one, the vortex ring remains stable during the whole deformation process (Fig. 4.10b), similar to another wake pattern (mode 1) observed in the aforementioned DPIV study. These results, together with the tendency shown in Fig. 4.9, suggest that the speed that can be achieved by the system is determined by the stability of the vortex ring it generates. Indeed, among all arrangements of vorticity with certain impulse a steady axi-symmetric vortex ring contains the maximum energy [72, 73]. On the other hand, it has been illustrated that with a given energy input, the optimal vortex ring (*i.e.* a vortex ring formed at the optimal formation number) possesses the maximum impulse so that it may be related to high-efficiency pulsed jet propulsion [47]. Our numerical results with a free-swimming model indicate that even if the added-mass effect is counted for, when the size of the body, the overall volume of the jet flow (determined by the body geometry and its deformability), and the deformation time (determine by the performance of the actuation system) are fixed, the thrust (and consequently the swimming speed) is maximized near the optimal formation number determined by the size of the nozzle. Hereby the added-mass related thrust is proportional to the forward speed so that it may just enhance the formation number effect. The phenomenon that a single optimally-formed vortex ring outperforms a number of smaller vorticity structures in thrust generation is reminiscent of the discovery that well-organized vorticity structures are usually associated with better propulsion performance [39]. By investigating the dynamics of a propulsion system containing multiple fins, it was illustrated that optimal thrust generation is achieved when the wake generated by the system contains a single (and strong) reversed Kármán vortex street (created through the merge of vortices from different fins), rather than a congregation of weaker vortices generated by individual fins.

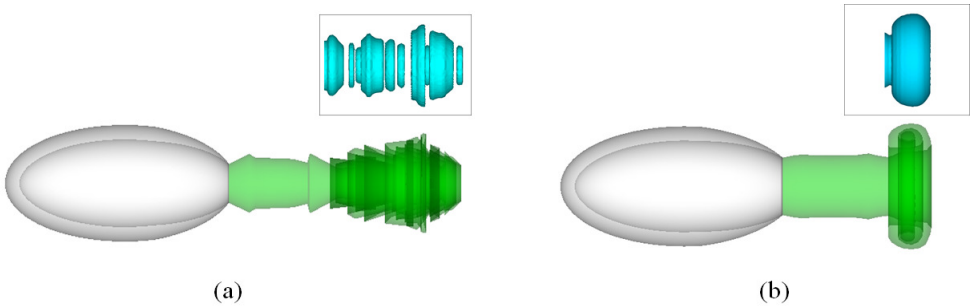

Figure 4.10: Shapes of the wake sheet at (a) $e_0 = 0$, $e_1 = 0.9$, $D/L = 0.08$, $t = T_D$, $\Gamma = 25.4$; and (b) $e_0 = 0$, $e_1 = 0.9$, $D/L = 0.12$, $t = T_D$, $\Gamma = 8.1$. The insets show the corresponding iso-surfaces of vorticity.

4.3.2 Coasting period ($T_D \leq t \leq T_D + T_C$)

In the coasting phase, the instantaneous speed of the body decreases gradually due to the viscous resistance in the fluid. The fully deflated body (with the exit and inlet being closed) is depicted as a neutrally-buoyant rigid prolate spheroid with eccentricity $e = 0.9$. Following Odar and Hamilton [74],we propose the following governing equation

$$\Lambda\rho\frac{dV_{bc}}{dt} = -\frac{1}{2}\rho S|V_{bc}|V_{bc}C_D(Re) - C_A\rho\Lambda\frac{dV_{bc}}{dt}, \tag{4.7}$$

where $2a$ denotes the chord length of the ellipsoid. $S = \pi a^2(1-e^2)$ stands for the projected area of the ellipsoid in the direction of the motion. $\Lambda = \frac{4}{3}\pi a^3(1-e^2)$ is the volume of the solid body. The Reynolds number is defined as $Re = \frac{2aV_{bc}}{\nu}$, where ν is the kinematic viscosity of fluid. The terms on the right hand side are, respectively, the quasi-steady drag force at instantaneous velocity V_{bc}, and the inertial drag due to added mass. For simplicity, the term $F_H = C_H\rho a^2\sqrt{\pi\nu}\int_0^t \frac{dV_{bc}}{dt}\frac{d\tau}{\sqrt{t-\tau}}$ that accounts for the past acceleration history of the body is neglected because its significance decreases rapidly as Re increases [75]. The added mass coefficient C_A is determined by the axis ratio of the spheroid. In this study, it is given by $C_A = \frac{\alpha}{\alpha-2}, \alpha = \frac{2(1-e^2)}{e^3}(\frac{1}{2}log\frac{1+e}{1-e} - e)$ [76]. The quasi-steady drag coefficient C_D can be approximated from the $C_D - R_e$ curve (see Fig. 4.11a) of

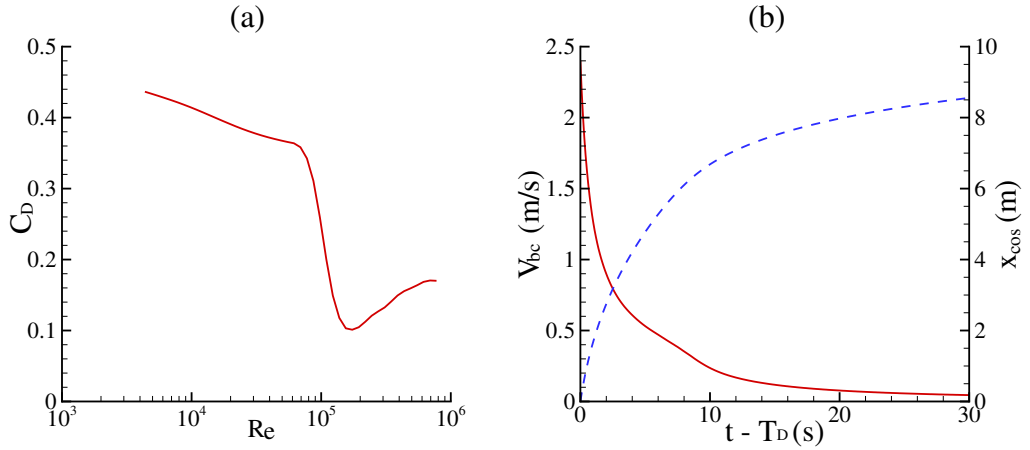

Figure 4.11: (a) $C_D - R_e$ relation for a spheroid with eccentricity $e = 0.87$ [3]. (b) Time histories of the speed V_{bc} (solid line) and the coasting distance x_{cos} defined as $-x_{bc}(t) + x_{bc}(T_D)$ (dashed line).

a spheroid with eccentricity $e = 0.87$ [3].

The motion of the body can then be calculated by numerically solving Eqn. (4.7) with the Runge-Kutta method, from which the traveling distance L_c can be determined.

As an example,we consider a body with a chord length of 0.3m and an initial speed of 2.4m/s (so that the initial Reynolds number is 7.2×10^5). In these conditions, the time histories of speed and displacement are plotted in Fig. 4.11b. The coasting distance L_c is estimated to be 8 m (27 body lengths).

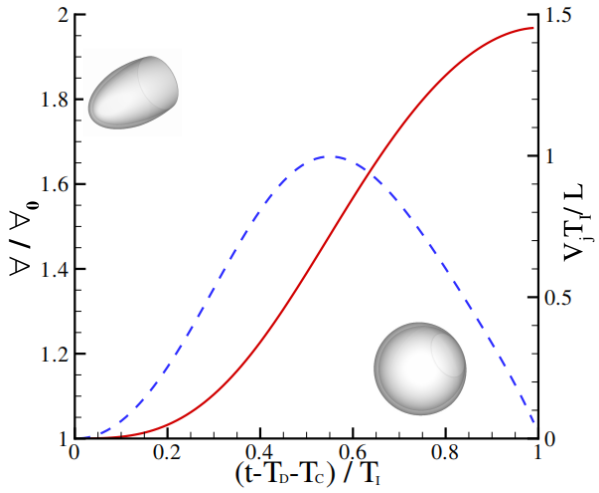

Figure 4.12: Time histories of the internal volume $\forall$ of the system normalized by it initial value $\forall_0$ (solid line) and the average speed of the jet V_j related to the inlet (dashed line) during the deformation. The insets show the shapes of the system before and after the deformation. $D_I/L = 0.2$.

4.3.3 Inflation period ($T_D + T_C \leq t \leq T_D + T_C + T_I$)

As mentioned earlier, the inflation period starts after coasting speed approaches zero. During this phase the eccentricity of the body decreases as a cubic function of time to enable a smooth start and avoid numerical instability (see §4.1). In this process the internal volume increases as shown in Fig. 4.12, which induces an jet flow into the pressure chamber. The variation of the average speed relative to the inlet of this jet is shown in the same figure. It is seen that with our specified variation of eccentricity, the speed of the incoming flow peaks at the middle of the inflation period. Its value approaches zero at both the start and the end of this phase.

Similar to the deflation case, the vorticity sheet generated at the edge of the inlet also rolls up into a torus structure (*i.e.* a vortex ring similar to the one shown in Fig. 4.8), although it occurs inside the pressure chamber (Fig. 4.13).

The inflation of the body also induces motions of its own centroid. In Fig. 4.14 we plot time histories of the body speed V_{bc} as its displacement during inflation. By comparing Fig. 4.14

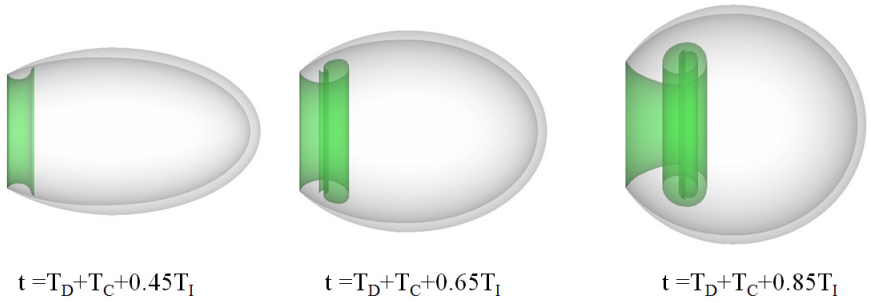

Figure 4.13: Evolution of the wake elements during the inflation deformation. $D_I/L = 0.2$.

with Fig. 4.12, a correlation between the forward speed of the body and the speed of the flow being sucked into the pressure chamber is disclosed. In this particular case with $D_I/L = 0.2$, the forward speed remains positive over the whole inflation period. Indeed, after the inflation there is still a small yet positive residue speed of 0.012 L/T_I. Correspondingly, a forward displacement of $L_I = 0.122L$ is achieved in the process.

A parametric examination about the effect of the size of the inlet (D_I) has been conducted and the results are summarized in Fig. 4.15, where we plot the normalized speed $V_I' = V_{bc}(T_D + T_C + T_I)T_I/L$ and the normalized displacement L_I' after the inflation, as well as the normalized energy expenditure E_I' over the inflation period within a range of D_I/L between 0.18 and 0.28 (due to geometric restraint 0.28 is close to the maximum value D_I/L can reach). The results show that V_I' is positive unless D_I/L is smaller than 0.19. The traveling distance L_I' remains close to 0.12 over the whole range of D_I. The energy expenditure decreases with increasing D_I.

4.4 Conclusions and discussion

To study the performance of a novel propulsion mechanism imitating the escaping motion of cephalopods, which combines body deformation and jet propulsion, we establish an idealized model including an axisymmetric object filled with fluid. In our proposed system, for sustained

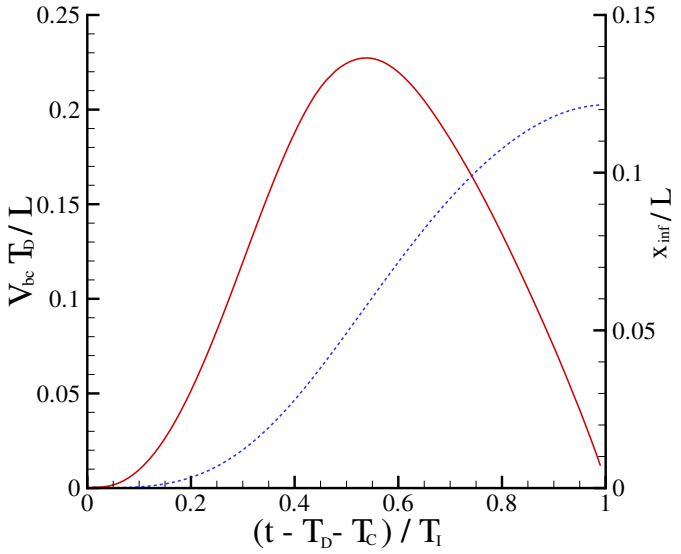

Figure 4.14: Time histories of the forward speed of the centroid of the body V_{bc} (solid line) and displacement x_{inf} defined as $-x_{bc}(t) + x_{bc}(T_D + T_C)$ (dashed line) during inflation.

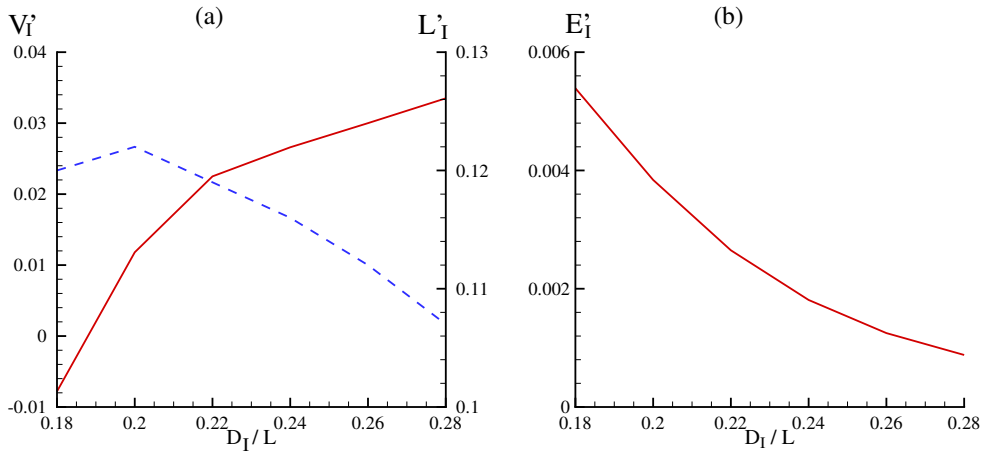

Figure 4.15: (a) Normalized velocity V_I' (solid line) and displacement L_I' (dashed line) after inflation as functions of the inlet size. (b) Normalized total energy expenditure E_I' as a function of the inlet size.

long-distance locomotion the system must undergo repeated deflation/inflation cycles to swim in a bursting-coasting style. The burst-coast cycle is decomposed into three phases, deflation, coasting, and inflation. The eventual locomotion performance depends not only on the forward speed achieved in the bursting (deflation) period, but also the effectiveness of the coasting and inflation periods. During the deflation phase, the object undergoes prescribed deformation, the internal volume shrinks and water is squeezed out through a exit, creating repulsive force that propels the object forward. This is followed by the coasting phase, in which the object moves forward as a rigid body via an initial speed gained in the deflation phase. Finally, after its kinetic energy is almost exhausted due to viscous drag, the object enters the inflation phase characterized by the expansion of its internal volume while water is sucked in.

The deflation and inflation problems are formulated within the potential-flow framework and numerically solved by using the boundary element method. The vorticity wake is modeled as a thin shear layer originated from the exit. During the deflation phase, by studying the overall thrust on the body and the effect of the shrinking added mass, it is illustrated that the additional thrust induced by added mass is most pronounced in the later stage of the deformation period, when the forward speed is already high. Meanwhile, through flow visualization it is found that a circular vortex ring is created in the wake. A parametric study has been conducted to document the performance over different combinations of volume change and nozzle size. The optimal performance in terms of speed is achieved when the *formation number*, a non-dimensional number governing the formation of the vortex ring approaches its critical value. The energy efficiency, defined as the portion of energy expenditure transferred into the kinetic energy of the body, is also studied. Within the range of parameters examined herein, this efficiency increases monotonically with the size of the exit and its maximum value approaches 0.5. However, in these high efficiency cases the forward speed is too small to have any practical value.

In the inflation phase, when fluid rashes into the pressure chamber a vortex ring is formed

there. The energy expenditure in this process is found to decay when the size of the inlet is increased. The inflation of the body is also found to induce a forward motion, although the distance gained in this phase is rather small.

This chapter, in part, is a reprint of the material as it appears in the following paper.

- Xiaobo Bi and Qiang Zhu, "Numerical Investigation of Cephalopod-Inspired Locomotion with Intermittent Bursts", *Bioinspiration & Biomimetics*, vol. 13, pp. 056005,2018.

The dissertation author is the primary investigator and author of the paper.

Chapter 5

Summary and Future Directions

5.1 Summary

The research focuses on the fluid dynamics and fluid-structure interaction mechanism of a novel jet propulsion mode inspired by squid locomotion with body deformation. This work is a pioneering investigation in the novel locomotion mode, aiming at paving the way for the development of cephalopod-inspired underwater robots that will be useful in a variety of applications. Inspired by the locomotion mechanism of squids, we proposed a novel underwater propulsion system using pulsed jet enabled by cyclic body inflation and deflation deformations. The specific design includes a flexible body with a pressure chamber and an opening.

To understand the fluid-structure interaction mechanisms involved in the propulsive performance of such a design, a two-dimensional numerical model using immersed boundary method was firstly developed. In tethered swimming mode, the 2D swimmer was found to generate higher thrust with increasing frequency of body deformation, whereas achieve an optimal propulsive efficiency at certain frequency. Depending on the frequency there are three distinct wake patterns, which are indicators of the swimming state of the swimmer. If the wake is dominated by the jet vortex pairs

(exit-shed vortex pairs), the swimmer is in acceleration state. If the wake is filled with body vortex pairs, the swimmer will be decelerated. Otherwise the two types of vortex pair coexist in the wake, indicating the force balance of thrust and drag such that the swimmer is in quasi-steady state.

But none of the three wakes could sustain longer than six inflation-deflation cycles in our simulations because symmetry-breaking instability will occur very soon. This effect compromises the propulsive performance by reducing the thrust force and inducing a lateral force as well. A straightforward solution of this problem is to stop the body deformation when the instability occurs and then restart it when the disturbances in the wake are dissipated away.

We then investigate the dynamics of the propulsive system in free swimming mode. Our results show that in long-distance swimming with multiple inflation-deflation cycles, the swimmer undergoes three different phases, acceleration, steady state and symmetry breaking, each with its own distinctive wake signature. The acceleration stage is associated with wakes dominated by jet vortices. When steady-state swimming is reached, this pattern is replaced by a transit wake, in which the strengthes of the jet vortices and the body-shed ones are comparable. Finally, when the symmetry-breaking instability dominates the wake becomes asymmetrical and the swimmer deviates from its track. The increase of the deflation-inflation frequency enhances the swimming speed at the expense of lower efficiency.

In the third chapter, we extended the 2D swimmer to an axisymmetric rendition. The body is idealized as an ellipsoidal shell with a circular orifice(exit). Three swimming modes, namely the escaping mode through body deflation, recovery mode through inflation and long-distance locomotion *via* cyclic deformation are investigated. We found that the pulsed jetting in low Reynolds number is a smooth vortex ring generation process and the vortex ring does not pinch off, which is different from cases in high Reynolds numbers.

We developed a thrust-drag decoupling strategy based on control volume analysis to predict the generated thrust. The jet-related thrust F_T in our definition can be further decomposed into three

distinct components, the jet flux force F_j, the exit over-pressure force F_p and the flow momentum force inside the body F_m. The thrust-drag decoupling method enables the calculation of jet-related thrust by using the flow field information. With the obtained thrust, we can define the propulsive efficiency of the system in the traditional manner.

Through systematic simulations, we found that the whole-cycle propulsive performance depended mostly on the incoming flow Reynolds number Re and the jet flow Reynolds number Re_j. For relatively low Re_j (*e.g.* 20), the time-averaged thrust varies considerably within the range of Re we consider. This variation mainly results from the exit pressure force F_p, which is sensitive to wake characteristics. It is shown that at low Re_j when the jet is relatively weak, the exit pressure can be easily affected by the negative pressure region induced by the vorticity shed from the outer side of the shell. However, for relatively high Re_j in which high-speed jet is discharged, the body-shed vortex ring becomes too weak to affect the jet flow or the exit pressure. In these cases the effect of Re on thrust generation is negligible. Our results suggests that the time-averaged thrust over a full cycle is linearly dependent on the jet speed when $Re_j > 100$.

The propulsive efficiency at the steady-swimming state (*i.e.* the state when the time-averaged net force on the body is zero) is then calculated at various values of Re_j. The results show that the efficiency increases as Re_j goes up. Finally, the effect of the stroke ratio has also been examined. It is demonstrated that within the current range of Re_j, and with the prescribed sinusoidal jet speed profile, the stroke ratio does not directly affect thrust generation.

By using the axisymmetric model, we investigate the pulsed jetting of the system with different nozzles added. Though a sequence simulations, we found that the thrust generation of the system (with nozzles) depends mostly on the nozzle exit size. For example, tubular nozzles generate thrust close to the one by the system without nozzle. Converging and diverging nozzles result in increased and declined thrust production, respectively. The propulsive efficiency of the system was also examined. It is shown that the usage of nozzles makes the jet propulsion less

efficient.

Finally the fluid dynamics of the squid-like jet propulsion is further studied by using a three dimensional model based on potential flow so that high Reynolds number mechanism can be involved. It was found that the *pinch off* of leading vortex ring happens at formation number (stroke ratio) $\Gamma = 12$. A parametric study has been conducted to document the performance over different formation number. The optimal performance in terms of speed is achieved at the critical formation number $\Gamma = 12$.

5.2 Future directions

The topics considered in this thesis are far from being thoroughly explored. For examples, our viscous axisymmetric numerical model is only applicable within the low Reynolds number regime. Several high Reynolds number mechanisms are not considered, including, *e.g.* the non-axisymmetric vortex shedding from the body, the *pinch-off* of the leading vortex ring, and evolution of secondary vortex rings in the wake. To address these issues, three-dimensional modeling with turbulence rendition is necessary. Moreover, the simplified propulsion system and its body kinematics exclude many other important mechanisms. For instance, aside from the jetting mode, real squids are also equipped with fins which are able to generate thrust and maneuvering force through undulating and flapping motions. The interaction mechanisms of the flapping mode and jetting mode, particularly how wakes produced in the two modes interact with each other, are unaddressed.

Appendix A

Determination of an ellipse with given contour length and exit size

As shown in Fig. A.1, we aim at finding a two-dimensional curve which is part of an ellipse with an open end (*i.e.* the exit). The contour length of the curve is L, the eccentricity is e, and the size of the nozzle is D. In the coordinate system (X, Y) the exit lies on the $X-$axis with point A at $(D/2, 0)$. Let a to be the (unknown) long axis, and b to be the distance from the center of the (complete) ellipse to the $X-$axis. We have

$$\frac{X^2}{1-e^2} + (Y-b)^2 = a^2. \tag{A.1}$$

By apply Eq. (A.1) at point A we get

$$b = \sqrt{a^2 - \frac{D^2}{4(1-e^2)}}. \tag{A.2}$$

In parametric form, the right half of the curve is expressed in terms of the angle θ ($\theta_A \leq \theta \leq \pi/2$) as

$$X = a\sqrt{1-e^2}\cos\theta, \tag{A.3}$$

$$Y = a\sin\theta + \sqrt{a^2 - \frac{D^2}{4(1-e^2)}}. \tag{A.4}$$

Then

$$dX = -a\sqrt{1-e^2}\sin\theta d\theta, \tag{A.5}$$

$$dY = a\cos\theta d\theta. \tag{A.6}$$

The unknown parameter a is determined by numerically solving the integral equation $\int_{\theta_A}^{\pi/2}\sqrt{dX^2+dY^2} = L/2$, where $\theta_A = \cos^{-1}\left[\frac{D}{2a\sqrt{1-e^2}}\right]$.

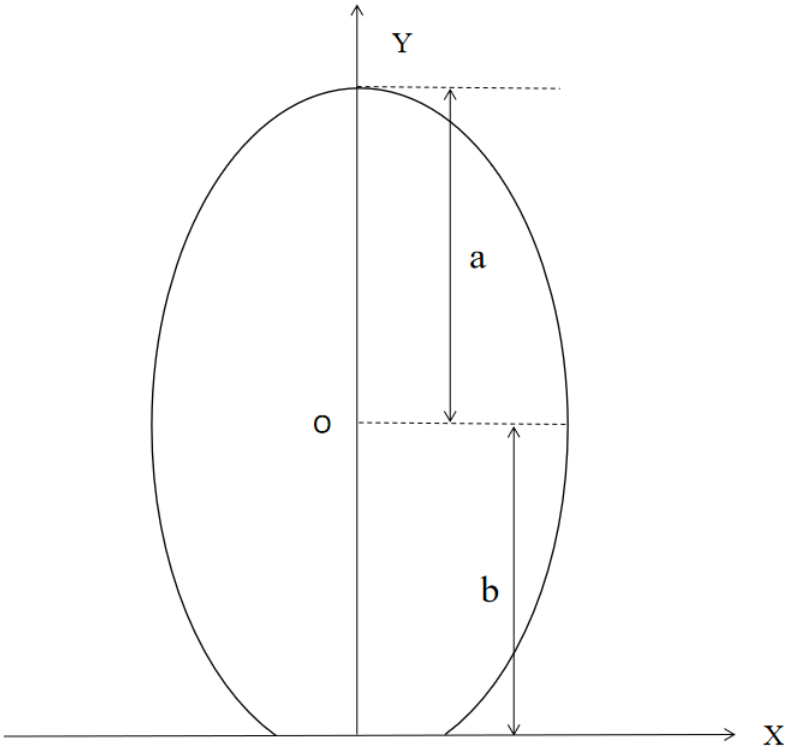

Figure A.1: An ellipse with an open end.

Appendix B

Thrust-drag decoupling and thrust decomposition

As shown in Figure B.1, a uniform flow with constant speed u_0 passes around the deformable ellipsoidal propeller. We consider a cylindrical control volume, which is bounded by the lateral surface $\delta\Omega_{side}$, the flow inlet $\delta\Omega_{in}$, and the exit plane $\delta\Omega_{out}$ (which includes the exit plane A). The control volume is separated into two parts (Ω_I and Ω_{II}) by the body, whose inner surface and outer surface are Γ_{in} and Γ_{out}, respectively. The conservation of momentum equation in the longitudinal direction is

$$\begin{aligned}\rho\frac{\partial}{\partial t}\iiint_{\Omega_I+\Omega_{II}} u_x dV - \rho\iint_{\delta\Omega_{in}} u_0^2 dS + \rho\iint_{\delta\Omega_{out}} u_x^2 dS \\ -\iint_{\delta\Omega_{in}} p_\infty dS + \iint_{\delta\Omega_{out}} (-\sigma) dS = F_n,\end{aligned} \tag{B.1}$$

where F_n represents the axial hydrodynamic force (net force) acting on the body, which includes jet-related thrust F_T ,drag F_d, and the added-mass-related force F_a [19]. p_∞ denotes the background pressure. σ is the normal fluid stress, i.e. $-p+\tau$, in which τ is the viscous normal stress. Equation

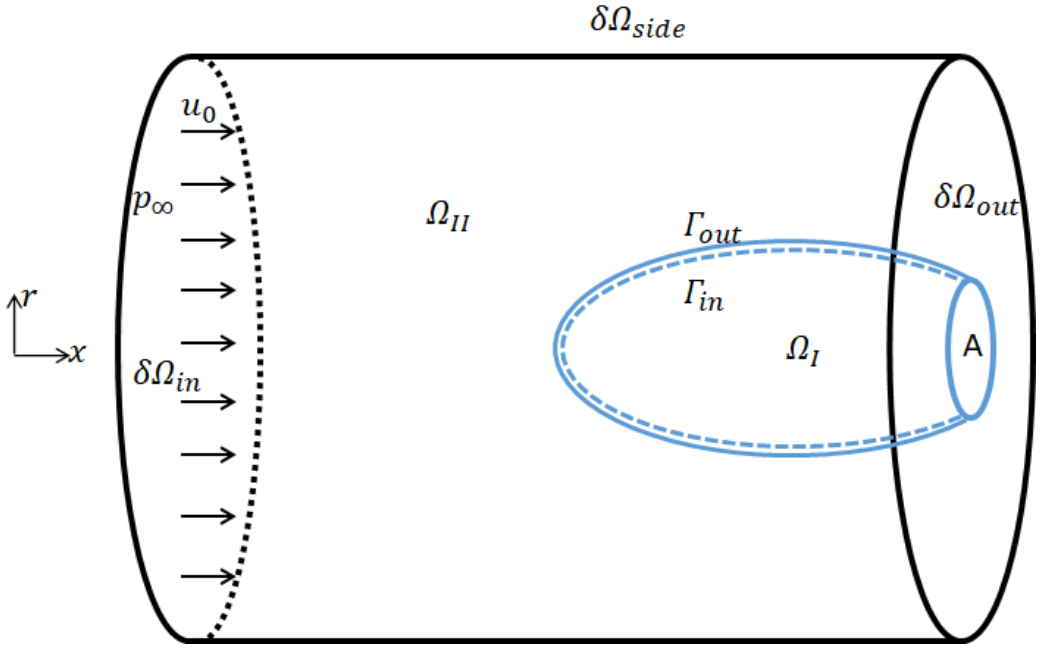

Figure B.1: Definition of the control volume and its boundaries.

(B.1) can be rewritten as

$$\begin{aligned}\rho\frac{\partial}{\partial t}\iiint_{\Omega_I} u_x dV + \rho\frac{\partial}{\partial t}\iiint_{\Omega_{II}} u_x dV - \rho\iint_{\delta\Omega_{in}} u_0^2 dS + \\ \rho\iint_{\delta\Omega_{out}-A} u_x^2 dS + \rho\iint_A u_x^2 dS + \iint_A (-\sigma - p_\infty) dS + \\ \iint_{\delta\Omega_{out}-A} (-\sigma - p_\infty) dS = F_T + F_d + F_a.\end{aligned} \tag{B.2}$$

In these expressions the positive directions of the forces (F_n, F_T, F_d and F_a) are the $-x$ direction.

On the left-hand side of Eqn. (D.1), the first, fifth, and sixth terms are associated with the internal flow and the generation of the jet flow, whereas the rest of the terms are associated with the outside flow attributed mostly to the incoming flow u_0. Based on the physical insight that the drag force F_d and added-mass-related force F_a are related to the incoming flow and the thrust F_T is related to the jet, we categorize these terms into F_T or $F_d + F_a$ according to their physical origins.

Thus we have

$$F_T = \rho\frac{\partial}{\partial t}\iiint_{\Omega_I} u_x dV + \rho\iint_A u_x^2 dS + \iint_A (-\sigma - p_\infty) dS, \tag{B.3}$$

and

$$\begin{aligned} F_d + F_a =& \rho\frac{\partial}{\partial t}\iiint_{\Omega_{II}} u_x dV - \rho\iint_{\delta\Omega_{in}} u_0^2 dS + \rho\iint_{\delta\Omega_{out}-A} u_x^2 dS \\ &+ \iint_{\delta\Omega_{out}-A} (-\sigma - p_\infty) dS. \end{aligned} \tag{B.4}$$

By doing so, we are able to extract the jet-generated thrust F_T from the net force F_n. Meanwhile, F_T is further decomposed into three components with different physical meaning. The first term on the right-hand side of Eqn. (B.3) represents the change rate of the fluid momentum inside the body (hereafter referred to as F_m), the second term is the jet flux (referred to as F_j), and the third term is the fluid stress term at the nozzle (F_σ).

Indeed, the jet-generated thrust defined in Eqn. (B.3) can be alternatively interpreted as the axial hydrodynamic force acting on the inner surface of the body. Towards this end, we perform control volume analysis on the deformable control volume Ω_I. According to the conservation of momentum in axial direction, we have

$$\begin{aligned} &\rho\frac{\partial}{\partial t}\iiint_{\Omega_I} u_x dV + \rho\iint_{\Gamma_{in}} (\mathbf{V}_r \cdot \mathbf{n}) u_x dS + \rho\iint_A u_x^2 dS + \iint_A \\ &- \sigma dS = F_{in}, \end{aligned} \tag{B.5}$$

where $\mathbf{n}$ is the unit normal vector on the control volume boundaries pointing outwards. $\mathbf{V}_r$ is the relative velocity of fluid crossing the control surface Γ_{in}, whose value is zero in this case because Γ_{in} is a non-penetrable boundary. F_{in} denotes the axial hydrodynamic force on the inner surface

with $-x$ as its positive direction. A comparison between Eqn. (B.3) and Eqn. (B.5) leads to

$$F_{in} = F_T + \iint_A p_\infty dS. \tag{B.6}$$

It is clear that F_{in} and F_T are the same except for a hydrostatic term related to the background pressure p_∞. Similar analysis on the deformable control volume Ω_{II} can also be conducted. It indicates that $F_d + F_a$ is the hydrodynamic force acting on the outside of the body. This is physically reasonable since the jet-generated force acts primarily on the inside surface, and the outer surface is directly in contact with the incoming flow.

In our formulation F_σ is a linear combination of a pressure term $F_p = \iint_A (p - p_\infty) dS$ and normal axial stress term $F_\tau = \iint_A -\tau dS$. At relatively high Reynolds number, F_τ becomes negligibly small so that F_σ is mostly equal to F_p. Our results show that even in the low Reynolds number regime we consider in this study, F_τ is small in comparison with F_p. For example, when jet -related Reynolds number $Re_j = 150$ and free-stream related Reynolds number $Re = 0$, F_τ accounts for less than 2% of F_σ, as shown in Fig. B.2. Its effect is further reduced when Re is none zero because F_p is amplified at the presence of incoming flow.

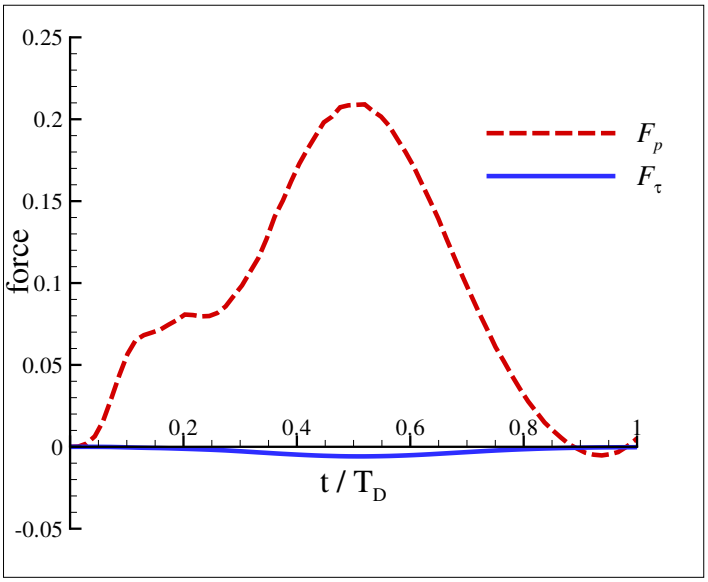

Figure B.2: Comparison between F_p and F_τ in single deflation process with cosine jet profile, $Re_j = 150$.

Appendix C

Validation of the numerical method of chapter 3

To validate the accuracy of the axisymmetric fluid solver and the feedback algorithm, they are used to simulate the canonical problem of a uniform flow around a stationary sphere. The numerical results are then compared with benchmark results from previous studies. There are different types of wake patterns behind the sphere depending on the Reynolds number Re (based on upcoming flow velocity u_0 and sphere diameter d). The flow remains unseparated when Re is smaller than 25. As Re increases the flow starts to separate from the surface of the sphere, forming an axisymmetric wake with a closed recirculating vortex ring behind. The axisymmetry and stability of the flow will then be disturbed as Re rises beyond 210. We perform simulations within the range of Reynolds number between 25 and 210, within which the axisymmetric flow pattern dominates. Simulations are performed using uniform grid $\Delta x = \Delta r = \Delta s = 0.02d$ and time step $\Delta t = 0.001d/u_0$. The feedback parameters α and β are chosen to be $-400\frac{\rho u_0^2}{d}$ and $-20\rho u_0$,respectively.

Figure C.1 shows comparisons between the present results and the data from previous

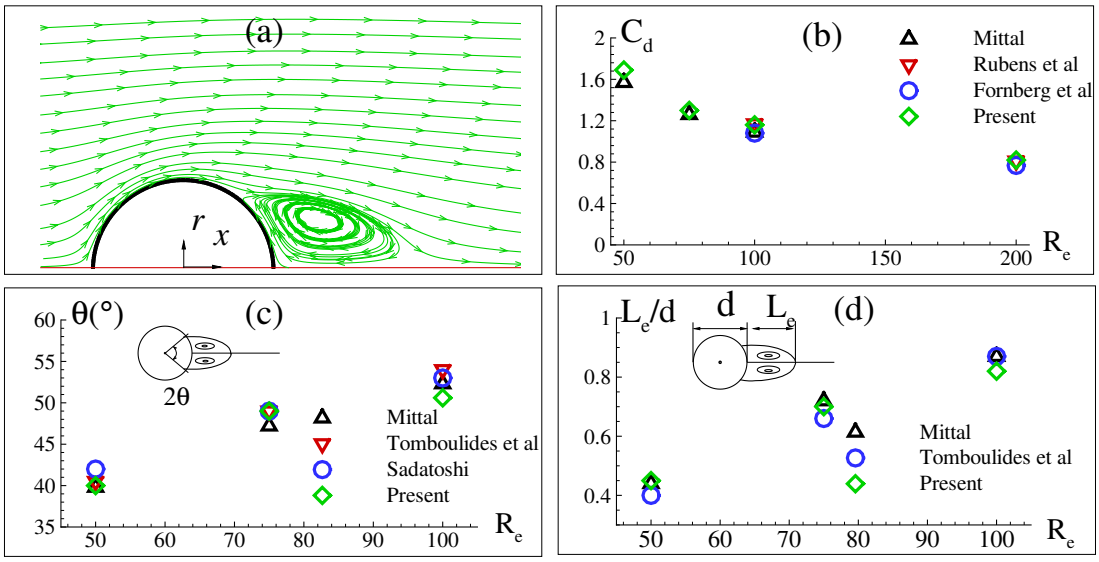

Figure C.1: Numerical simulations of flow past a sphere with diameter d and comparisons with previous results: (a) flow pattern (visualized via streamlines) at $Re = 100$, (b) the drag coefficient, (c) the separation angle, and (d) length of the standing eddy.

studies [77–81] in terms of the drag coefficient C_d, the separation angle θ, and the length of the standing eddy L_e. The drag coefficient is obtained by $C_d = F_d/(0.5\rho u_0^2 A_d)$, where F_d is the drag force on the body, and $A_d = \pi d^2/4$ is the projected area. The definitions of θ and L_e are provided in the insets in Figs. C.1c and d. It is clearly seen that the results of the current model are in good agreement with the previous data.

Appendix D

Impulse of an isolated vortex ring

Considering the wake region behind the exit plane as a control volume Ω' as illustrated in Fig. D.1, the axial momentum conservation of the control volume yields

$$\frac{\partial}{\partial t}\iiint_{\Omega'} \rho u_x dV \approx \iint_{A'} \rho u_x^2 dS + \iint_{A'} (p - p_\infty - \tau) dS = F_T^j + F_T^\sigma, \tag{D.1}$$

in which the flow flux and fluid stress term on the control volume boundaries except A' are ignored. For an isolated vortex ring, the momentum can be approximated by $(m + m_e + m_a)W$, where W is the translating speed of the vortex ring centroid in the axial direction, m is the ejected fluid mass (note that $dm/dt = \rho A' V_j'$), m_a is the added mass from the ambient fluid, m_e represents the ambient fluid entrained by the shear layer from the exit boundary layer as it rolls up into the ring [4, 82]. Assuming that the majority of the momentum inside the control volume is stored in the vortex ring bubble (this is reasonable at the initial stage when only a vortex ring is shed and there is no trailing flow following behind the ring), Eqn. (D.1) can be rewritten as

$$\frac{\partial (m + m_e + m_a)W}{\partial t} \approx F_T^j + F_T^\sigma, \tag{D.2}$$

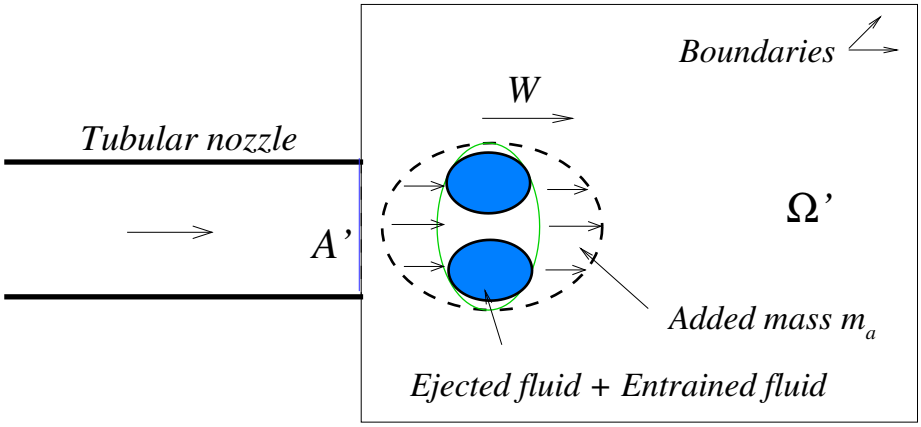

Figure D.1: Illustration of the control volume and vortex bubble. This figure is modified from Fig. 10 in reference [4].

Therefore

$$\rho A' {V_j}' W + \frac{d(m_e + m_a)}{dt} W + (m + m_e + m_a)\frac{dW}{dt} \approx F_T^j + F_T^\sigma. \tag{D.3}$$

Given the fact that the translating speed W is roughly proportional to the jet speed ${V_j}'$ [83], it is reasonable that the first term of above equation is closely related to the jet flux F_T^j and the second and third terms can be regarded as the source of F_T^σ,

$$F_T^\sigma \sim \frac{d(m_e + m_a)}{dt} W + (m + m_e + m_a)\frac{dW}{dt}. \tag{D.4}$$

Bibliography

[1] E. Anderson and M. Grosenbaugh, "Jet flow in steadily swimming adult squid," *J. Exp. Biol.*, vol. 208, pp. 1125–1146, 2005.

[2] C. Palacios-Morales and R. Zenit, "Vortex ring formation for low re numbers.," *Acta Mech*, vol. 224, pp. 383–397, 2012.

[3] M. Frank, *Fluid Mechanics (7th ed.)*. McGraw-Hill, 2009.

[4] P. S. Krueger and M. Gharib, "The significance of vortex ring formation to the impulse and thrust of a starting jet.," *PHYSICS OF FLUIDS*, vol. 15, p. 5, 2003.

[5] P. Webb, "The biology of fish swimming," in *Mechanics and Physiology of Animal Swimming* (L. Maddock, Q. Bone, and J. Rayner, eds.), pp. 45–62, Cambridge: Cambridge University Press, 1994.

[6] W. Harder, *Anatomy of Fishes*. Stuttgart: E. Schweizerbartsche Verlagsbuchhandlung, 1975.

[7] B. Flammang and G. Lauder, "Speed-dependent intrinsic caudal fin muscle recruitment during steady swimming in bluegill sunfish, *Lepomis macrochirus*," *J. Exp. Biol.*, vol. 211, pp. 587–598, 2008.

[8] B. Flammang and G. Lauder, "Caudal fin shape modulation and control during acceleration, braking and backing maneuvers in bluegill sunfish, *Lepomis macrochirus*," *J. Exp. Biol.*, vol. 212, pp. 277–286, 2009.

[9] Q. Zhu and X. Bi, "Effects of stiffness distribution and spanwise deformation on the dynamics of a ray-supported caudal fin," *Bioinspiration & Biomimetics*, vol. 12, p. 026011, 2017.

[10] K. Low and A. Willy, "Biomimetic motion planning of an undulating robotic fish fin," *Journal of Vibration and Control*, vol. 12, no. 12, pp. 1337–1359, 2006.

[11] J. Tangorra, G. Lauder, I. Hunter, R. Mittal, P. Madden, and M. Bozkurttas, "The effect of fin ray flexural rigidity on the propulsive forces generated by a biorobotic fish pectoral fin," *J. Exp. Biol.*, vol. 213, pp. 4043–4054, 2010.

[12] A. Raj and A. Thakur, "Fish-inspired robots: design, sensing, actuation, and autonomy - a review of research," *Bioinspir. Biomim.*, vol. 11, p. 031001, 2016.

[13] R. O'Dor, "How squid swim and fly," *Can. J. Zool.*, vol. 91, pp. 413–419, 2013.

[14] J. Gosline and M. DeMont, "Jet-propelled swimming in squid," *Scientific American*, vol. 252, pp. 96–103, 1985.

[15] H. Neumeister, B. Ripley, T. Preussm, and W. Gilly, "Effects of temperature on escape jetting in the squid," *J. Exp. Biol.*, vol. 203, pp. 547–557, 2000.

[16] S. Spagnolie and M. Shelley, "Shape changing bodies in fluid: hovering, ratcheting, and bursting," *Phys. Fluids*, vol. 21, p. 013103, 2009.

[17] G. Weymouth and M. Triantafyllou, "Ultra-fast escape of a deformable jet-propelled body," *J. Fluid Mech.*, vol. 721, pp. 367–375, 2013.

[18] M. Triantafyllou, G. Weymouth, and J. Miao, "Biomimetic survival hydrodynamics and flow sensing," *Annu. Rev. Fluid Mech.*, vol. 48, pp. 1–26, 2016.

[19] S. Steele, G. Weymouth, and M. Triantafyllou, "Added mass energy recovery of octopus-inspired shape change," *J. Fluid Mech.*, vol. 810, pp. 155–174, 2017.

[20] J. Gosline, J. Steeves, A. Harman, and M. DeMont, "Patterns of circular andd radial mantel muscle activity in respiration and jetting of the squid *Loligo Opalescens*," *J. Exp. Biol.*, vol. 104, pp. 97–109, 1983.

[21] I. Bartol1, P. Krueger, W. Stewart, and J. Thompson, "Hydrodynamics of pulsed jetting in juvenile and adult brief squid *Lolliguncula brevis*: evidence of multiple jet 'modes' and their implications for propulsive efficiency," *J. Exp. Biol.*, vol. 212, pp. 1889–1903, 2009.

[22] W. Stewart, I. Bartol, and K. Kreuger, "Hydrodynamic fin function of brief squid, lolliguncula brevis," *J. Exp. Biol.*, vol. 213, pp. 2009–2024, 2010.

[23] I. Bartol1, P. Krueger, R. Jastrebsky, S. Williams, and J. Thompson, "Volumetric flow imaging reveals the importance of vortex ring formation in squid swimming tail-first and arms-first," *J. Exp. Biol.*, vol. 219, pp. 392–403, 2016.

[24] C. Roh and M. Gharib, "Asymmetry in the jet opening: underwater jet vectoring mechanism by dragonfly larvae," *Bioinspir. Biomim.*, vol. 13, p. 046007, 2018.

[25] G. Weymouth, V. Subramaniam, and M. Triantafyllou, "Ultra-fast escape maneuver of an octopus-inspired robot," *Bioinspir. Biomim.*, vol. 10, p. 016016, 2015.

[26] F. Giorgio-Serchi, A. Arienti, and C. Laschi, "Underwater soft-bodied pulsed-jet thrusters: actuator modeling and performance profiling," *International Journal of Robotics Research*, vol. 35, no. 11, pp. 1308–1329, 2016.

[27] C. Christianson, Y. Cui, X. Bi, Q. Zhu, G. Pawlak, and M. Tolley, "Cephalopod-inspired robot capable of cyclic jet propulsion through shape change," p. Under review.

[28] C. Peskin, "The immersed boundary method," *Acta Numerica*, vol. 11, pp. 479–517, 2002.

[29] R. Mittal and G. Iaccarino, "Immersed boundary methods," *Annu. Rev. Fluid Mech.*, vol. 37, pp. 239—-261, 2005.

[30] B. Griffith and N. Patankar, "Immersed methods for fluid–structure interaction," *Annu. Rev. Fluid Mech.*, vol. 52, pp. 421—-448, 2020.

[31] B. Griffith, X. Luo, D. McQueen, and C. Peskin, "Comparative jet wake structure and swimming performance of salps," *International of Applied Mechanics*, vol. 1, pp. 137–177, 2009.

[32] S. Xu and Z. Wang, "An immersed interface method for simulating the interaction of a fluid with moving boundaries," *J. Comput. Phys.*, vol. 216(2), pp. 454–493, 2006.

[33] D. Golddstein, R. Handler, and L. Sirovich, "Modelling a no-slip flow boundary with an external force field," *J. Comput. Phys.*, vol. 105, pp. 354–366, 1993.

[34] W. Huang, S. Shin, and H. Sung, "Simulation of flexible filaments in a uniform flow by the immersed boundary method," *J. Comput. Phys.*, vol. 226, pp. 2206–2228, 2007.

[35] S.-J. B. Kyoungyoun Kim and H. J. Sung, "An implicit velocity decoupling procedure for the incompressible navier–stokes equations," *Int. J. Numer. Meth. Fluids*, vol. 38, pp. 125–138, 2002.

[36] K. Shoele and Q. Zhu, "Leading edge strengthening and the propulsion performance of flexible ray fins," *J. Fluid Mech.*, vol. 693, pp. 402–432, 2012.

[37] K. Shoele and Q. Zhu, "Performance of a wing with nonuniform flexibility in hovering flight," *Phys. Fluids*, vol. 25, p. 041901, 2013.

[38] K. Shoele and Q. Zhu, "Flow-induced vibrations of a deformable ring," *J. Fluid Mech.*, vol. 650, pp. 343–363, 2010.

[39] K. Shoele and Q. Zhu, "Performance of synchronized fins in biomimetic propulsion," *Bioinspir. Biomim.*, vol. 10, p. 026008, 2015.

[40] E. Anderson, H. Jiang, and M. Grosenbaugh, "Jet flow in steadily swimming squid," *Am. Zool*, vol. 41, pp. 1380–1381, 2001.

[41] H. Jiang and M. Grosenbaugh, "Numerical simulation of vortex ring formation in the presence of background flow," *Theor. Comput. Fluid Dyn.*, vol. 20, pp. 103–123, 2006.

[42] A. Leonard, "Vortex methods for flow simulation," *J. Comput. Phys.*, vol. 37, no. 3, pp. 289–335, 1980.

[43] S. Alben, L. Miller, and J. Peng, "Efficient kinematics for jet-propelled swimming," *J. Fluid Mech.*, vol. 733, pp. 100–133, 2013.

[44] H. Schlichting and K. Gersten, *Boundary-layer theory*. Springer, 2016.

[45] R. Beam and R. Warming, "An implicit factored scheme for the compressible navier–stokes equations," *AIAA J.*, vol. 16, pp. 393–402, 1978.

[46] M. Gharib, R. Rambod, and K. Shariff, "A universal time scale for vortex ring formation," *J. Fluid Mech.*, vol. 360, pp. 121–140, 1998.

[47] P. Linden and J. Turner, "The formation of 'optimal' vortex rings, and the efficiency of propulsion devices," *J. Fluid Mech.*, vol. 427, pp. 61–72, 2001.

[48] J. Dabiri, "Optimal vortex formation as a unifying principle in biological propulsion," *Annu. Rev. Fluid Mech.*, vol. 41, pp. 17–33, 2009.

[49] D. Staaf, W. Gilly, and M. Denny, "Aperture effects in squid jet propulsion," *J. Exp. Biol.*, vol. 217, pp. 1588–1600, 2014.

[50] L. Ruiz, R. Whittlesey, and J. Dabiri, "Vortex-enhanced propulsion," *J. Fluid Mech.*, vol. 668, pp. 5–32, 2011.

[51] P. Linden, "The efficiency of pulsed-jet propulsion," *J. Fluid Mech.*, vol. 668, pp. 1–4, 2011.

[52] A. Moslemi and P. Krueger, "Propulsive efficiency of a biomorphic pulsed-jet underwater vehicle," *Bioinspir. Biomim.*, vol. 5, p. 036003, 2010.

[53] A. Moslemi and P. Krueger, "The effect of reynolds number on the propulsive efficiency of a biomorphic pulsed-jet underwater vehicle," *Bioinspir. Biomim.*, vol. 6, p. 026001, 2011.

[54] E. Anderson and M. Demont, "The mechanics of locomotion in the squid *Loligo pealei*: locomotory function and unsteady hydrodynamics of the jet and intramantle pressure," *J. Exp. Biol.*, vol. 203, pp. 2851–2863, 2000.

[55] D. Barrett, *Propulsive Efficiency of a Flexibale Hull Underwater Vehicle*. PhD thesis, Massachusetts Institute of Technology, 5 1996.

[56] I. Borazjani and F. Sotiropoulos, "Numerical investigation of the hydrodynamics of carangiform swimming in the transitional and inertial flow regimes," *J. Exp. Biol.*, vol. 211, pp. 1541–58, 2008.

[57] X. Bi and Q. Zhu, "Dynamics of a squid-inspired swimmer in free swimming," *Bioinspir. Biomim.*, vol. 15, p. 016005, 2019.

[58] P. Krueger and M. Gharib, "The significance of vortex ring formation to the impulse and thrust of a starting jet," *Phys. Fluids*, vol. 15, pp. 1271–1281, 2003.

[59] C. Christianson, Y. Cui, M. Ishida, X. Bi, Q. Zhu, G. Pawlak, and M. Tolley, "Cephalopod-inspired robot capable of cyclic jet propulsion through shape change," *Bioinsp. Biomim.*, vol. 16, p. 016014.

[60] F. Renda, F. Giorgio-Serchi, F. Boyer, and C. Laschi, "Modelling cephalopod-inspired pulsed-jet locomotion for underwater soft robots," *Bioinspir. Biomim.*, vol. 10, no. 5, p. 055005, 2015.

[61] Y. Luo, Q. Xiao, Q. Zhu, and G. Pan, "Pulsed-jet propulsion of a squid-inspired swimmer at high reynolds number," *Phys. Fluids*, vol. 32, p. 111901, 2020.

[62] Y. Luo, Q. Xiao, Q. Zhu, and G. Pan, "Jet propulsion of a squid-inspired swimmer in the presence of background flow," *Phys. Fluids*, vol. 33, p. 031909, 2021.

[63] M. Krieg and K. Mohseni, "Modelling circulation, impulse and kinetic energy of starting jets with non-zero radial velocity.," *J. Fluid Mech*, vol. 719, pp. 488–526, 2013.

[64] K. Schlueter-Kuck and J. Dabiri, "Pressure evolution in the shear layer of forming vortex rings," *Phys. Rev. Fluids*, vol. 1, p. 012501, 2016.

[65] L. Gao, X. Wang, S. Yu, and M. Chyu, "Development of the impulse and thrust for laminar starting jets with finite discharged volume," *J. Fluid Mech.*, vol. 902, p. A27, 2020.

[66] Q. Zhu, M. Wolfgang, D. Yue, and M. Triantafyllou, "Three-dimensional flow structures and vorticity control in fish-like swimming," *J. Fluid Mech.*, vol. 468, pp. 1–28, 2002.

[67] Q. Zhu, "Numerical simulation of a flapping foil with chordwise or spanwise flexibility," *AIAA J.*, vol. 45, no. 10, pp. 2448–2457, 2007.

[68] Q. Zhu, Y. Liu, and D. Yue, "Dynamics of a three-dimensional oscillating foil near the free surface," *AIAA J.*, vol. 44, no. 12, pp. 2997–3009, 2006.

[69] P. Linden and J. Turner, "Optimal vortex rings and aquatic propulsion mechanisms," *Proc. R. Soc. Lond.*, vol. B271, pp. 647–653, 2004.

[70] C. T. Mohseni K., Ran H., "Numerical experiments on vortex ring formation.," *J. Fluid Mech*, vol. 430, pp. 267–282, 2001.

[71] G. M. Rosenfeld M., Rambod E., "Circulation and formation number of laminar vortex ring.," *J. Fluid Mech*, vol. 376, pp. 297–318, 1998.

[72] L. Kelvin, "Vortex statics," *Philos. Mag.*, vol. 10, pp. 97–109, 1880.

[73] T. Benjamin, "The alliance of practical and analytical insights into the nonlinear problems of fluid mechanics," in *Applications of Methods of Functional Analysis to Problems in Mechanics* (P. Germain and B. Nayroles, eds.), pp. 8–28, New York: Springer, 1976.

[74] F. Odar and W. Hamilton, "Forces on a sphere accelerating in a viscous fluid," *J. Fluid Mech.*, vol. 18, pp. 302–314, 1964.

[75] R. Clift, *Bubbles drops and particles*. Academic Press,San Diego,Calif, 1978.

[76] F. Imlay, "The complete expressions for 'addded mass' of a rigid body moving in an ideal fluid," Tech. Rep. 1528, Hydrodynamics Laboratory, Department of the Navy, 1961.

[77] S. Taneda, "Experimental investigation of the wake behind a sphere at low reynolds numbers," *Journal of the Physical Society of Japan*, vol. 11, p. 10, 1956.

[78] R. Mittal, "A fourier-chebyshev special collocation method for simulating flow past spheres and spheroids," *International Journal Of Numerical Methods in Fluids*, vol. 30, pp. 921–937, 1999.

[79] A. Tomboulides, S. Orszag, and G. Karniadakis, "Direct and large-eddy simulations of axisymmetric wakes," *AIAA J.*, vol. 93, p. 0546, 1993.

[80] R. Campregher, J. Militzer, S. S. Mansur, and A. da Silveira Neto, "Computations of the flow past a still sphere at moderate reynolds numbers using an immersed boundary method," *J. Braz. Soc. Mech. Sci. Eng.*, vol. 31, pp. 344–352, 2009.

[81] B. Fornberg, "Steady viscous flow past a sphere at high reynolds number," *J. Fluid Mech.*, vol. 190, pp. 471–489, 1988.

[82] N. Didden, "On the formation of vortex rings: Rolling-up and production of circulation," *Z. Angew. Math. Phys.*, vol. 30, p. 101, 1979.

[83] K. Mohseni and M. Gharib, "A model for universal time scale of vortex ring formation.," *Phys. Fluids*, vol. 10, pp. 2436–2438, 1998.